

ABSTRACT

Title of Document: THERMOMECHANICAL BEHAVIOR OF
POLYMER COMPOSITE HEAT
EXCHANGERS

Franklin Robinson, Master of Science, 2011

Directed By: Professor Avram Bar-Cohen, Mechanical
Engineering

Professor Hugh Bruck, Mechanical Engineering

Industrial cooling with seawater, particularly at elevated temperature and salinity, shortens the useful lives of conventional metallic heat exchangers. Cost effective, corrosion-resistant heat exchangers are required to fully utilize available saline water resources. Polymer composites, which use carbon fibers for thermal and mechanical reinforcement, are a promising material for such heat exchangers.

The present thesis provides a characterization and thermomechanical analysis of heat exchangers fabricated using thermally conductive polymers. The change in mechanical properties resulting from exposure to saltwater at elevated temperature is characterized for raw and reinforced polymers. Then, thermal performance of such heat exchangers is compared to that of heat exchangers fabricated from conventional corrosion-resistant materials. Finally, the mechanical and combined thermomechanical response of such heat exchangers to conditions typical of LNG operations is studied and compared to that of heat exchangers fabricated from conventional corrosion-resistant materials.

THERMOMECHANICAL BEHAVIOR OF
POLYMER COMPOSITE HEAT EXCHANGERS

By

Franklin Lee Robinson III

Thesis submitted to the Faculty of the Graduate School of the
University of Maryland, College Park, in partial fulfillment
of the requirements for the degree of
Master of Science
2011

Advisory Committee:
Professor Avram Bar-Cohen, Co-chair
Professor Hugh Bruck, Co-chair
Professor Abhijit Dasgupta
Professor Satyandra Gupta

© Copyright by
Franklin Lee Robinson III
2011

Acknowledgements

I am grateful for the intellectual and motivational support of my advisors, Prof. Avram Bar-Cohen and Prof. Hugh Bruck, who provided tremendous insight during my tenure as their student. This thesis would not have been possible without their persistence and intellect, particularly in the fields of heat transfer, solid mechanics and materials characterization.

I am grateful for the support of Prof. Satyandra Gupta and Prof. Abhijit Dasgupta as committee members. Prof. Gupta's expertise in polymers and manufacturing and Prof. Dasgupta's expertise in composites and thermomechanical modeling have proven most useful during my time at the University of Maryland.

I must acknowledge the contributions of my colleague, Juan Cevallos, who has worked with me in the field of polymer composite heat exchangers throughout my time as a graduate student. His experience, knowledge and willingness to help were tremendously valuable to me as I completed my studies and thesis. Furthermore, Juan's experimental studies and analytical heat transfer calculations were most useful in my thesis.

I must also acknowledge the work of Patrick Luckow on the least-material design of polymer composite heat exchangers. The experimental apparatus allowed for the experimental heat transfer results shown in my thesis.

I appreciate the intellectual contributions of my lab mates Emil Rahim and Mike Manno. Beyond their intellectual insight, Emil and Mike were responsible for many welcomed distractions during the stressful process of completing this thesis.

I must recognize Jeffrey Didion, whose support and flexibility were most valuable as I completed my degree while working as a co-operative student at the National Aeronautics and Space Administration's Goddard Space Flight Center.

This research was supported as part of the Energy Education and Research Collaboration between the University of Maryland and the Petroleum Institute in Abu Dhabi, United Arab Emirates. The Abu Dhabi National Oil Company and its international partners deserve appreciation for their generous financial support.

Table of Contents

Acknowledgements.....	ii
Table of Contents.....	iv
List of Tables.....	vi
List of Figures.....	vii
Nomenclature.....	x
Chapter 1: Introduction.....	1
History of Polymer Heat Exchangers.....	1
Seawater-Cooled Heat Exchangers.....	2
Energy Use.....	8
Water Use.....	14
Electricity Generation and Water Use Nexus.....	16
Potential Applications for Polymer Composite Heat Exchangers.....	22
Overview of Thesis.....	24
Chapter 2: Polymers and their Composites.....	26
Introduction.....	26
Types of Polymers.....	26
Properties of Polymers.....	28
Thermoplastic Polymers.....	28
Polymer Reinforcements.....	31
Characteristics of Polymer Fiber Composites.....	35
Chapter 3: Calculation of Composite Properties.....	39
Polymer-Fiber Composite.....	39
Effective Fiber Modulus.....	41
Anisotropic Mechanical Properties.....	42
Anisotropic Thermal Properties.....	46
Chapter 4: Hygrothermal Aging Studies.....	49
Motivation.....	49
Operating Conditions.....	50
Experimental Setup.....	50
Results and Discussion.....	54
Summary of Findings.....	72
Chapter 5: Mechanical Modeling.....	74
Motivation.....	74
Operating Conditions.....	74
Finite Element Model.....	75
Prototype Heat Exchanger.....	77
Mesh Independence Study.....	79
Model Verification.....	86
Results and Discussion.....	88
Summary of Findings.....	92
Chapter 6: Thermal Modeling.....	94
Motivation.....	94

Experimental Study.....	94
Numerical Study	103
Summary of Findings.....	115
Chapter 7: Thermomechanical Modeling	116
Motivation.....	116
Thermal Stress Development.....	116
Operating Conditions	120
Results.....	120
Variation of Geometry	130
Summary of Findings.....	133
Chapter 8: Summary of Findings and Contributions and Path to Commercialization	
.....	135
Summary of Findings and Contributions.....	135
Path to Commercialization.....	138
Appendix 1: ANSYS Code	141
References.....	148

List of Tables

Table 1: Properties of common heat exchanger materials [10-17]	4
Table 2: Fouling of heat transfer surfaces by industry group [20,21]	5
Table 3: Surface energy of corrosion-resistant heat exchanger materials	8
Table 4: Physical and mechanical properties of thermoplastic polymers [47,48]	29
Table 5: Properties of common fibers [52]	34
Table 6: Carbon fiber properties [66]	39
Table 7: Composite structural properties	46
Table 8: Injection molding parameters for raw and reinforced PA12 [64,65].....	51
Table 9: Weight % difference between unaged and redried composite PA12	58
Table 10: Weight % difference between unaged and redried raw PA12	58
Table 11: Mechanical properties input into finite element model	77
Table 12: Mesh parameters and their values.....	80
Table 13: Maximum stresses in isotropic HX as a function of airside pressure.....	87
Table 14: Maximum stresses from isotropic and transversely isotropic finite element heat exchanger models	92
Table 15: Thermal material properties input into finite element model	104
Table 16: Location of maximum stresses in PCHX exposed to combined loading..	124
Table 17: Location of maximum stresses in Ti HX exposed to combined loading..	129

List of Figures

Figure 1: Total global primary energy production by source, 1970-2007 [35]	9
Figure 2: Relative global primary energy production by source, 1970-2007 [35]	10
Figure 3: Electricity flow in the United States, 2009 (units: quadrillion Btu) [35]	12
Figure 4: Electricity generation in the United States by source [36]	13
Figure 5: CO ₂ emissions from electricity generation [36]	14
Figure 6: SO ₂ and NO _x emissions from electricity generation [36]	14
Figure 7: Water withdrawals in the United States by end use [40]	15
Figure 8: Cooling systems for thermoelectric power plants [43]	17
Figure 9: Current cooling systems for thermoelectric power plants [44]	18
Figure 10: Power output and cost of power plants based on cooling system [45]	20
Figure 11: Water withdrawals across fuel cycles [38]	21
Figure 12: Common polymers by type	27
Figure 13: Composite materials with different forms of constituents [51]	32
Figure 14: Typical tensile stress-strain curve for unreinforced PP [53]	35
Figure 15: Typical tensile stress-strain curves for SGF/PP and SCF/PP composites (C: carbon, G: glass, 1: 25 vol. %, 2: 16 vol. %, 3: 8 vol. %) [53]	35
Figure 16: Residual stresses in carbon-epoxy due to 100°C temperature drop (units: MPa) [58]	37
Figure 17: SEM micrograph of tensile fracture surface of an SCF/PP composite with carbon fiber (8 vol. %) [62]	38
Figure 18: Thermal conductivity based on Nielson model	48
Figure 19: Water baths for hygrothermal aging studies	52
Figure 20: Dimensions of type V tensile specimens (units: mm) [84]	54
Figure 21: Dogbone specimen prepared for tensile testing	54
Figure 22: Equilibrium moisture content of raw and reinforced PA12	55
Figure 23: Yield strength of hygrothermally-aged raw PA12	60
Figure 24: Elongation at yield of hygrothermally-aged raw PA12	60
Figure 25: Elastic modulus of hygrothermally-aged raw PA12	61
Figure 26: Failure strength of hygrothermally-aged raw PA12	62
Figure 27: Yield strength of hygrothermally-aged composite PA12	63
Figure 28: Elongation at yield of hygrothermally-aged composite PA12	63
Figure 29: Elastic modulus of hygrothermally-aged composite PA12	64
Figure 30: Failure strength of hygrothermally-aged composite PA12	65
Figure 31: Elongation at failure of hygrothermally-aged composite PA12	65
Figure 32: Yield strength of redried raw PA12	66
Figure 33: Elongation at yield of redried raw PA12	66
Figure 34: Elastic modulus of redried raw PA12	66
Figure 35: Failure strength of redried raw PA12	67
Figure 36: Yield strength of redried composite PA12	68
Figure 37: Elongation at yield of redried composite PA12	68
Figure 38: Elastic modulus of redried composite PA12	68
Figure 39: Failure strength of redried composite PA12	69
Figure 40: Elongation at failure of redried composite PA12	69

Figure 41: Stress-strain behavior of raw and reinforced PA12.....	70
Figure 42: Das Island seawater intake and outlet [90].....	75
Figure 43: Fluid inlet pressures for heat exchangers in Das Island third LNG train [91].....	75
Figure 44: SOLID226 brick element [93].....	76
Figure 45: Isometric view of prototype heat exchanger [34].....	78
Figure 46: Heat exchanger dimensions (units: mm) [34]	78
Figure 47: Variation of number of divisions parameter (left: 3, right: 5).....	79
Figure 48: Variation of spacing ratio parameter (left: 2, right: 5)	80
Figure 49: Variation of x-y element size parameter (left: 0.50 mm, right: 0.25 mm) 80	80
Figure 50: Variation of z element size parameter (left: 1.0 mm, right: 0.5 mm).....	80
Figure 51: Mesh independence study for x-direction stress magnitude	82
Figure 52: Mesh independence study for y-direction stress magnitude	82
Figure 53: Mesh independence study for z-direction stress magnitude.....	82
Figure 54: Mesh independence study for y-z-direction stress magnitude	83
Figure 55: Error in stress magnitude as a function of computation time.....	83
Figure 56: High accuracy, low runtime mesh configuration	84
Figure 57: X-direction stress contours.....	85
Figure 58: Original (left) and refined (right) volume assignments.....	85
Figure 59: Refined brick mesh on heat exchanger.....	86
Figure 60: Y-direction stress magnitudes in an airside channel of an isotropic heat exchanger exposed to an airside pressure of 1.0 MPa (Units: Pa).....	88
Figure 61: Maximum stress development in heat exchangers fabricated from various materials subjected to mechanical loading	89
Figure 62: Maximum x-, y-, and xy-stress locations in isotropic and anisotropic heat exchangers.....	90
Figure 63: Heat exchanger test facility [34]	95
Figure 64: Experimental and analytical heat transfer rates.....	103
Figure 65: Fluid inlet and outlet on heat exchanger	105
Figure 66: Calculated local heat transfer coefficients for air and water in a counter flow configuration.....	106
Figure 67: Numerical and experimental results	107
Figure 68: Airside heat transfer coefficients over range of conditions.....	109
Figure 69: Heat transfer rate of heat exchangers made from various materials	110
Figure 70: Temperature distributions of PCHX (left) and Ti HX (right) (units: °C) 112	112
Figure 71: Map of heat transfer rate using simplified network model	113
Figure 72: Fin efficiency as a function of conductivity and heat transfer coefficient (fin height: 5.0 mm, fin thickness: 2.5 mm)	114
Figure 73: Elastic modulus and CTE of polymers and metals [100].....	117
Figure 74: Modulus-CTE product of polymers and metals [100].....	117
Figure 75: Yield strength and inverse normalized modulus-CTE product of polymers and metals [16] [100].....	118
Figure 76: Maximum stress development from thermomechanical loading of PCHX (ST: structural only loading. TM: thermomechanical loading)	121
Figure 77: Y-direction stresses under combined loading for an airside pressure of 0.5 MPa and air inlet temperature of 150°C (units: Pa).....	122

Figure 78: Naming convention for channels in HX.....	123
Figure 79: Naming convention for channel fillets	124
Figure 80: Maximum stress development from thermomechanical loading of titanium HX (ST: structural only loading, TM: thermomechanical loading)	127
Figure 81: Normalized stresses in polymer composite heat exchanger.....	128
Figure 82: Normalized stresses in titanium heat exchanger	128
Figure 83: Maximum directional stress magnitude as a function of fin and plate thickness.....	132

Nomenclature

A	Area (m^2)
A_N	Nielson model parameter based on fiber shape and orientation (-)
AR	Aspect ratio (-)
B	Nielson model parameter (-)
C_{min}	Smallest heat capacity of two fluids ($\text{J/kg}\cdot\text{K}$)
C_r	Ratio of fluids' heat capacities (-)
D_h	Hydraulic diameter (m)
E	Elastic modulus (GPa)
G	Shear modulus (GPa)
Gz	Graetz number (-)
$LMTD$	Log mean temperature difference ($^{\circ}\text{C}$)
L^+	Dimensionless position (-)
L^*	Dimensionless position (-)
M	Moisture content (-)
M_m	Equilibrium moisture content (-)
Nu	Nusselt number (-)
NTU	Number of transfer units (-)
Pr	Prandtl number (Pr)
R	Mean separation of fibers (m)
Re	Reynolds number (-)
S	Stress (MPa)
SE	Sum of the error (-)
T	Temperature ($^{\circ}\text{C}$)
UA	Overall thermal conductance (W/K)
V	Volume fraction (-)
\dot{V}	Volumetric flow rate (m^3/s)
W	Weight (g)
c_p	Specific heat capacity ($\text{J/kg}\cdot\text{K}$)
d	Average fiber diameter (m)
f	Friction factor (-)
\bar{f}	Apparent friction factor (-)
h	Heat transfer coefficient ($\text{W/m}^2\cdot\text{K}$)
k	Thermal conductivity ($\text{W/m}\cdot\text{K}$)
k_E	Einstein coefficient (-)
l	Average fiber length (m)
\dot{m}	Mass flow rate (kg/s)
\dot{q}	Heat transfer rate (W)
r	Average fiber radius (m)
t	Thickness (m)
$x_{fd,h}$	Hydrodynamic entry length (m)
$x_{fd,t}$	Thermal entry length (m)

Greek Letters

Δ	Difference (-)
Φ	Foye coefficient (-)
α	Coefficient of thermal expansion ($\mu\text{m}/\text{m}/^\circ\text{C}$)
β	Shear-lag parameter (-)
ε	Effectiveness (-)
η	Shear modulus parameter (-)
η_{fin}	Fin efficiency (-)
η_o	Surface efficiency (-)
ν	Poisson's ratio (-)
ξ	Shear modulus parameter (-)
σ	Stress (MPa)
φ_2	Fiber volume fraction (-)
φ_m	Maximum packing fraction (-)

Subscripts

H	Constant heat flux wall condition
L	Longitudinal
$Temp$	Constant wall temperature wall condition
T	Transverse
T'	Orthogonal to longitudinal and transverse planes
b	Base
c	Composite
d	Dry
f	Fiber
fd	Fully developed
h	Hydrodynamic
i	Inlet
m	Matrix
max	Maximum
o	Outlet
rd	Redried
t	Time
th	Thermal
w	Wall
x	X-direction
xy	XY-direction
y	Y-direction
1	Fluid 1
2	Fluid 2

Chapter 1: Introduction

History of Polymer Heat Exchangers

Polymer heat exchangers (PHXs) were first introduced by DuPont in 1965 [1]. These heat exchangers consisted of bundles of many flexible, thin-walled, small-diameter polytetrafluoroethylene (PTFE) tubes that were joined at their ends to form a honeycomb structure that could be used in shell-and-tube and immersion configurations. They were adopted for many industrial applications, such as pickling in steel manufacturing, heating of agitated reactor vessels and heating and cooling of distilled water. The wide availability and versatility of polymers has since driven the interest of the research community toward the use of these materials in heat exchange applications [2,3].

When corrosive fluids are present in the heat exchange process, polymers are an increasingly popular material choice as an alternative to exotic metals [4], especially when strong acidic solutions are present [5]. Due to their low surface energy and smooth surface, fouling deposits have a lower propensity to adhere to polymers, leading to a reduction in the fouling resistance, which can play an important role in the performance of corrosion-resistant heat exchangers. In seawater heat exchangers, fouling is generally a costly problem due to the many modes of fouling that occur when using seawater as a heat transfer fluid: corrosion, biological, crystallization and particulate [6]. Therefore, the material properties of polymers make them strong candidates to replace costly exotic metals such as copper-nickel alloys and titanium.

Several reports have been published with the aim of reviewing the latest advances in PHX technology. Zaheed and Jachuck [7] reviewed the use of polymers in compact heat exchangers, paying special attention to designs made of high temperature polyetheretherketone (PEEK) with 100- μm -films fabricated with corrugations to enhance boundary layer mixing. The most recently published review, by T'Joen et al [8], aimed to assess the merits of PHXs for heating, ventilation, air-conditioning and refrigeration applications. Heat exchanger applications are reviewed in detail and special attention is paid to polymer matrix composites, which offer vast improvements in thermal conductivity. Most notably, fiber-filled composites are most promising because of their availability as injection molding resins [9].

Composites with thermal conductivities up to two orders of magnitude higher than those of unreinforced polymers were made possible by the development of pitch-based and vapor-grown carbon fibers and carbon nanotubes that offer very high thermal conductivities (i.e., $\sim 1000 \text{ W/m}\cdot\text{K}$ for fibers, $>2000 \text{ W/m}\cdot\text{K}$ for nanotubes). It is noteworthy that with improved fiber conductivity, polymer composites approach the thermal properties of common corrosion resistant metals (e.g., titanium and stainless steel) and thus, can be considered as replacements for metals in applications where seawater is used as a direct coolant for industrial processes.

Seawater-Cooled Heat Exchangers

Applications

Heat exchangers are fundamental components of many processes, including space heating, air-conditioning, refrigeration, chemical and petrochemical processing, cooling of thermoelectric power plants, wastewater treatment, and natural gas

processing. Many heat exchange applications involve the heating and cooling of corrosive fluids. The present study focuses on seawater-cooled heat exchangers for cooling of thermoelectric power plants and for the liquefaction of natural gas.

Materials

Seawater, particularly at high salinity and elevated temperature, is very corrosive, and thus seawater-cooled heat exchangers must be built from corrosion-resistant materials. The most common corrosion-resistant materials for implementation in seawater-cooled heat exchangers are titanium, cupronickel alloys or stainless steels. Table 1 provides an overview of the mechanical and thermal properties of common heat exchanger materials. Please note that density, thermal conductivity, yield strength and coefficient of thermal expansion (CTE) information is from Shah [10], elastic modulus information is taken from MatWeb [11-15], the yield strength of PTFE is from Jones [16] and embodied energy information is from Ashby, Shercliff and Cebon [17].

The properties reveal that the thermal conductivities of corrosion-resistant materials are lower than those of their non-corrosion-resistant counterparts by as much as an order of magnitude or more. However, the elastic modulus and yield strengths of the corrosion-resistant materials are high and their CTEs are low, similar to those respective properties of the non-corrosion-resistant materials shown. The embodied energy of titanium is much higher than those of other materials, including corrosion-resistant materials such as stainless steel. Please note that Ashby, Shercliff and Cebon [17] provide an embodied energy of 400-500 GJ/m³ for carbon fiber reinforced polymers, which is lower than the embodied energy of the metals shown.

The relatively lower embodied energy of polymer composites can be largely attributed to the low energy content of conventional polymers (i.e., 60-200 GJ/m³).

Table 1: Properties of common heat exchanger materials [10-17]

Material	Name	Density (kg/m ³)	Thermal Cond. (W/m·K)	Elastic Modulus (GPa)	Yield Strength (MPa)	CTE (μm/m/°C)	Embodied Energy (GJ/m ³)
Aluminum Alloy	AA3003	2710	169	68.9	69	7.2	500-600
Copper Alloy	Cu 99.9	8890	391	110	69	5.2	-
Nickel Alloy	Hastelloy A	8800	17	-	303	3.4	1000-1200
Nickel Alloy	Inconel X	8250	12	-	690-932	3.8	1000-1200
PTFE	-	2140-2200	0.25	3.6	13-16	126-216	300-350
Stainless Steel Alloy	SS 304	7920	16	193-200	207	4.4	600-700
Stainless Steel Alloy	SS 316	8080	16	79.3	276	4.9	600-700
Stainless Steel Alloy	SS 446	7470	21	-	345	3.2	600-700
Titanium Alloy	Grade 2	4510	17	116	517	2.6	4000-4500

Corrosion and Fouling

Types

Corrosion and fouling are two factors that influence heat exchanger design and performance. There are several different types of corrosion [18], which include overall corrosion, which is a uniform attack over the entire exposed surface; pitting corrosion, which is characterized by highly localized corrosion rates with little or no corrosion in the areas surrounding the pits; galvanic corrosion, which occurs when two dissimilar metals are electrically connected in the presence of an electrolyte, causing the more electrochemically active metal to corrode at an increasing rate by giving off electrons; microbiologically-induced corrosion, which occurs beneath

colonies of microorganisms that form colonies on the heat exchange surface; stress-corrosion cracking, which occurs when a stressed metal is exposed to certain types of environment; and hydrogen embrittlement, which affects noble alloys (e.g., titanium).

Fouling is defined generally as the undesired deposition of material on surfaces [19], including: scaling and mineral fouling, which is the deposition of inorganic material precipitating on a surface; deposition of organic substances (e.g., oils and proteins); particle fouling, which is the deposition of silica, clay, humic substances and other particles; and biofouling, which is the adhesion of microorganisms to surfaces and biofilm development. Table 2 provides an overview of the types of fouling that occur on heat transfer surfaces in various industry groups where polymer composite heat exchangers could be implemented.

Table 2: Fouling of heat transfer surfaces by industry group [20,21]

Industry group	Type of fouling that occurs in heat exchange equipment	Usual extent of problem
Chemical and allied	Crystallization (process side, cooling water)	Medium
	Particulate (process side, cooling water)	Minor/medium
	Biofouling (cooling water)	Medium
	Chemical reaction (process side)	Minor/major
	Corrosion	Medium
Petroleum refining and related industries	Chemical reaction (process side)	Major
	Crystallization (cooling water)	Medium
	Particulate (cooling water, gas side)	Minor/medium
	Biofouling (cooling water)	Medium
	Corrosion (process side)	Medium
Electric power production	Biofouling (cooling water)	Major
	Crystallization (cooling water, boiler water)	Medium
	Particulate (furnace side)	Major
	Freezing (furnace-side slag formation)	Major
	Corrosion (condensers)	Major

Seawater heat exchangers generally experience high rates of corrosion and fouling because of the corrosiveness of the seawater and the inorganic and organic content of the water. Seawater heat exchangers are particularly susceptible to microbiologically induced corrosion due to the variety of biofouling processes derived from the natural microflora contained in the water [22,23]. As such, seawater heat exchangers must be carefully designed and maintained to prevent the undesirable effects of fouling and corrosion.

Effects

Corrosion, fouling and scaling are widely recognized as factors that diminish the performance of heat exchangers, particularly those operating with seawater as one of the working fluids. In general, the presence of fouling on heat exchanger surfaces decreases their heat transfer performance. The thermal conductivity of biofilms, for example, is similar to that of water, but its presence allows only diffusive heat transport and inhibits convective heat transport [24]. Shah and Sekulic [25] explained that fouling is costly because of increased capital costs resulting from the need to oversurface the heat exchanger and for cleaning; increased maintenance costs resulting from cleaning, chemical additives and troubleshooting; loss of production due to shut down or reduced capacity; and increased energy losses due to reduced heat transfer, increased pressure drop and dumping of dirty streams present.

Prevention

Many countermeasures have been implemented to reduce corrosion and fouling in seawater heat exchangers. One of the most common methods to prevent biofouling is by using biocides that kill biological material in the water. Chlorine was implemented as a biocide for many years in concentrations of about 1 mg/L, but the

products of chlorine reactions with organic matter are toxic and may be carcinogenic [26]. In general, biocides are toxic and their use pollutes the water being used in the heat exchange process, which can contaminate local water sources when released.

One notable difference between corrosion-resistant heat exchangers and other heat exchangers is in material selection, with seawater heat exchangers requiring the use of costly and energy intensive corrosion resistant metals and alloys. Research has indicated that polymer heat exchanger surfaces are less prone to fouling than metallic heat exchanger surfaces [26]. It is for this reason that polymers are sometimes employed as surface coatings in metallic heat exchangers; however, the addition of a coating to the metallic surface increases the overall thermal resistance.

Mott [27] studied the effect of surface condition on biofouling and found that smooth surfaces (e.g., glass and electropolished 316 stainless steel) had 35% less biofilm deposition than did the surfaces of a similar unpolished 316 stainless tube. Mott also found that fluorinated ethylene polypropylene gave a similar reduction in biofilm accumulation to the reduction achieved with smooth surfaces.

Research has indicated that materials with low surface energy may be less prone to fouling. The surface energy of several heat exchanger materials is provided in Table 3. Polytetrafluoroethylene (PTFE) has the lowest surface energy, which contributes to its excellent non-stick and antifouling properties. Untreated carbon fibers exhibit a range of surface energy that is comparable to the surface energy of corrosion-resistant alloys such as stainless steel or titanium. However, the design goal in carbon fiber polymer composites for heat exchangers is to minimize the weight fraction of carbon fibers and thus, the low surface energy of the polymer matrix

material is expected to dominate the composite surface energy. Therefore, carbon fiber polymer matrix composites are likely to have surface energies in the range of 20-35 mJ/m². It is noteworthy that this expected range is near the optimum range of 20-30 mJ/m² recommended by Baier and Meyer [28], who suggests that efforts to reduce the surface energy below this range are counterproductive.

Table 3: Surface energy of corrosion-resistant heat exchanger materials

Material	Surface Energy (mJ/m ²)
PTFE [29]	18.6
Polyamide 12 [30]	31.0
Carbon fibers [31]	38.1-44.1
Stainless steel 304 [32]	40.7
Titanium [32]	42.0
Stainless steel 316L [32]	43.9

Zhao et. al [33] investigated corrosion and fouling rates of composite Nickel-Copper-Phosphorous-Polytetrafluoroethylene (Ni-Cu-P-PTFE) coatings to assess the effect of surface energy. They found that the surface free energy of N-Cu-P-PTFE coated surfaces has a significant influence on surface adhesion of bacteria and calcium sulfate, and concluded that graded electroless Ni-Cu-P-PTFE coatings with corrosion resistant properties can reduce biofouling and mineral fouling. Furthermore, the fouling that does occur on these surfaces is easier to clean because of weaker binding at the interface between the composite and deposited material [33].

Energy Use

Global Primary Energy Production

Between 1970 and 2007, global primary energy production increased 121% from 227.3 exajoules (EJ) to 501.3 EJ, as shown in Figure 1. The increase in global energy production was roughly linear over this span ($R^2=0.9736$) and increased annually by 7.41 EJ on average. Fossil fuels accounted for 86.2% of global primary

energy production in 2007, which represents only a modest decrease of the 93.2% contribution fossil fuels made to global energy production in 1970 [35].

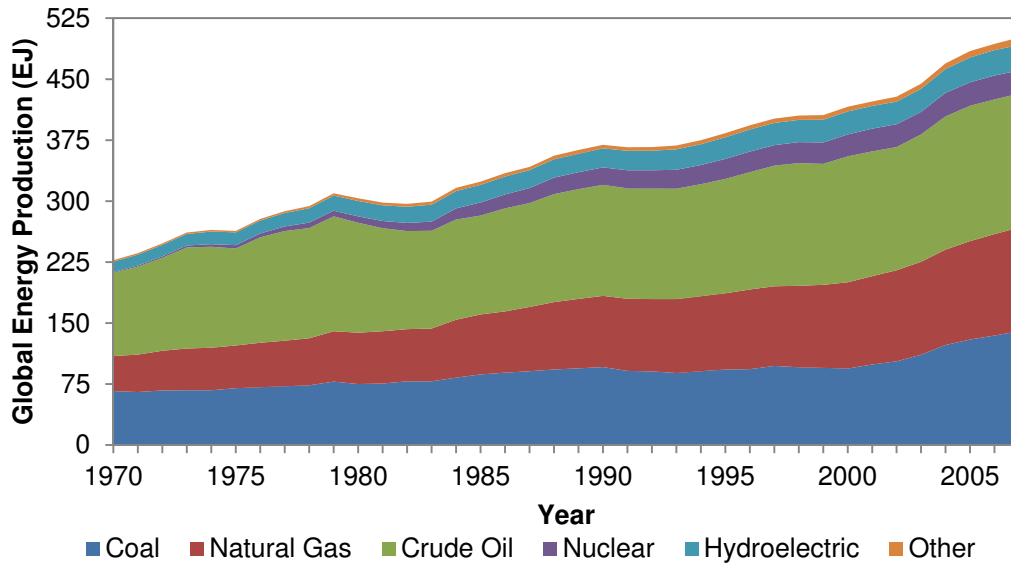


Figure 1: Total global primary energy production by source, 1970-2007 [35]

Figure 2 shows the relative contribution of several sources to global primary energy production between 1970 and 2007. Although the total contribution from fossil fuels decreased only slightly over this span, the relative contribution of the fossil fuels changed dramatically. The contribution of coal was relatively stable around 26%, but the contribution of natural gas grew steadily from 18.9% in 1970 to 25.4% in 2007 and the contribution of crude oil decreased steadily from 45.1% in 1970 to 32.8% in 2007. The contribution of clean technologies (i.e., nuclear, hydroelectric and renewables) more than doubled from 6.8% in 1970 to 13.8% in 2007. It is noteworthy that increases in electricity production from nuclear energy accounted for more than three-quarters of this increase. These results indicate some changes resulting from environmental concerns (i.e., crude oil contributed less, while natural gas and nuclear contributed more), but show that a dramatic shift to primary

energy production via clean energy sources has failed to occur. Energy consumption is expected to continue to grow to support an increasing standard of living for the world's population, which is also growing. Providing this energy to the world's population without causing irreparable damage to the environment will be one of engineering's grandest challenges of the 21st century.

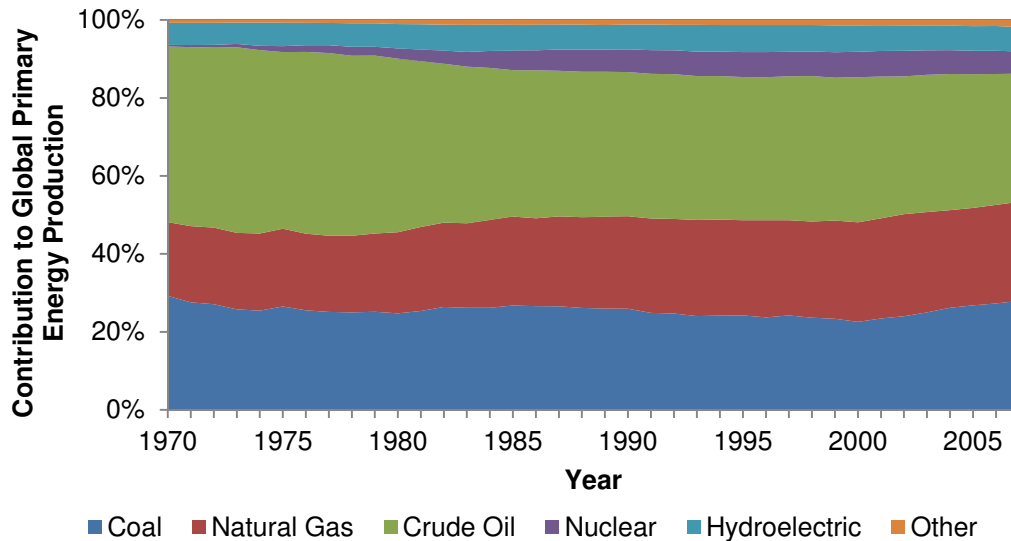


Figure 2: Relative global primary energy production by source, 1970-2007 [35]

Electricity Generation in the United States

Electricity Flow

Electricity generation requires the extensive use of primary fuel sources. The growing demand for electricity coupled with the inefficiency of the conversion of primary fuel sources to electricity lead to significant energy requirements for electricity generation, as can be seen in Figure 3. Of the 41.0 EJ consumed to generate electricity, only 14.2 EJ of net electricity was generated, indicating an efficiency of 34.7%. End uses of electricity account for 13.5 EJ, of which the residential sector consumes 36.4%, the commercial sector consumes 35.3% and the industrial sector consumes 23.6%. Transportation and direct uses (i.e., self-generated

electricity produced by the same entity that consumes the electricity) have modest contributions of only 0.2% and 4.5%, respectively. The industrial sector can achieve energy efficiency improvements through material and manufacturing method selection. Regardless of the end use sector, improving the efficiency of the electricity generation process is critical to maintaining high standards of living while reducing greenhouse gas emissions resulting from electricity generation. Improvements in efficiency are especially important due to the source of the generated electricity, with fossil fuels constituting 67.1% of primary fuel usage for electricity generation [35].

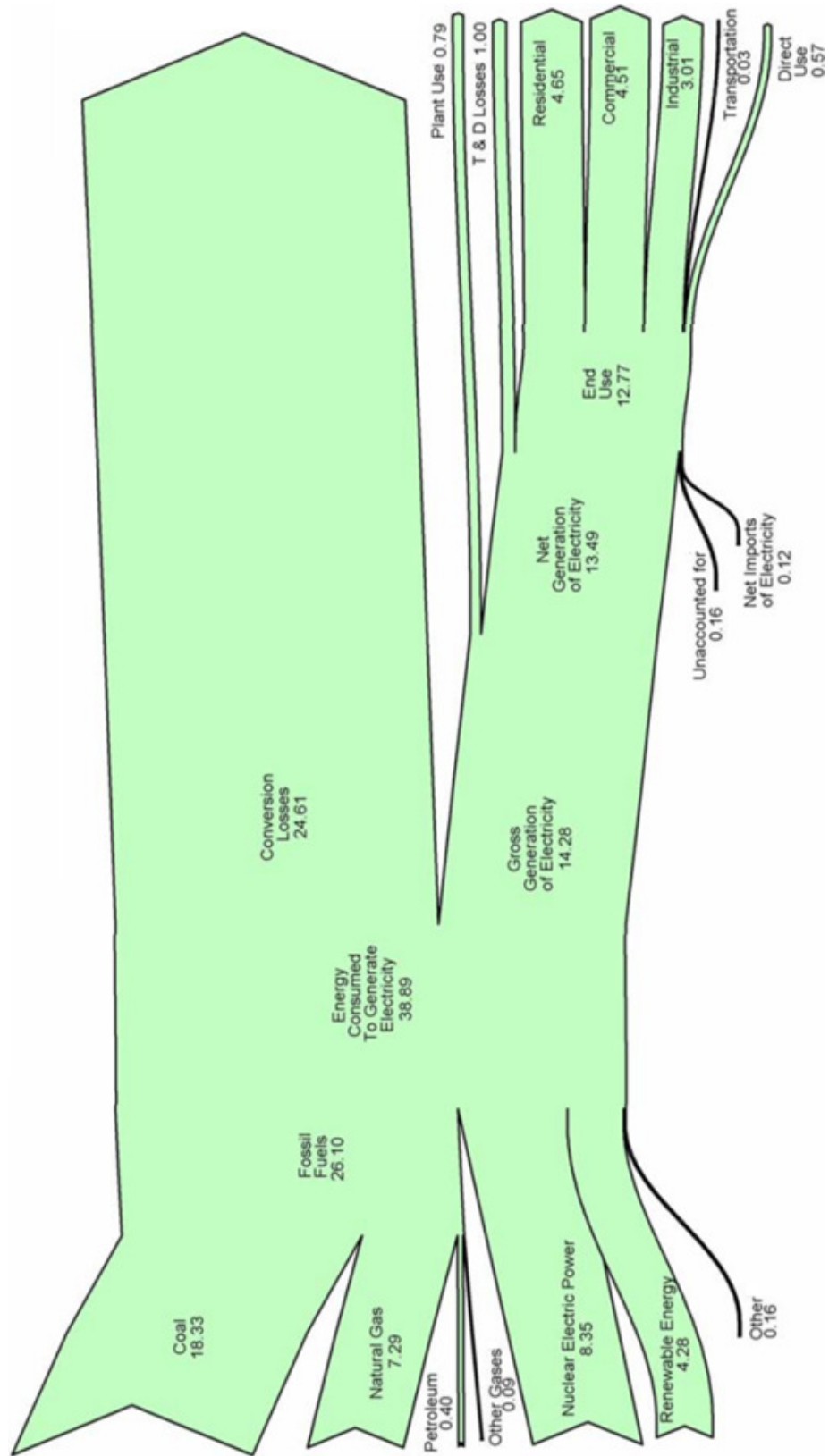


Figure 3: Electricity flow in the United States, 2009 (units: quadrillion Btu) [35]

Trends in Electricity Generation

Electricity generation in the United States has increased dramatically from 10.93 EJ in 1990 to 14.22 EJ in 2009, an average increase of 1.6% annually [36]. The overwhelming majority of electricity generated came from thermoelectric, fossil fuel – primarily coal and natural gas – power plants, which accounted for more than 70% of the generated power during this period, as shown in Figure 4.

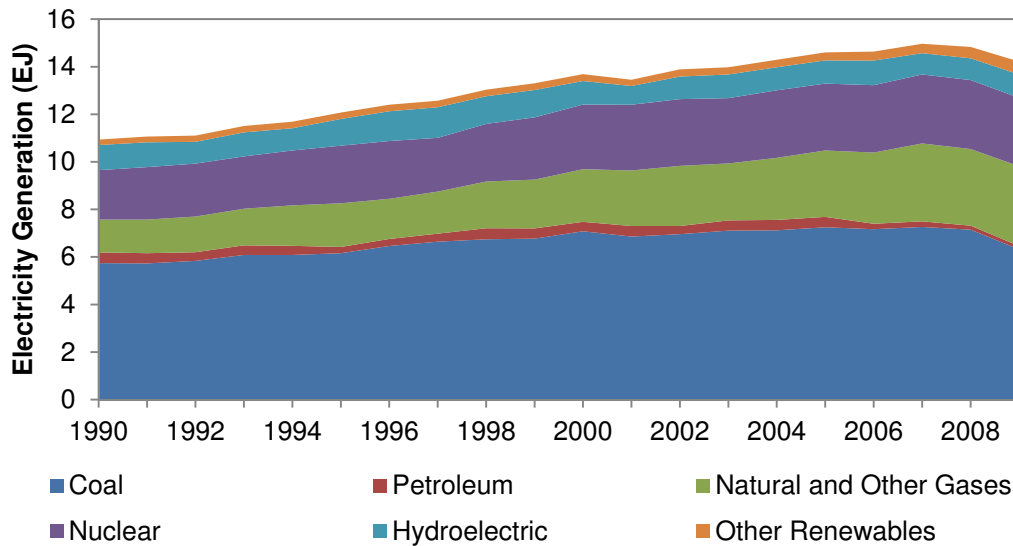


Figure 4: Electricity generation in the United States by source [36]

The trends from Figure 4 also show the recent decline in electricity generation at coal power plants (a decrease of 11.6% from 2008 to 2009, thus accounting for 44.5% of total generation in 2009) and increase in generation at natural gas power plants (an increase of 4.3% from 2008 to 2009, thus accounting for 23.3% of total generation in 2009). These trends reflect the increase in delivered coal prices and the decrease in delivered natural gas prices, as well as the cost of compliance with current environmental regulations [36]. Renewables, other than hydroelectric power, increased 19.8% in 2008 and 14.4% in 2009, enhancing the contribution of this sector that has grown 87.2% since 1998. These trends in generation as well as the

installation of new emission control devices have led to decreased emissions from electricity generating facilities, as shown in Figure 5 and Figure 6. Although total generation increased 9.1% from 1998 to 2009, carbon dioxide emissions from electricity generation were reduced by 3.5%, sulfur dioxide emissions were reduced 55.7% and nitrogen oxides emissions were reduced 62.9%.

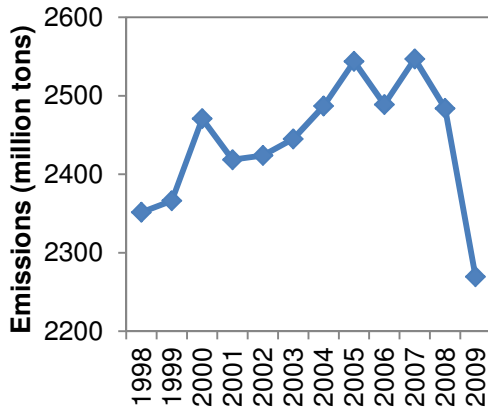


Figure 5: CO₂ emissions from electricity generation [36]

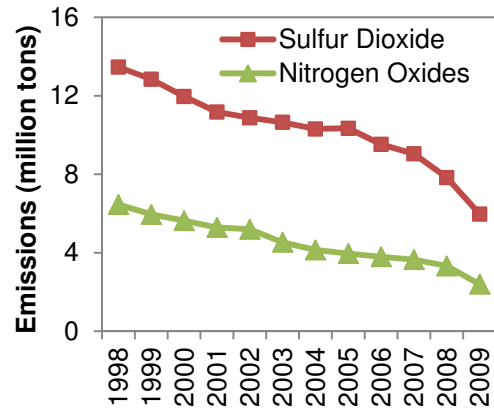


Figure 6: SO₂ and NO_x emissions from electricity generation [36]

It is expected that electricity generation will continue to grow and projections to 2035 are available. Based on Energy Information Administration estimates, electricity generation including net imports is expected to grow from 14.45 EJ in 2009 to 15.43 EJ in 2015 to 16.93 EJ in 2025 to 18.65 EJ in 2035 [37]. This growth will generate new challenges as the U.S. attempts to meet increasing demand while reducing emissions and supplying freshwater for irrigation and domestic uses.

Water Use

Current trends in water use show that demands on the United States' water supply are growing, while storage capacity of surface water is becoming more limited and ground water is being depleted [38]. Water supply issues are exacerbated by strong population growth in water-scarce areas, such as in Nevada and Arizona,

where populations grew 32.3% and 28.6%, respectively, between April 2000 and July 2009 [39]. Figure 7 shows water withdrawals in the United States by end use, revealing that withdrawals for cooling of thermoelectric power plants accounted for 49% of all withdrawals in 2005 [40]. Although withdrawals were greatest for the thermoelectric cooling sector, consumption of this sector was less than 3% of total consumption, with consumptive uses being dominated by irrigation and public supply end uses [40]. Note that according to the United States Geological Survey, withdrawal is defined as water removed from the ground or diverted from a surface-water source for use, while consumption is defined as the part of water withdrawn that is evaporated, transpired, incorporated into products or crops, consumed by humans or livestock or otherwise removed from the immediate water environment [40]. It must be noted, however, that water withdrawn for power plant cooling cannot directly re-enter the domestic water supply and must be treated or allowed to re-enter the natural water cycle before becoming available for irrigation or domestic uses.

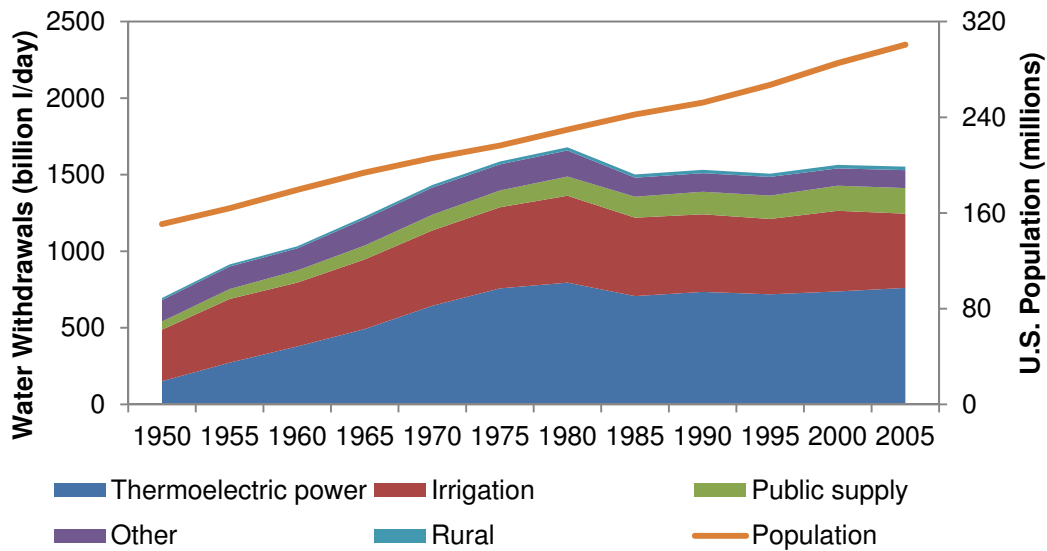


Figure 7: Water withdrawals in the United States by end use [40]

Current withdrawals for cooling of thermoelectric power plants include modest use of saline water. Surface water was the source for 99% of total withdrawals for thermoelectric cooling and 28% of the surface water withdrawn for thermoelectric cooling was saline [40]. Saline surface water withdrawals for thermoelectric power accounted for 93% of total saline withdrawals for all categories [40], which demonstrates that thermoelectric cooling is one of the few end uses that can operate while using saline water. However, recent history suggests that the thermoelectric power industry is not focusing on the use of saline water. Between 2000 and 2005, total withdrawals for thermoelectric cooling increased by 3%, of which freshwater withdrawals increased 7%, whereas saline withdrawals decreased 4% [40]. It is evident that thermoelectric cooling is a significant market for the use of saline water, although this resource is not being fully utilized because of the difficulties associated with the use of saline water (e.g., corrosion and elevated biological activity [41]).

Electricity Generation and Water Use Nexus

Cooling of Thermoelectric Power Plants

The relationship between electricity generation and water use is largely the result of the need for cooling water for condensing steam in thermoelectric power plants. Thermoelectric power plants rely on the heat generated by combustion of a fuel resource (e.g., fossil or biomass) to evaporate water at high temperature and high pressure, after which the steam expands through a turbine connected to a generator to produce electricity. After leaving the turbine, low-pressure steam must be condensed before returning to the evaporator and thus, cooling water is fed through a condenser

to remove heat from the steam. Cooling water mass flow rates can be 50 times or more as high as steam mass flow rates depending on the allowable temperature rise of the cooling water, which is typically 8-14°C [42]. Figure 8 provides a breakdown of common cooling systems for thermoelectric power plants and Figure 9 shows the breakdown of currently installed cooling systems on thermoelectric power plants in the United States. The following section discusses each cooling technology and discusses the breakdown of cooling technologies shown in Figure 8.

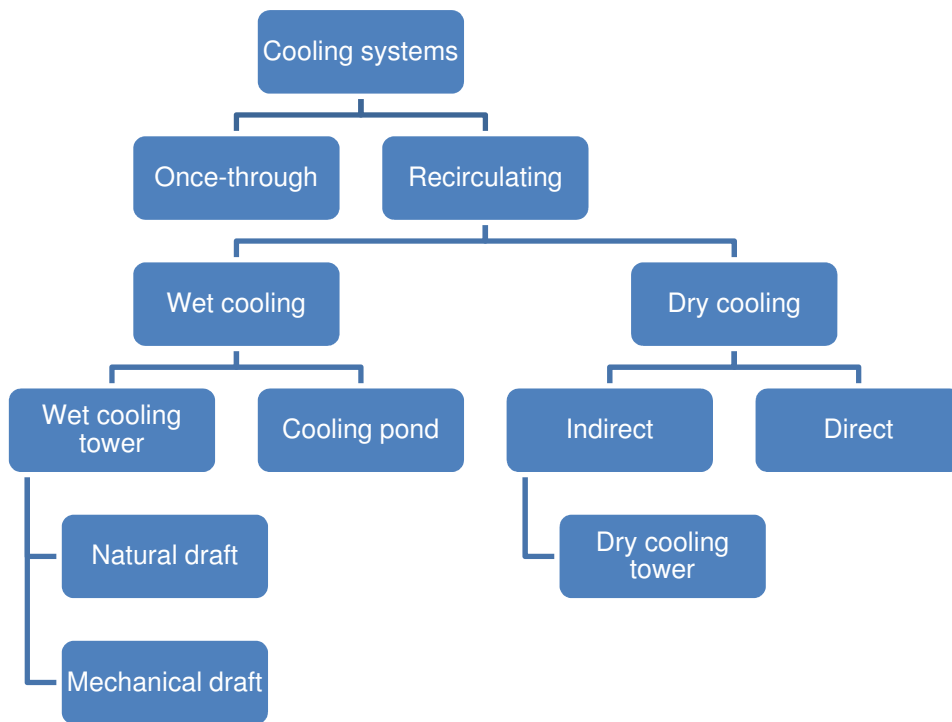


Figure 8: Cooling systems for thermoelectric power plants [43]

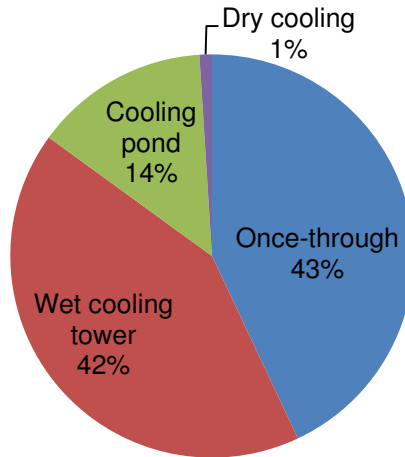


Figure 9: Current cooling systems for thermoelectric power plants [44]

Types of Cooling Systems

Once-Through Systems

In once-through systems, cooling water is withdrawn from a local body of water, it passes through the condenser and then is returned to the same body of water at a higher temperature. Once-through systems have high water withdrawals but relatively low consumption. These systems require specially designed intake and outfall structures to prevent intake of debris and ensure that the water is returned at an optimal velocity and optimal depth within the thermal discharge limit [45].

Wet Recirculating Systems

Recirculating systems can be either wet or dry, with current implementation heavily favoring wet recirculating systems that can be either wet cooling towers or cooling ponds. Wet cooling towers dissipate heat from the water used to condense the low-pressure steam to cooler ambient air flowing through the cooling tower. During this process, some water is lost to evaporation, which then also requires a portion of the water to be discharged from the system (i.e., blowdown) to prevent the

accumulation of minerals and sediment in the cooling water [42]. Wet cooling towers can be either mechanical draft or natural draft, with the difference being that mechanical draft systems use a fan to force air through the tower whereas natural draft systems rely on the density difference between the warm air in the tower and the cool ambient air outside the tower to draw air through the tower [42]. Cooling ponds are manmade bodies of water located near thermoelectric power plants that transfer heat from the cooling water to the environment primarily via evaporation, with some heat transfer by conduction to the ground and convection to the air. Wet recirculating systems have increasingly been installed on thermoelectric power plants because they require fewer withdrawals than once-through systems. However, as a result of wider implementation of wet recirculating systems, total water consumption for thermoelectric power, which currently accounts for 3% of total United States water consumption, is expected to escalate [40,44].

Dry Recirculating Systems

Dry recirculating systems can be either indirect or direct systems. Direct dry systems force the steam leaving the turbine to pass through an air-cooled condenser where the steam is cooled primarily via convective heat transfer to ambient air, which passes through the condenser at high flow rates. Water is not required for direct dry recirculating systems. Indirect dry recirculating use a cooling water loop to condense the steam from the turbine and a dry cooling tower to remove heat from the cooling loop water. Although indirect dry cooling systems rely on a cooling water loop, the loop is closed, which means that there are no losses to evaporation [45].

Cooling System Effects on Power Plant

The relative power output per unit of fuel and installed cost of thermoelectric power plants are dependent on the selected cooling method, as shown in Figure 10. Once-through systems have the highest power output and lowest installed cost because they have the lowest heat sink temperature and most compact cooling solution [45]. Dry cooling systems have lower efficiency than wet cooling towers or once-through systems because of parasitic losses from operation of the cooling system (i.e., fan blowing) [46]. These systems are also expensive because they require larger structures to dissipate the heat because of the poor performance of air as a heat transfer fluid.

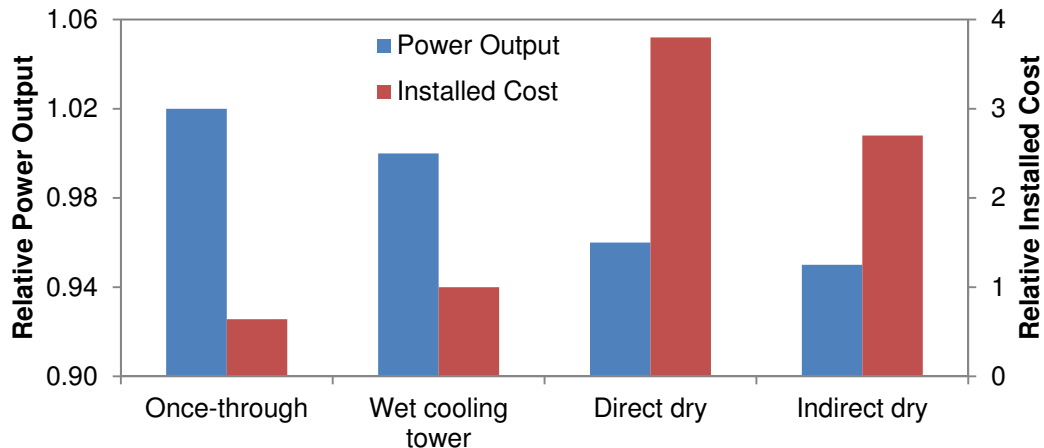


Figure 10: Power output and cost of power plants based on cooling system [45]

Cooling method selection has important implications on the life-cycle water use of power plants. Fthenakis and Kim [38] studied the life-cycle water withdrawals for various fuel cycles, incorporating withdrawals for extraction and processing of fuels and manufacturing. Their results, shown in Figure 11, reveal that recirculating and cooling ponds generally require less withdrawals than once-through systems and that high efficiency cycles, such as those for natural gas combined cycles, reduce

water use. It is noteworthy that water withdrawals for biomass power plants vary widely based on the irrigation requirements of the crops, which is a function of growth location. Other renewable sources, such as photovoltaics and wind, demonstrate multiple benefits by reducing emissions and reducing water withdrawals for electricity generation. Fthenakis and Kim considered only withdrawals because there was minimal information available regarding upstream consumptive water usages [38]. Nonetheless, their results demonstrate the importance of both selecting a generation source and the cooling method for that source.

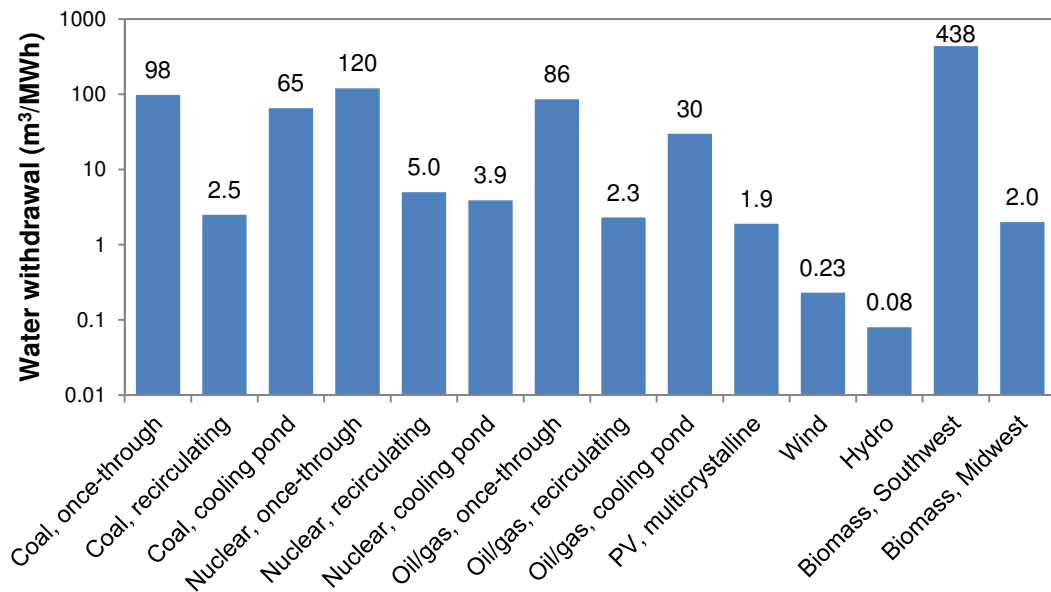


Figure 11: Water withdrawals across fuel cycles [38]

It is anticipated that water withdrawals for fossil fuel fed thermoelectric power plants will increase in the future due to carbon sequestration practices. A report from the National Energy Technology Program estimated that carbon capture based on monoethanolamine scrubbing to remove carbon dioxide would increase water withdrawals by 90% in subcritical pulverized coal power plants, 87% in supercritical pulverized coal power plants, 45% in integrated gasification combined cycle power

plants and 79% in natural gas combined cycle power plants [44]. Based on these findings, as generation facilities are retrofitted to reduce emissions, water resources will become further constrained, thus motivating the search for technologies and materials that can enable the use of saltwater for thermoelectric cooling.

Potential Applications for Polymer Composite Heat Exchangers

Polymer composite heat exchangers (PCHXs) can play an important role in the future of energy-water issues because they offer corrosion resistance, low embodied energy and ease of manufacturability, while providing adequate thermal conductivities and strengths, that will allow for the fabrication of inexpensive, low embodied energy heat exchangers for corrosive environments. Heat exchangers that can operate in corrosive environments are useful for cooling of thermoelectric power plants using saltwater, geothermal and ocean thermal power generation, desalination, chemical processing and waste heat recovery. Please note that while freshwater supplies are considered constrained, the availability of saltwater is nearly unlimited [38]. If 25% of current freshwater recirculating systems were replaced with once-through seawater cooling, made possible by PHX technology, the U.S. electric grid would gain 1.47 GW of generating capacity without construction of additional power plants. It is noteworthy that this figure does not account for temperature differences between freshwater and seawater, which could lead to increased generation because the seawater could be cooler. This transition would also eliminate freshwater withdrawals and consumption at these facilities. Beyond thermoelectric cooling applications, PHXs could lead to significant efficiency improvements through waste

heat recovery and the embodied energy of these heat exchangers will be much lower than their metallic counterparts.

The availability of carbon fiber enhanced polymers that are stiffer, stronger and more thermally conductive, yet energy-efficient could provide new opportunities in the design of corrosion-resistant heat exchangers. Heat exchangers fabricated from carbon fiber enhanced polymers, relative to conventional corrosion-resistant metallic alloys, are expected to have enhanced resistance to corrosion and scaling, lower costs, greater geometric flexibility and lower embodied energy. For heat exchangers operating with corrosive fluids, significant energy gains can be achieved by increasing the heat exchanger service life through material substitution. Furthermore, it is expected that the low energy of fabrication and formation for polymer materials may lead to considerable energy savings over the lifetime of the heat exchanger [34].

Energy savings from material selection, fabrication and formation have only recently been considered in heat exchanger design. The more conventional approach was to reduce pumping power requirements, which have a larger impact on lifetime energy consumption of conventional heat exchangers due to their longer service lives that are often 20 years or longer. In heat exchange applications involving corrosive fluids, where heat exchanger service life is limited and energy intensive alloys are often required, the energy required for the raw material and fabrication of the heat exchanger can represent a significant fraction of its total energy [34]. In the future, significant energy savings can be achieved by reducing embodied energy of commercial and industrial products, such as heat exchangers.

Overview of Thesis

Fiber-reinforced polymer composites with enhanced thermomechanical properties are a promising heat exchanger material. However, significant work must be completed to demonstrate the viability of such composites before they gain industry acceptance. The objective of this thesis is to continue the trend toward such acceptance, through the following assessments:

1. Demonstrate potential freshwater and energy savings resulting from implementation of polymer composite heat exchangers.
2. Assess the thermomechanical material properties of a commercially available polymer composite that could be implemented as a heat exchanger material.
3. Quantify the effect of hygrothermal aging on a raw polymer and a carbon fiber-reinforced polymer composite.
4. Develop a finite element model capable of assessing the structural and thermal performance of anisotropic polymer composite heat exchanges exposed to thermomechanical loading.
5. Understand the effects of anisotropic thermomechanical properties present in polymer composites on structural and thermal performance of polymer composite heat exchangers.

This thesis provides an overview of the characterization of polymer composites, the development of a finite element model for heat exchangers fabricated from polymer composites, and the analysis of the structural and thermal performance of such heat exchangers in specific operating conditions. Divided into eight chapters, the thesis begins by introducing applications of the heat exchangers being presently

studied and explores the motivation behind this work. Chapter 2 discusses the thermomechanical properties of polymers and how these properties change after the addition of filler materials. Chapter 3 provides a methodology for the calculation of the properties of composite materials. Chapter 4 presents the design of environmental test chambers and the change in mechanical properties of raw and reinforced polymers resulting from the hygrothermal effect. Chapter 5 details the development of a finite element model for characterization of the mechanical behavior of polymer composite heat exchangers exposed to pressure loading. Chapter 6 presents the adaptation of the model developed in Chapter 5 to thermal analysis and analyzes the heat transfer rate of corrosion-resistant polymer, polymer composite and metallic heat exchangers. Chapter 7 builds on Chapters 5 and 6 by incorporating both structural and thermal loading to characterize the thermomechanical behavior of an isotropic metallic and anisotropic polymer composite heat exchanger model. A summary of contributions and proposed future work is discussed in Chapter 8.

Chapter 2: Polymers and their Composites

Introduction

Polymers are an important group of raw materials implemented in an array of manufacturing operations. Products fabricated from polymers include food storage containers, large chemical storage tanks, domestic water piping systems, industrial piping systems for highly corrosive fluids, toys and boat hulls, along with a multitude of other products [47]. Polymers generally possess the advantages of being lightweight, easy to manufacture, low cost and corrosion resistant, when properly designed and applied.

Types of Polymers

The three general categories of polymers are thermoplastic polymers (thermoplastics), thermoset polymers (thermosets) and elastomers (rubbers). Common polymers of each type are shown in Figure 12. Thermoplastics are polymers that can be easily formed by heat and pressure at temperatures above their glass transition temperature. Thermoplasts can be reheated and reformed and thus, they can be recycled. Thermosets are polymers that assume a permanent shape when heated and thus, they cannot be recycled. Thermosets begin as powders or liquids that, when reacted with a second material, result in a new material whose properties differ from those of both starting materials. Elastomers are polymers that deform dramatically when loaded with relatively modest forces, but which return to their original dimensions when the forces are released.

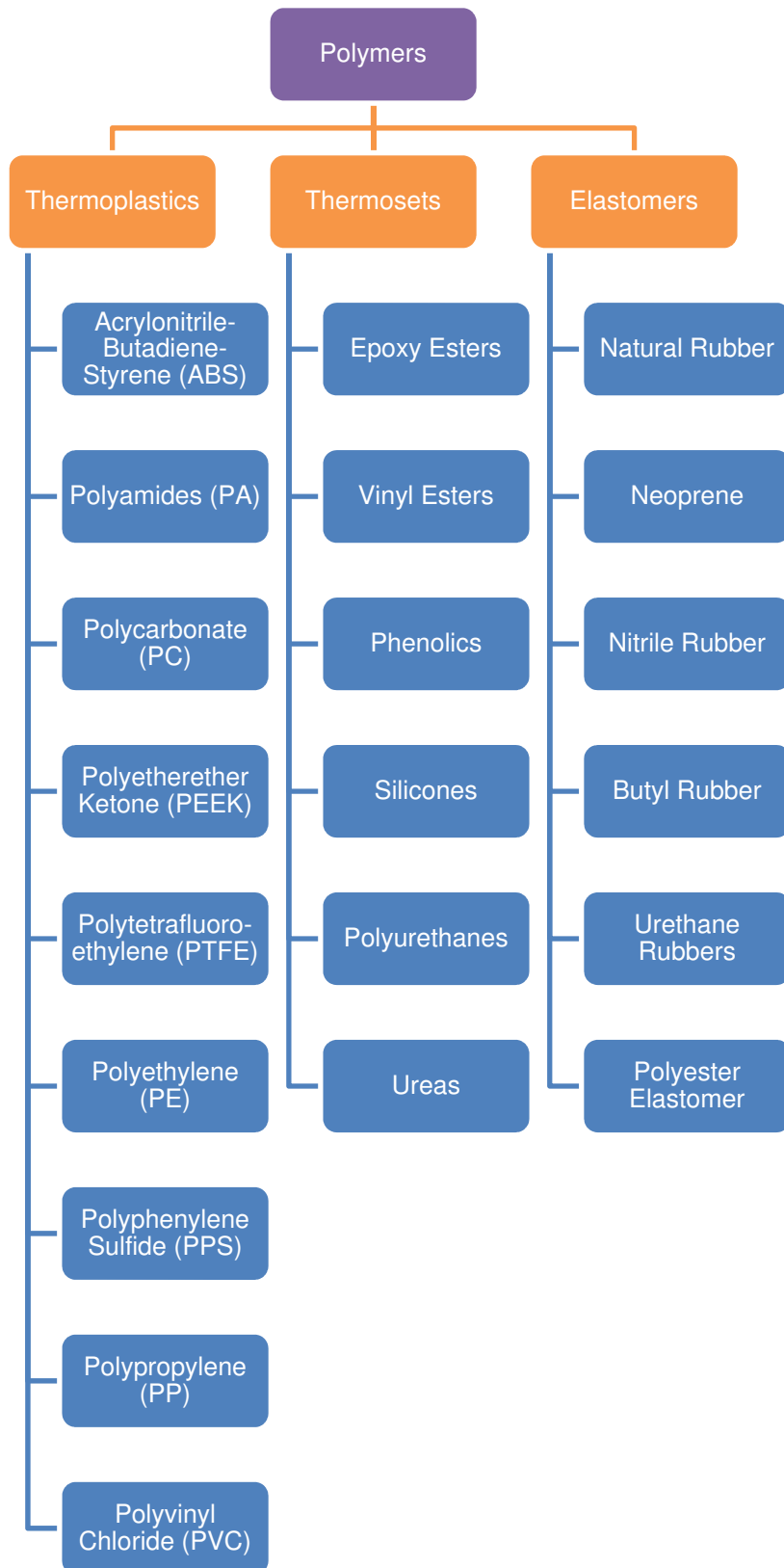


Figure 12: Common polymers by type

Properties of Polymers

General Behavior

Polymers are viscoelastic, meaning that they have the characteristics of both a viscous liquid and a spring-like elastomer. When subjected to modest loads for a short duration, polymers behave like a spring and return to their original dimensions when the load is removed. Long-term heavy loading or loading during exposure to elevated temperatures causes polymers to behave like a highly viscous liquid, in which the polymer chains slip and do not return to their original locations when the load is removed. While undergoing this permanent deformation, the strain resulting from a constant applied stress increases with time as a nonlinear function [47].

Compared with other material classes (e.g., ceramics and metals), polymers exhibit low densities and elastic moduli roughly 50 times less than those of metals [17]. However, due to their low densities, polymers can achieve strength per unit weight ratios comparable to those of metals. The environmental temperature must be considered when using polymers because they can be brittle at temperatures below 0°C and can lose much of their mechanical stiffness and strength at temperatures above 150°C. Despite these considerations, polymers have significant advantages relative to other materials, including their geometric flexibility, ease of manufacture, low cost and corrosion resistance.

Thermoplastic Polymers

Advantages

Thermoplastic polymers have several advantages relative to other polymers, especially when considering the application of polymers to heat exchangers. Polymer

engineering led to the development of high stability, higher performance thermoplastic polymers, which have improved mechanical and physical properties relative to other polymers. Thermoplastic polymers can also be easily reinforced with fillers (e.g., carbon or glass) to further enhance their structural stability and mechanical properties. Moreover, thermoplastic polymers can be reshaped and recycled more easily than other polymers and can be processed with screw injection molding technology, which allows for high volume, low cost production of these polymers [47].

Physical and Mechanical Properties

The properties of common thermoplastic polymers are shown in Table 4. Please note that the properties shown are for acrylonitrile butadiene styrene (ABS), polyamide 6 (PA6, nylon), polycarbonate (PC), polyether ether ketone (PEEK), polytetrafluoroethylene (PTFE, Teflon), high-density polyethylene (HDPE), polyphenylene sulfide (PPS) and polypropylene (PP).

Table 4: Physical and mechanical properties of thermoplastic polymers [47.48]

Property	ABS	PA6	PC	PEEK	PTFE	HDPE	PPS	PP
Density (kg/m ³)	1020-1080	1120-1140	1200	1300-1320	2140-2200	952-955	1350	890-905
Water abs. (24 hr. at 23°C) (wt. %)	0.20-0.45	1.30-1.90	0.15	0.50	0.01	>.01	0.01-0.07	0.03
Failure strength (MPa)	17-55	41-165	63-72	100	21-34	22-31	48-86	28-45
Tensile modulus (GPa)	0.9-2.9	2.6-2.8	2.4	3.6	0.4-0.6	1.1	3.3	0.2-0.3
Elongation at break (%)	20-100	30-100	110-120	50	200-400	10-1200	2	200-500
CTE (µm/m/°C)	108-234	144-149	122	5-11	126-216	106-198	49-88	122-171

k (W/m·K)	0.17-0.19	0.24	0.20	0.26	0.25	0.46-0.50	0.08-0.29	0.15-0.17
Deflection temp. (1.8 MPa) (°C)	77-104	68-85	121-132	160	46	47	100-135	54-60
Deflection temp. (0.46 MPa) (°C)	77-113	175-191	138-197	Not available	71-121	79-91	199	85-104
Max. operating temp. (°C)	85	79-150	120-135	250	260	80	230	93

As shown in Table 4, the density of common thermoplasts is between 900 and 1200 kg/m³, with the notable exceptions of PEEK and PPS, which are slightly denser, and PTFE, which is much denser. The water absorption of many thermoplastics is low, although several types (e.g., ABS, PA and PEEK) absorb water more readily than others. In general, thermoplastic polymers have modest failure strength and stiffness (~ 30 MPa and < 1 GPa, respectively), but some (e.g., PA, PC, PEEK and PPS) exhibit high strength and stiffness. It is noteworthy that PPS has very high stiffness among thermoplasts but it suffers from limited elongation before break. The coefficients of thermal expansion (CTEs) of thermoplastic polymers are generally between 100 and 200 µm/m/°C, although PEEK and PPS exhibit CTEs much below this typical range.

The thermal conductivity of thermoplastic polymers is generally around 0.20-0.30 W/m·K, which constrains their performance in heat transfer applications unless very thin walls are implemented, since the one-dimensional conduction thermal resistance is proportional to wall thickness and inversely proportional to material thermal conductivity. The deflection and operating temperatures of thermoplastic polymers are also of concern in heat transfer applications due to their relatively modest values. Several thermoplastic polymers have deflection and operating

temperatures below 100°C, although some thermoplasts (e.g., PEEK, PTFE and PPS) have operating temperatures above 225°C. It is noteworthy that the high operating temperature of PTFE (260°C) is constrained by the poor mechanical properties of this material, which leads to deflection temperatures of 46°C when loaded at 1.82 MPa and 71-121°C when loaded at 0.46 MPa.

Polymer Reinforcements

In the present study, polymers are not considered as raw materials for heat exchangers due to their low thermal conductivity, low strength and low stiffness. The addition of filler materials to the polymer matrix enhances these properties and could allow for competitive performance with metals while offering lower cost, easier manufacturing, lower density and lower embodied energy. Other benefits of reinforced polymers include increasing dimensional stability, increasing toughness and improving heat resistance [16]. Many reinforcements have been successfully integrated with a polymer matrix and a few of the most common reinforcements are described in the following section.

Types of Reinforcements

Polymer reinforcements can take several forms, the most common of which are particles, flakes, fibers and laminas (see Figure 13). Fiber reinforced composites were selected for the present study due the great extent to which their properties can be tailored. Mechanical and thermal properties of fiber-reinforced composites can be controlled by the chosen fiber, matrix, processing option and the manner in which the constituents are put together [49]. This ability to control the properties of the composite is particularly attractive because it makes it possible to

select the minimum fiber content needed to achieve the required properties, leading to composites that have lower cost and lower embodied energy. Short fibers (i.e., fibers with lengths less than 10-15 mm) are a particularly attractive filler material because composites comprised of a polymer matrix and short fibers can be fabricated via mass production (e.g., injection molding and extrusion), whereas composites with long fibers require nonautomated or semiautomated processes (e.g., hand layup, spray-up, rotomolding, compression and transfer molding) [16]. Although short fibers are advantageous in terms of manufacturing and thus, cost, the decrease in fiber length reduces the composite's average thermal conductivity by increasing the conduction length in the matrix and magnifying the effect of the thermal contact resistance at the polymer-filler interface. The magnitude of this latter effect is not well understood nor is it easy to evaluate, but Lipton and Vernescu [50] have shown that the appearance of a resistance at the phase contact reduces the effective conductivity of a composite, especially when the size of the inclusions decreases. The following sections provide a brief overview of the most common fiber reinforcements: glass, aramid, and carbon.

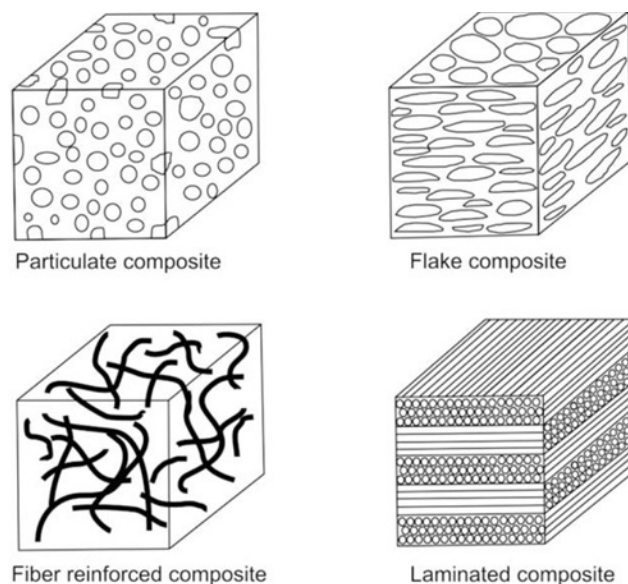


Figure 13: Composite materials with different forms of constituents [51]

Glass Fibers

The most widely used reinforcement material for polymer materials is glass [16]. In general, glass is relatively weak, has a high coefficient of thermal expansion and has very low thermal conductivity. Some variations of glass fibers have higher strengths and lower coefficients of thermal expansion, with common choices being borosilicate glass and E-glass [52]. The strongest known glass fibers are made from pure silica and can have strengths as high as 9.6 GPa at liquid nitrogen temperatures [52]. Regardless of the type of glass fiber used, care must be taken to avoid surface damage because contact among fibers can lead to cracks that severely reduce the strength of the fibers. Despite their limitations, glass fibers have been widely used because of the strength and stiffness enhancement they offer at low cost, which can be as low as \$1/kg [52].

Aramid Fibers

Aramid fibers, such as Kevlar, have very high tensile strength, a high elastic modulus, a very low coefficient of thermal expansion and excellent corrosion resistance [52]. The primary disadvantages of aramid fibers are their very low compressive strength and their ability to absorb moisture, although their absorption of water does not have a significant effect on their strength [52]. The most common inclusion of aramid fibers in polymer fiber composites are with thermoset polymers, such as epoxy and phenolics. The cost of Kevlar fibers can be about \$20/kg, although higher modulus versions can cost \$30 or more per kg [52].

Carbon Fibers

Carbon fibers offer very high elastic modulus and strength per unit mass, as well as excellent corrosion and fatigue resistance properties [52]. Carbon fibers offer very high thermal conductivities, making these fibers attractive for application such as heat exchangers. The addition of carbon fibers to a polymer matrix also increases the heat deflection temperature of the polymer, which is also useful in heat exchanger applications. The primary disadvantage of carbon fibers is their high cost, which is approximately \$25/kg for the lower modulus and strength materials, although their low density relative to glass fibers helps to offset some of the cost [52].

Summary of Fiber Properties

Table 5 provides a summary of the mechanical and thermal properties of the fibers described earlier. Carbon fibers have the highest elastic modulus and highest operating temperature, while still offering modest density and excellent corrosion resistance. Furthermore, carbon fibers offer the highest thermal conductivity of the common reinforcement fibers. Based on these properties, carbon fibers were selected as the most appropriate reinforcement material for a polymer composite heat exchanger application.

Table 5: Properties of common fibers [52]

Type of Fiber	Material	Density (kg/m ³)	Strength (GPa)	Elastic Modulus (GPa)	Maximum Temperature (°C)
Glass	E-glass	2540	3.40	72	550
	S-glass	2480	4.80	85	650
	Silica	2200	3.45	69	1070
Aramid	Kevlar 49	1440	3.60	130	
	Kevlar 149	1470	2.41	160	
Carbon	Carbon P120S	2180	2.20	827	2500
	Carbon HMS	1900	2.30	377	2500
	Carbon T40	1810	5.60	290	2500

Characteristics of Polymer Fiber Composites

Mechanical Properties

The typical change in tensile stress-strain behavior resulting from the addition of fiber reinforcements to a polymer matrix can be seen by comparing Figure 14, which shows the stress-strain behavior for unreinforced polypropylene (PP), with Figure 15, which shows the stress-strain behavior of short glass fiber (SGF) reinforced PP and short carbon fiber (SCF) reinforced PP.

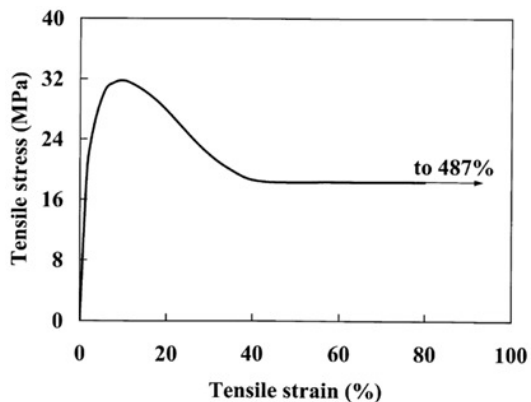


Figure 14: Typical tensile stress-strain curve for unreinforced PP [53]

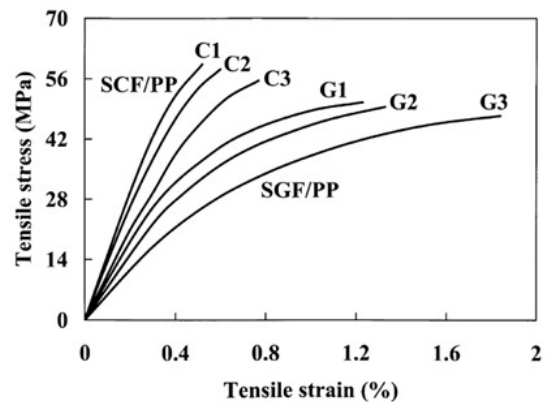


Figure 15: Typical tensile stress-strain curves for SGF/PP and SCF/PP composites (C: carbon, G: glass, 1: 25 vol. %, 2: 16 vol. %, 3: 8 vol. %) [53]

The unreinforced polymer is much more ductile, less stiff and less strong than the fiber reinforced composites, which is the result of the better mechanical properties of the fibers relative to the matrix. Short fiber reinforced polymers exhibit brittle fracture and show linear deformation at lower stresses and nonlinear deformation at higher stresses [53]. The reduction in failure strain is the result of an embrittlement effect caused by matrix crack formation at the ends of the reinforcing fibers [53]. The composite failure occurs when the extent of cracking across the weakest section of a

specimen reaches a critical level when the surrounding fibers and matrix can no longer support the increasing load [54,55].

Reinforcement with carbon fibers leads to high stiffness and strength and lower ductility than seen with glass fibers because carbon fibers are stiffer, stronger and more brittle than their glass counterparts. Higher volume fractions of either glass or carbon fibers lead to stronger, stiffer and less ductile material systems.

Residual Stress

Fiber-polymer composite material systems fabricated via injection molding experience residual stress that develop for several reasons when the molded component cools from its fabrication temperature to ambient temperature. The coefficient of thermal expansion of the polymer matrix is typically much higher than that of the fibers, which leads to residual stresses at the micro scale during cool down because the polymers and fibers, which are interfacially bonded, contract at different rates as the temperature cools [56,57]. Residual stress can also develop from cure shrinkage (i.e., polymers shrink during curing) and the interaction of the material system with the injection mold tooling, which is generally steel or aluminum [57].

Figure 16 shows stresses calculated by micromechanical finite element analysis based on a repeating array of fibers in a carbon fiber/epoxy composite subjected to a 100°C temperature drop [58]. The resulting thermal residual stresses are of compressive nature in the fiber and of tensile nature in the matrix [59]. Hoop tensile stresses arise in the matrix as it shrinks around the fibers, compressive radial stresses develop where the fibers are close together and tensile radial stresses develop where fibers are furthest apart [57]. The von Mises stresses, which are as large as 25

MPa in the case shown, represent a significant fraction of the strength of the matrix material. Depending on the local fiber distribution, the residual stresses can improve or reduce the local ultimate strength of the composite [60]. Due to the complexity of the residual stress development, which is a function of material properties, fiber distribution and interfacial bond strength, and that the residual stresses can augment or reduce ultimate strength, the zero-stress state was considered room temperature (20°C) for the present analysis.

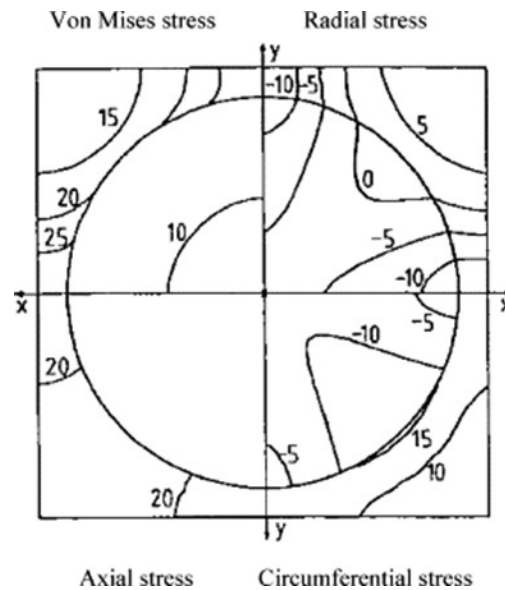


Figure 16: Residual stresses in carbon-epoxy due to 100°C temperature drop (units: MPa) [58]

Fiber Orientation

Fibers in injection molded polymer composites exhibit preferential orientation in the flow direction [61]. Figure 17 shows a scanning electron microscope (SEM) micrograph of the tensile fracture surface of a short carbon fiber (SCF, 8 vol. %) polypropylene (PP) composite, in which the preferential orientation of the fibers in the flow direction can be seen [62]. It is known that in pure shear flow, fibers orient

mainly in the flow direction, whereas in extensional flows, fibers orient in the direction of extension [63]. In many injection-molded components, the thickness is nearly constant and is much lower than other dimensions, which means that shear deformations are dominant and thus, fiber orientation is generally in the flow direction [63].

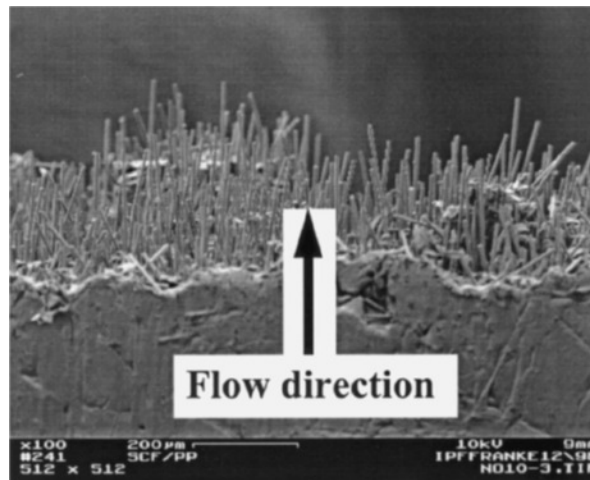


Figure 17: SEM micrograph of tensile fracture surface of an SCF/PP composite with carbon fiber (8 vol. %) [62]

Although flow induced fiber orientation phenomena are well understood by the research community, the details in injection-molded components are not easy to capture [63]. The most common techniques utilized for fiber orientation characterization consist of observing a polished cross section of the molded component using optical or scanning electron microscopy. However, these methods are time consuming and provide only a rough estimate of the fiber state [63]. As such, for simplicity, the present modeling assumes a transversely isotropic material state with the longitudinal composite properties assigned to the expected flow directions (as will be described in more detail later in this document).

Chapter 3: Calculation of Composite Properties

Polymer-Fiber Composite

Both raw and carbon-fiber reinforced polymers were studied to assess the effects of hygrothermal aging on polymers and the effect of the addition of carbon fibers to the matrix. The raw polymer material was commercially available Grilamid L16 Natural polyamide 12 (PA12), which was manufactured by EMS and provided in granular form [64]. The carbon-fiber reinforced material was commercially available Therma-Tech NJ-6000 TC, which was manufactured by PolyOne and provided in granular form [65]. The carbon fibers used for reinforcement of the PA12 matrix were ThermalGraph DKD fibers, manufactured by CYTEC Industries [66]. Carbon fibers constituted 36.6% by volume and 51.8% by weight of the composite. The manufacturer-specified properties of the pitch-based carbon fibers used in the composite material are provided in Table 6.

Table 6: Carbon fiber properties [66]

Parameter	Value
Average Diameter	10 μm
Average length	200 μm
Density	2.15-2.25 g/cm^3
Thermal conductivity	400-700 $\text{W/m}\cdot\text{K}$
Elastic modulus	690-930 GPa
Tensile strength	1380 MPa
Poisson's ratio	0.30

The relevant properties of the matrix material are: elastic modulus of 1.46 GPa (experimentally-determined), Poisson's ratio of 0.41, coefficient of thermal expansion of 130 $\mu\text{m/m}\cdot^\circ\text{C}$ and thermal conductivity of 0.25 $\text{W/m}\cdot\text{K}$.

Polyamides were chosen for the present study because they are commercially available in many filled and reinforced varieties, which allows for appropriate

materials selection based on material requirements. One of the benefits of polymer composites is the ability to tailor physical properties to the application and thus, the proven variety of polyamide composites was attractive. PA12 was selected because it has the lowest equilibrium moisture content among polyamides, which is a result of the combination of the long hydrophobic paraffinic chains between the hydrophilic amide groups and its highest ratio of CH₂ to CONH among polyamides [16,67].

It was important to select a polymer that absorbs moisture to ensure that some change in material properties resulted from hygrothermal aging; as discussed in Chapter 2, some polymers absorb very little or no moisture over time. Furthermore, PA12 was a good candidate for the present study because the hygrothermal aging behavior of a PA66 with high moisture absorption as high as 12% or more by weight was studied previously by Ishak and Berry [68]. In general, it is expected that polymer heat exchangers would be manufactured from materials with modest equilibrium moisture content to minimize the change in material properties and possible deformation (e.g., swelling) that can result from moisture absorption.

The selection of a carbon fiber reinforced PA12 for the present study is not an indication of a preference for the present material for PCHXs. One of the advantages of polymer composites is that their matrix, reinforcement type and reinforcement content can be tailored to achieve the desired properties for a given application. Carbon fiber reinforced PA12 is a material that allowed for the study of hygrothermal aging effects and that represented general properties of polymer composites, but it is expected that other polymers with different fiber sizes and concentration will be more suitable for certain PCHX applications. One of the goals of this work is to provide a

methodology for studying the thermomechanical behavior of polymer composites and thus, this work does not offer a definitive material for PCHXs.

Effective Fiber Modulus

The longitudinal elastic modulus of the considered composite, which was determined experimentally using injection-molded dogbone tensile specimens, was 18.5 GPa. This value is a slightly less than the manufacturer specified modulus of 20.7 GPa [65]. Based on experimental results, the effective modulus of the fibers (E_f) was calculated using the shear-lag model proposed by Cox [67]:

$$E_L = E_f \left[1 - \frac{\tanh\left(\frac{\beta l}{2}\right)}{\frac{\beta l}{2}} \right] V_f + E_m(1 - V_f) \quad (1)$$

$$\beta = \left[\frac{2\pi G_m}{E_f(\pi r_f^2) \ln\left(\frac{R}{r_f}\right)} \right]^{\frac{1}{2}} \quad (2)$$

where E_L is the longitudinal (parallel to the fibers) modulus of the composite, β is the shear-lag parameter, l is the average fiber length, V_f is the fiber volume fraction, E_m is the matrix elastic modulus, G_m is the matrix shear modulus, r_f is the average fiber radius and R is the mean separation of fibers normal to their length. For a square packing arrangement [67]:

$$\ln \frac{R}{r_f} = \frac{1}{2} \ln \left(\frac{\pi}{V_f} \right) \quad (3)$$

The shear modulus of the matrix was calculated according to Equation 4:

$$G_m = \frac{E_m}{2(1 + \nu_m)} \quad (4)$$

where ν_m is the Poisson's ratio of the matrix. The effective fiber modulus was calculated to be 111 GPa, which was well below the manufacturer's specified range of 690 to 930 GPa due to the discontinuous nature of the fibers in the studied composite. According to Cox's shear lag-model, if the fibers had an elastic modulus of 810 GPa (the average of the manufacturer-specified values), an average fiber length of 137 μm would have resulted in the experimentally-determined composite longitudinal elastic modulus of 18.5 GPa.

Anisotropic Mechanical Properties

Several theories exist regarding structural properties of fiber-reinforced composite materials. All of the models for predicting the mechanical properties of short-fiber composites use the same basic assumptions, i.e., the fibers and the matrix are linearly elastic, the matrix is isotropic and the fibers are either isotropic or transversely isotropic; the fibers are axisymmetric, identical in shape and size and can be characterized by an aspect ratio l/d ; and the fibers and matrix are well bonded at their interface and remain fully attached during deformation (thus, the models do not consider interfacial slip, fiber-matrix debonding or matrix micro-cracking) [70].

Tucker and Liang [70] reviewed and evaluated several micromechanics models for the stiffness of aligned short-fiber composites and concluded that the Halpin-Tsai model gives reasonable results for all the elastic constants, except for the transverse Poisson's ratio ν_{TT} , and that the predicted longitudinal elastic modulus E_L values are low for moderate-to-high fiber aspect ratios. In the present study, E_L was determined experimentally from injection-molded specimens configured to provide high orientation and was found to be in good agreement with manufacturer's

specifications. It is noted that it has not proved possible to produce physical samples with perfectly aligned fibers and that even in samples of partially aligned fibers, the fibers may be clustered or bundled together in some unspecified way [71].

In the present study, properties for the polymer-fiber composite were calculated as the average of the properties provided by the Halpin-Tsai and Tsai-Hahn models. A similar process was utilized by Pegoretti et. al [72] in their analysis of short glass fiber composites. For a detailed review of the Halpin-Tsai and Tsai-Hahn equations, see Reference [73] and Reference [74], respectively.

A composite material with uniaxially oriented fibers randomly packed in the cross-section (as in the case for the present study and will be described more thoroughly later in the document) is a particular type of orthotropic material called transversely isotropic. In such materials, the material properties in the longitudinal direction (i.e., parallel to the fibers) are different from those in the two transverse directions (i.e., perpendicular to the fibers). In general, five independent elastic constants are required to describe the elastic behavior of such transversely isotropic materials [75]: the tensile longitudinal modulus (E_L), transverse modulus ($E_T = E_{T'}$), shear modulus ($G_{LT} = G_{LT'}$), Poisson's ratios ($\nu_{LT} = \nu_{LT'}$) and $\nu_{TT'}$, where L stands for longitudinal direction and T and T' refer to two mutually perpendicular directions in the transverse plane.

Transverse Modulus

The transverse modulus (E_T) according to the Halpin-Tsai model was calculated according to Equations 5-6:

$$E_T = E_m \frac{1 + \xi\eta V_f}{1 - \eta V_f} \quad (5)$$

$$\eta = \frac{E_f - E_m}{E_f + \xi E_m} \quad (6)$$

where $\xi = 2$ for fibers with a circular cross-section. The transverse modulus based on the Tsai-Hahn model was calculated according to Equation 7:

$$\frac{1}{E_T} = \frac{1}{V_f + \eta V_m} \left(\frac{V_f}{E_f} + \eta \frac{V_m}{E_m} \right) \quad (7)$$

where V_m is the matrix volume fraction and $\eta = \frac{1}{2}$. It is noteworthy that the transverse modulus equations for both models do not include a term for fiber aspect ratio because the transverse modulus is nearly independent of the fiber aspect ratio [76].

In-plane Shear Modulus

The Halpin-Tsai equations for in plane shear modulus (G_{LT}) are given by Equations 8-9:

$$G_{LT} = G_m \frac{1 + \xi\eta V_f}{1 - \eta V_f} \quad (8)$$

$$\eta = \frac{G_f - G_m}{G_f + \xi G_m} \quad (9)$$

where G_f is the fiber shear modulus and $\xi = 1$ for fibers with a round cross-section.

The Tsai-Hahn equations for in-plane shear modulus are given by Equations 10-11.

$$\frac{1}{G_{LT}} = \frac{1}{V_f + \eta V_m} \left(\frac{V_f}{G_f} + \eta \frac{V_m}{G_m} \right) \quad (10)$$

$$\eta = \frac{1}{2} \left(1 + \frac{G_m}{G_f} \right) \quad (11)$$

Poisson's Ratios

The in-plane Poisson's ratio (ν_{LT}) was evaluated using the rule of mixtures:

$$\nu_{LT} = \nu_f V_f + \nu_m V_m \quad (12)$$

where ν_f is the Poisson's ratio of the fibers. The minor Poisson's ratio $\nu_{TL}(= \nu_{T'L})$ can be obtained by the following relationship:

$$\nu_{TL} = \nu_{LT} \frac{E_T}{E_L} \quad (13)$$

The transverse Poisson's ratio ($\nu_{TT'}$) was evaluated based on Equations 14-15, as proposed by Foye [77].

$$\nu_{TT'} = \nu_f V_f + \nu_m V_m \Phi \quad (14)$$

$$\Phi = \frac{1 + \nu_m - \nu_{LT} \left(\frac{E_m}{E_L} \right)}{1 - \nu_m^2 + \nu_m \nu_{LT} \left(\frac{E_m}{E_L} \right)} \quad (15)$$

Transverse Shear Modulus

The transverse shear modulus ($G_{TT'}$) was calculated according to Equation 16.

$$G_{TT'} = \frac{E_T}{2(1 + \nu_{TT'})} \quad (16)$$

Coefficient of Thermal Expansion

The longitudinal and transverse effective coefficients of thermal expansion (CTEs) of the composite were calculated based on the work of Schapery [78]. Karadeniz and Kumluta [79] found that the Schapery model for longitudinal and transverse CTE showed excellent agreement with numerical results of carbon fiber reinforced epoxy composites. The longitudinal CTE (α_L) was calculated according to Equation 17:

$$\alpha_L = \frac{E_f \alpha_f V_f + E_m \alpha_m V_m}{E_f V_f + E_m V_m} \quad (17)$$

where α_f and α_m are the CTEs of the fiber and matrix, respectively. The transverse CTE ($\alpha_T = \alpha_{T'}$) of the composite was calculated according to Equation 18.

$$\alpha_T = (1 + \nu_f) \alpha_f V_f + (1 + \nu_m) \alpha_m V_m - (\nu_f V_f + \nu_m V_m) \alpha_L \quad (18)$$

Mechanical Properties Summary

Mechanical properties were found by averaging the results of the Halpin-Tsai and Tsai-Hahn models and the results are shown in Table 7. It is to be noted that among the mechanical properties, the transverse elastic moduli and the CTEs display the greatest degree of anisotropy.

Table 7: Composite structural properties

Parameter	Value
E_L	18.5 GPa
E_T	3.2 GPa
G_{LT}	1.01 GPa
$G_{T'T'}$	1.05 GPa
ν_{LT}	0.34
$\nu_{T'T'}$	0.51
α_L	1.98 $\mu\text{m}/\text{m}/^\circ\text{C}$
α_T	122 $\mu\text{m}/\text{m}/^\circ\text{C}$

Anisotropic Thermal Properties

Thermal Conductivity

The composite thermal conductivity (k) was calculated according to the Nielsen model [80] because researchers have concluded that the Nielsen model fits experimental data best for a range of fillers in solid filled composites [81]. The Nielsen model is provided in Equations 19-22:

$$\frac{k}{k_m} = \frac{1 + A_N B \varphi_2}{1 - B \varphi \varphi_2} \quad (19)$$

$$A_N = k_E - 1 \quad (20)$$

$$B = \frac{\frac{k_f}{k_m} - 1}{\frac{k_f}{k_m} + A_N} \quad (21)$$

$$\varphi = 1 + \left(\frac{1 - \varphi_m}{\varphi_m^2} \right) \varphi_2 \quad (22)$$

where k_m and k_f are the thermal conductivity of the matrix and filler, respectively, k_E is the Einstein coefficient, A_N is a parameter based on the fiber aspect ratio, φ_2 is the fiber volume fraction and φ_m is the maximum packing fraction. The A parameter is equal to two times the fiber aspect ratio parallel to uniaxial oriented fibers and A equals 0.5 perpendicular to uniaxial oriented fibers [80]. The maximum packing fraction for three-dimensional random fibers is 0.52 [80].

Figure 18 shows the longitudinal and transverse thermal conductivities provided by the Nielson model as a function of the fiber volume fraction. Please note that the longitudinal thermal conductivity does not reach 10 W/m·K until the fiber volume fraction exceeds 37%. At this concentration, the transverse thermal conductivity is only 0.82 W/m·K. Although composites with very high volume fractions of fibers can achieve desirable thermal and mechanical properties, these composites are brittle, have high embodied energy and high cost. As such, the fiber volume fraction is generally increased just enough to achieved the desired properties.

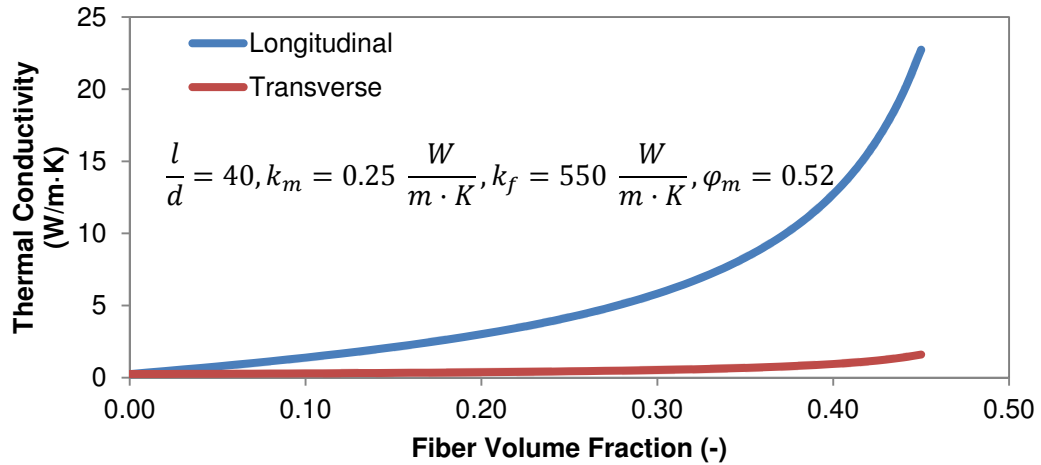


Figure 18: Thermal conductivity based on Nielson model

Based on the assumptions of the Nielson model and the properties of the matrix and fibers for the present material, the longitudinal thermal conductivity was calculated as 9.25 W/m·K and the transverse thermal conductivity was calculated as 0.73 W/m·K. For reference, it is noted that the manufacturer of the composite specified the longitudinal conductivity as 10 W/m·K [65] and did not specify a transverse thermal conductivity.

Chapter 4: Hygrothermal Aging Studies

Motivation

While in operation, polymer composite heat exchangers are exposed to fluids at elevated temperatures. The combined exposure of the material system to humidity and temperatures changes (i.e., the hygrothermal effect) can be more damaging to fiber-reinforced polymers than to either of the components separately [68]. Moisture penetration is conducted primarily by diffusion, although capillarity and transport by micro cracks can occur, usually only after the occurrence of specific damage to the composites, which is in itself a direct consequence of the exposure of the composite to a hot and moist environment [68,82]. The rate of absorption and effect of the moisture on the properties of the composite depend on several factors, which include the matrix and filler materials, fiber orientation and distribution, conditioning temperature and whether the absorbed moisture reacts chemically with the matrix.

Hygrothermal aging can occur chemically or physically. Chemical aging is the result of chemical interactions between the moisture and either the matrix or fiber; the most common chemical aging is the result of hydrolysis of polymer bonds and dissolution and leaching of water-soluble species [68]. Physical hygrothermal aging is reflected in the plasticization of the matrix, which leads to a reduction in its glass transition temperature, elastic modulus and strength [68].

In polymer composites, the polymer matrix is subjected to hygrothermal aging, although it is not expected that hygrothermal aging affects carbon-based filler materials. Hygrothermal aging studies were completed in order to assess the change

in mechanical properties of polyamide 12 (PA12) and fiber-reinforced PA12 resulting from hygrothermal aging in water of various temperatures and salinities. The design of heat exchangers using hygroscopic polymers, such as polyamides, requires careful investigation of the change of mechanical properties as the material absorbs moisture to ensure the long-term structural integrity of the heat exchanger.

Operating Conditions

The Abu Dhabi Gas company, a subsidiary of the Abu Dhabi National Oil Company, processes and distributes natural gas in the United Arab Emirates. Seawater is one coolant used in the liquefaction of natural gas. The water in the Persian Gulf has a mean upper-ocean salinity of as much as 37.1 g/kg and surface temperature as high as 30.9°C [83] and thus, heat exchangers must be fabricated from expensive, corrosion resistant alloys. Fiber reinforced polymers may be able to replace these materials within certain design constraints.

Experimental Setup

Processing

All tensile specimens were injection molded using a Cincinnati Milacron Babyplast injection-molding machine. The molding temperatures, injection pressures and other processing conditions were set as closely as possible to those recommended by EMS and PolyOne for the molding of raw PA12 and reinforced PA12, respectively, as shown in Table 8. Please note that some parameters were not provided by PolyOne and thus, parameters were adjusted based on established injection molding guidelines for composite materials until consistent specimens were produced from the injection molding process.

Table 8: Injection molding parameters for raw and reinforced PA12 [64,65]

Parameter	Grilamid L16 Natural PA12	Therma-Tech NJ- 6000 TC Composite PA12
Nozzle Temperature (°C)	230	--
Mold Temperature (°C)	80	65-93
Melt Temperature (°C)	250	260-277
Injection Speed (-)	low-medium	--
Hold Pressure (bar)	300-800	--
Dynamic Pressure (bar)	5-15	--
Screw Speed (1/min)	50-100	--

Moisture Absorption

All injection molded tensile specimens were dried at 80°C over calcium sulfate until constant weight was attained prior to immersion in water baths. Eight water conditions were selected based on the maximum surface temperature and salinity seen in the Persian Gulf, as reported by Kampf and Sadrinasab [83] and the expected water temperature rise resulting from the heat exchange process. The four temperatures were 25°C, 40°C, 50°C and 60°C and the two salinities were 0 g/kg (i.e., freshwater) and 45 g/kg. Immersion in freshwater and saltwater was studied in order to quantify the effect of the presence of salt relative to the effect of hygrothermal aging in freshwater. The testing conditions were achieved in glass water baths, which were temperature regulated using a controller, immersion heater and pump as shown in Figure 19. The pump served to prevent temperature and salinity stratification.

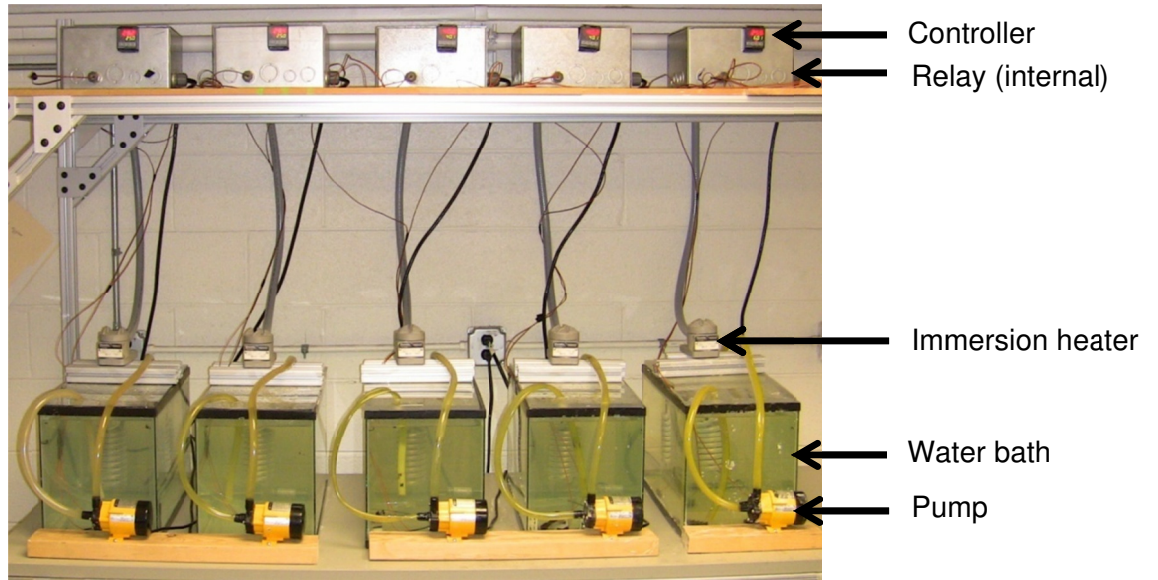


Figure 19: Water baths for hygrothermal aging studies

Weight gains after immersion in water were recorded by periodic removal of the specimens from the environment and weighing on a Mettler AE100 analytical balance with a precision of 0.1 mg. Weight percentage gain (M_t) at any time (t) because of moisture absorption was determined according to Equation 23:

$$M_t(\%) = \frac{W_t - W_d}{W_d} \times 100 \quad (23)$$

where W_d and W_t denote the weight of the specimen prior to exposure to environment and the weight of the exposed specimen, respectively. The equilibrium moisture absorption percentage (M_m) was calculated based as the average of several consecutive measurements that showed negligible additional absorption.

Tensile Test

The study of the effect of hygrothermal aging on tensile properties was carried out on both unreinforced PA12 and carbon fiber reinforced PA12. Specimens were conditioned at 100% relative humidity at 25, 40, 50 and 60°C in the water baths

described previously prior to tensile testing. The tensile test was conducted on an Imada tensile test frame MX-500 with an Imada digital force gauge model Z2H-440. Tensile tests were performed at room temperature (23°C). The present study did not account for the change in mechanical properties resulting from operation at elevated temperatures, which would have required that the properties be measured at the desired operating temperature. Such a test would have made the effects of hygrothermal aging difficult to distinguish from the temperature dependence of the mechanical properties.

Tensile testing was completed within accordance of American Society for Testing and Materials (ASTM) Standard D638 and type V tensile specimens were used [84]. Type V specimens are recommended for applications where the material thickness is 4 mm or less or where a large number of specimens are to be exposed in a limited space (e.g., environmental stability tests). Both of these criteria were satisfied for the present study. The dimensions of the specimens are shown in Figure 20; please note that the gauge length was 7.62 mm and the distance between the grips was 25.4 mm. The displacement rate of 5.8 mm/min was chosen to be as close as possible to the manufacturer-specified displacement rate of 5.1 mm/min, which was used while testing the material properties of the reinforced PA12. The Imada tensile test frame used was incapable of completing tests at a slower displacement rate than 5.8 mm/min.

For these mechanical tests, the resulting strain rate was 0.012/sec, which is normally considered within the quasi-static regime. However, at the strain rate sensitivity of polymer composites, especially with thermoplastic matrices, means that

there can still be potential variability in the measured properties due to differences in the applied strain rate. In order to minimize these effects, efforts were made to ensure consistency in the applied strain rate for every specimen.

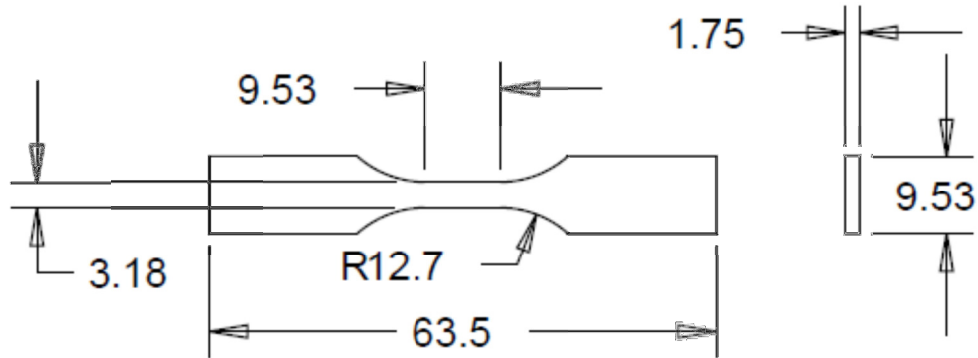


Figure 20: Dimensions of type V tensile specimens (units: mm) [84]

Digital image correlation was used to monitor the strain of the specimens during testing. Two horizontal stripes were marked on each specimen's gauge length (as shown in Figure 21) to allow for visual monitoring of the strain induced on the specimen by Vic-Gauge software. The camera used was Point Grey model FL2-1453M with a Tamron lens.



Figure 21: Dogbone specimen prepared for tensile testing

Results and Discussion

Moisture Absorption

Equilibrium Moisture Content

The equilibrium moisture contents of the raw PA12 and carbon fiber reinforced PA12 are shown in Figure 22. The equilibrium moisture content of both materials does not change significantly with either temperature or salinity. Under all environmental conditions, the equilibrium moisture content for the raw PA12 was

between 1.483% and 1.567% and the equilibrium moisture content for the reinforced PA12 was between 0.539% and 0.586%. Please note that EMS-Grivory published an equilibrium moisture content of 1.5 weight % for their raw PA12 aged at 23°C [64]. PolyOne did not publish an equilibrium moisture content for their carbon fiber reinforced PA12.

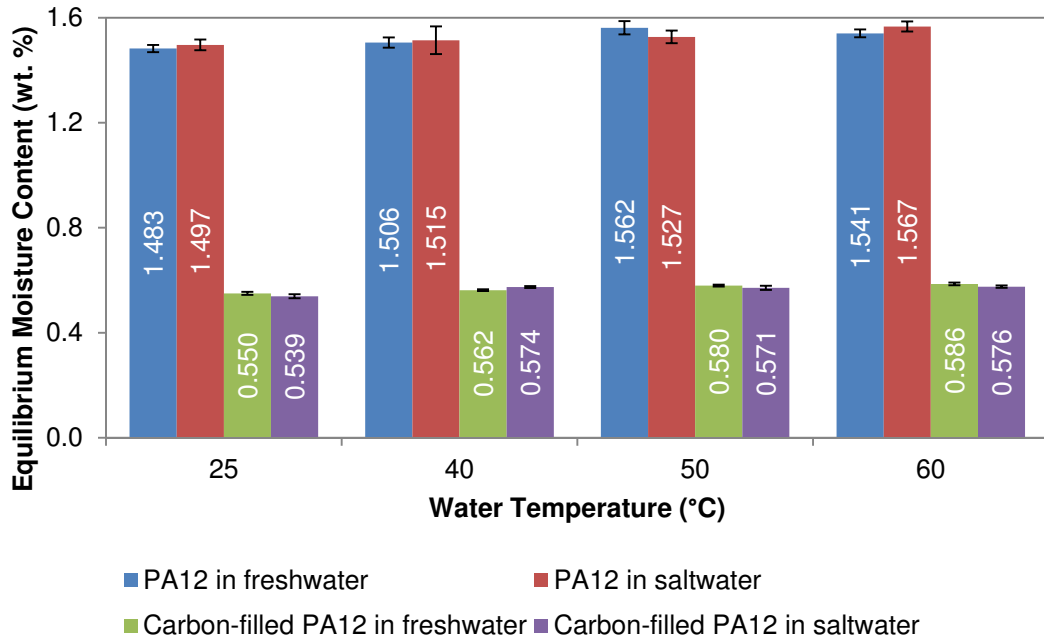


Figure 22: Equilibrium moisture content of raw and reinforced PA12

The theoretical equilibrium moisture content for the reinforced PA12, $(M_m)_c$ was calculated based on the weight fraction of the matrix in the composite, W_m , the equilibrium moisture content of the matrix, $(M_m)_m$, and the understanding that carbon fibers do not absorb any moisture. The corresponding expression for $(M_m)_c$ is shown in Equation 24.

$$(M_m)_c = (M_m)_m \times W_m \quad (24)$$

According to Equation 24, the theoretical equilibrium moisture content of the carbon fiber reinforced PA12 is about 0.73% by weight, which is slightly more than the experimentally determined range of 0.54% to 0.59%. Two simple reasons that may account for the disparity between the theoretical and actual equilibrium moisture contents for fiber reinforced PA12: (1) the carbon may reduce the free volume by tightening the molecular structure between particles and (2) the additives required to functionalize the carbon in the composite mixture could fill the free volume of the composite specimens, reducing equilibrium moisture content. PolyOne does not disclose the additives of its Therma-Tech NJ-6000 TC fiber reinforced PA12.

Since these water absorption experiments (i.e., dilatometry) are often used to characterize the degree of crystallinity, which is related to free volume, in polymers, it is reasonable to assume that one of these mechanisms is in effect. To obtain the degree of crystallinity, it is necessary to have the volume of the crystalline and amorphous matrices. However, that was not possible in this study. Additional characterization techniques include obtaining the change in enthalpy due to crystallinity using Differential Scanning Calorimetry and direct characterization using Wide Angle X-ray Diffraction (WAXD), both of which were beyond the scope of the current study. However, given that their sensitivity to additives may be different than the dilatometry measurements, it is possible that they could be used to distinguish between the two mechanisms.

Ishak and Berry [68] studied hygrothermal aging in carbon fiber reinforced PA66 and also found that in all cases the experimental values of equilibrium moisture content were lower than theoretical values. They argued that the discrepancy might

have resulted from changes in morphology of the PA66 matrix, such as an increase in crystallinity, which they found occurred with the addition of carbon fibers to the PA66 matrix. The research community has accepted that the equilibrium moisture content of polyamides is proportional to their degree of crystallinity through dilatometry testing [67,85]. Thus, their work was consistent with the present findings, but they did not explore the possibility of additive effects on their measurements.

It is noteworthy that in a previous study by Loos and Springer [86] on the moisture absorption of graphite-epoxy composites immersed in liquids, the authors concluded that immersion of specimens in saturated saltwater significantly reduced the equilibrium moisture content of the test specimens. The solubility of sodium chloride (i.e., the primary salt in saltwater) in water is 26.5% by weight [87]. The saltwater used in the present study had a salinity of 4.5 % by weight. At roughly one-eighth the salinity of saturated saltwater, the presence of salt in the water did not significantly affect the equilibrium moisture content of the carbon fiber reinforced PA12 specimens. However, the previous study demonstrates that in applications involving concentrated saline solutions (e.g., desalination), the high salinity of the water may lead to lower equilibrium moisture content levels.

After tensile specimens were hygrothermally-aged and weighed, half of the specimens were redried in accordance with the manufacturer's suggested drying specifications. The weights of the specimens after redrying were compared to the dry weights of the specimens measured before hygrothermal aging. The difference in dry weight prior to and after aging were calculated and normalized according to:

$$\% \text{ difference} = \frac{W_{rd} - W_d}{W_d} \times 100 \quad (25)$$

where W_{rd} is the redried weight and W_d is the dry weight measured prior to aging.

Table 9 shows the average and standard deviation results for the percent difference of the weights of the composite PA12 prior to and post aging. The weight percent differences for the four temperatures and two salinities did not show significant deviation from the baseline weights.

Table 9: Weight % difference between unaged and redried composite PA12

Water Temperature (°C)	Water Salinity (g /kg)			
	0		45	
	Average (wt. %)	Standard Deviation (wt. %)	Average (wt. %)	Standard Deviation (wt. %)
25	-0.0445	0.0141	-0.0434	0.0159
40	-0.0055	0.0172	-0.0100	0.0121
50	0.0013	0.0133	-0.0070	0.0098
60	-0.0306	0.0156	-0.0277	0.0068

Table 10 shows the average and standard deviation results for the percent difference of the weights of the unreinforced PA12. The weight percent differences for the three temperatures and two salinities did not show significant deviation from the baseline weights.

Table 10: Weight % difference between unaged and redried raw PA12

Water Temperature (°C)	Water Salinity (g /kg)			
	0		45	
	Average (wt. %)	Standard Deviation (wt. %)	Average (wt. %)	Standard Deviation (wt. %)
25	-0.0858	0.0543	-0.0509	0.0265
40	-0.0024	0.0408	-0.0042	0.0268
50	0.0388	0.0379	-0.0230	0.0333
60	-0.0522	0.1311	-0.0584	0.0691

Analysis of Variance (ANOVA) [88] was performed on each of the data sets (i.e. for each combination of temperature and salinity and for each material). The results proved that the variation between the weights of the dried, unaged specimens

and the redried specimens was not statistically significant. These results verify that leaching of the fibers (i.e., complete debonding between the fibers and matrix such that the fibers enter the water) did not occur during aging.

Ishai [89] studied environmental effects on the deformation, strength and degradation of glass-fiber reinforced plastics (GRPs). He found that all GRPs (glass fibers comprised 47 vol. % of the composite) exposed to hot water (80°C) were characterized by irrecoverable weight loss and no such behavior was seen in unfilled specimens. Weight loss was attributed to temperature-controlled attack on the glass-fiber surface and the interfacial coupling agent phase by the water, with consequent leaching and removal of glass constituent molecules [89]. The combination of hot water exposure for several days and leaching of glass fibers significantly reduced the tensile strength and increased free volume of the specimens, which allowed for greater moisture absorption during subsequent immersion after redrying [89]. The weight results presented in Table 9 and Table 10 indicate that leaching did not occur with the carbon fiber reinforced PA12 specimens under the conditions of the present study and thus, concerns of strength loss and greater moisture absorption are not applicable to the present study.

Tensile Test

Hygrothermally-Aged Raw PA12

Figure 23 and Figure 24 shows the yield strength and elongation at yield of raw PA12 hygrothermally-aged at several water temperatures and salinities, respectively. Please note that the baseline yield strength was 40.1 MPa and the baseline elongation at yield was 2.95%. Yield strength at all aging conditions was reduced from the baseline value and elongation at yield at all aging conditions

increased relative to the baseline value. Within the uncertainty of the present study, the water temperature and salinity did not have a significant effect on property retention, although yield strength values generally showed lower retention with increasing water temperature.

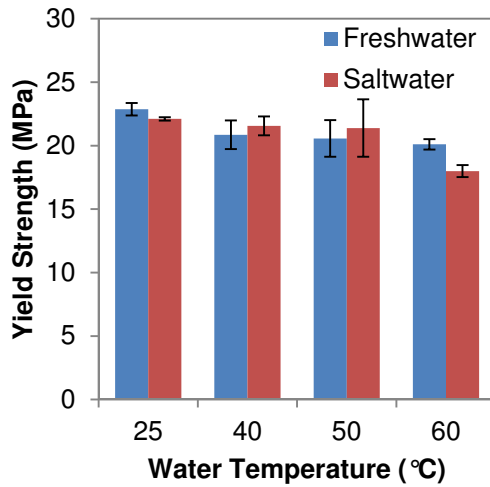


Figure 23: Yield strength of hygrothermally-aged raw PA12

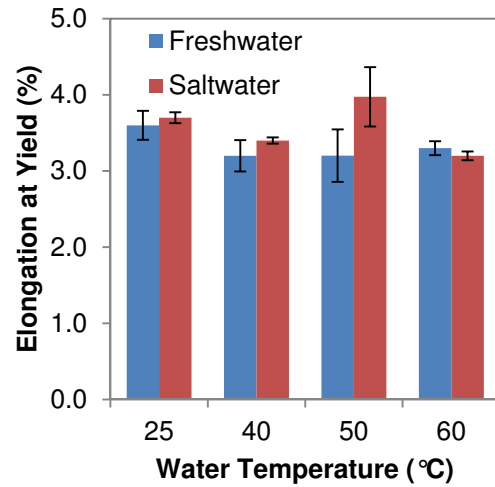


Figure 24: Elongation at yield of hygrothermally-aged raw PA12

Figure 25 shows the longitudinal elastic modulus of raw PA12 hygrothermally-aged at several water temperatures and salinities. Please note that the baseline longitudinal elastic modulus was 1.46 GPa. The trends are similar to those for the yield properties, as the elastic modulus does not appear to be significantly affected by the presence of salt in the water or by water temperature increases.

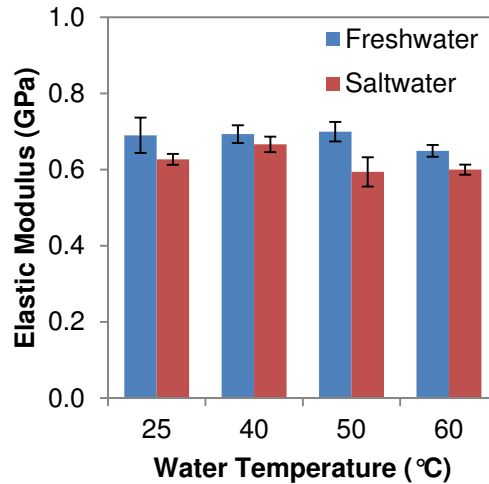


Figure 25: Elastic modulus of hygrothermally-aged raw PA12

Figure 26 shows the failure strength of raw PA12 hygrothermally-aged at several water temperatures and salinities. Please note that the baseline failure strength was 43.8 MPa. The results show unique trends from the others seen in the present study in that the failure strength increases relative to the baseline value at lower water temperatures (i.e., 25 and 40°C) and then decreases relative to the baseline value at higher water temperatures (i.e., 50 and 60°C). This behavior is seen in both freshwater and saltwater and the magnitude at each temperature does not vary significantly with the presence of salt, which indicates that salt does not have a significant effect on the failure strength of unreinforced PA12 for the conditions of the present study. The increase in ultimate strength of the aged raw PA12 at the lower condition temperatures may be the result of the moisture allowing the polymer chains to slip past each other more readily, which prolongs time before fracture.

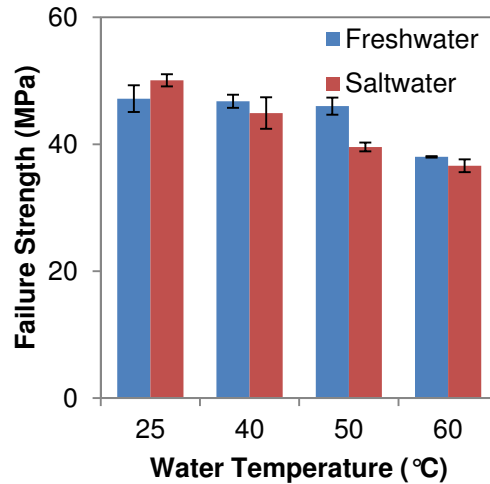


Figure 26: Failure strength of hygrothermally-aged raw PA12

Hygrothermally-Aged Composite PA12

Figure 27 and Figure 28 shows the yield strength and elongation at yield of composite PA12 hygrothermally-aged at several water temperatures and salinities, respectively. Please note that the baseline yield strength was 91.5 MPa and the baseline elongation at yield was 0.71. Yield strength at all aging conditions was reduced from the baseline value and elongation at yield at all aging conditions increased relative to the baseline value. Within the uncertainty of the present study, saltwater did not appear to affect the polymer composite differently than the freshwater did. The higher temperatures appear to increase the effect of hygrothermal aging, as indicated by yield strength retention of 85% at 25°C and only 66% at 60°C. Similar behavior is seen in the elongation at yield, with an 8% increase at 25°C relative to the baseline value and a 24% increase at 60°C relative to the baseline value.

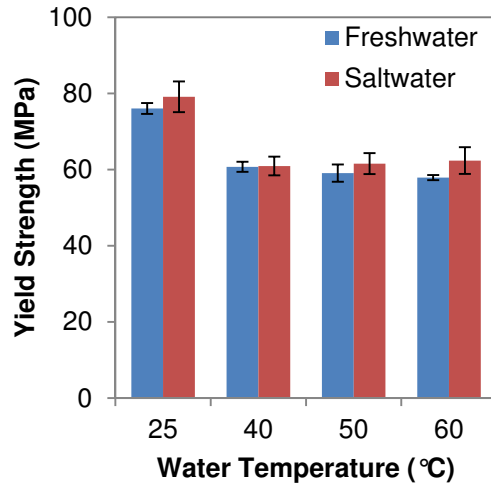


Figure 27: Yield strength of hydrothermally-aged composite PA12

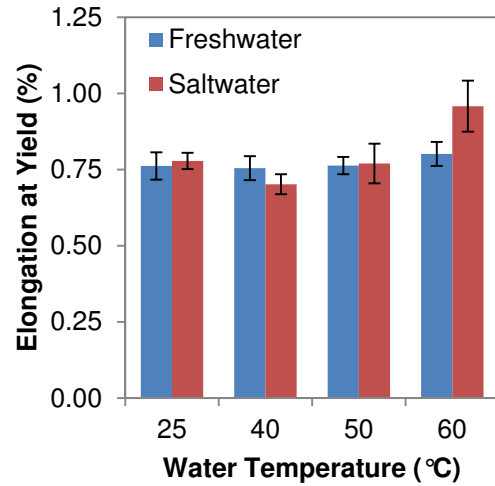


Figure 28: Elongation at yield of hydrothermally-aged composite PA12

Figure 29 shows the longitudinal elastic modulus of composite PA12 hydrothermally-aged at several water temperatures and salinities. Please note that the baseline longitudinal elastic modulus was 18.5 GPa. The trends are similar to those for the yield properties, as the elastic modulus does not appear to be significantly affected by the presence of salt in the water and property retention decreases with increasing water temperature. At a water temperature of 25°C, the elastic modulus retains 75% of its baseline value and at a water temperature of 60°C, the elastic modulus retains only 50% of its baseline value.

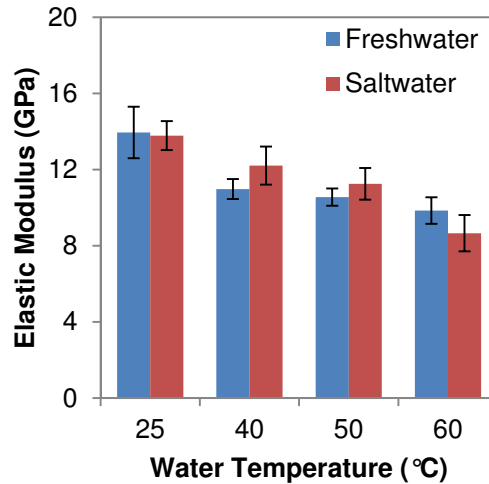


Figure 29: Elastic modulus of hygrothermally-aged composite PA12

Figure 30 and Figure 31 shows the failure strength and elongation at failure of composite PA12 hygrothermally-aged at several water temperatures and salinities. Please note that the baseline failure strength was 105.0 MPa and the baseline elongation at failure was 1.38%. Similar to the behavior seen in the yield properties of the aged composite, failure strength decreased and elongation at failure increased for all aging conditions. The presence of salt did not appear to have a significant effect on the failure properties of composite PA12. The effect of hygrothermal aging appears to be more significant at higher temperatures, with 90% retention of failure strength at 25°C and only an average of 82% retention at 40-60°C and only a 29% increase in elongation at failure at 25°C but an average increase of 114% at temperatures 40-60°C.

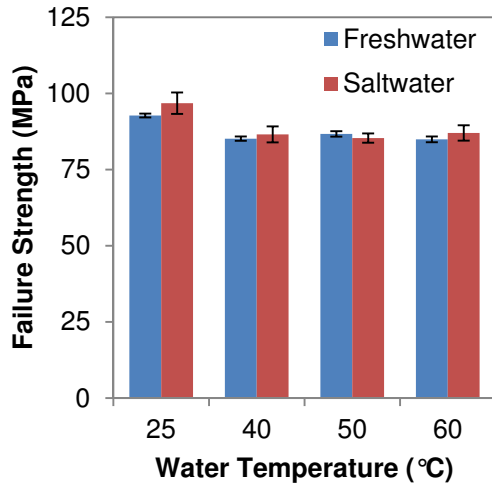


Figure 30: Failure strength of hydrothermally-aged composite PA12

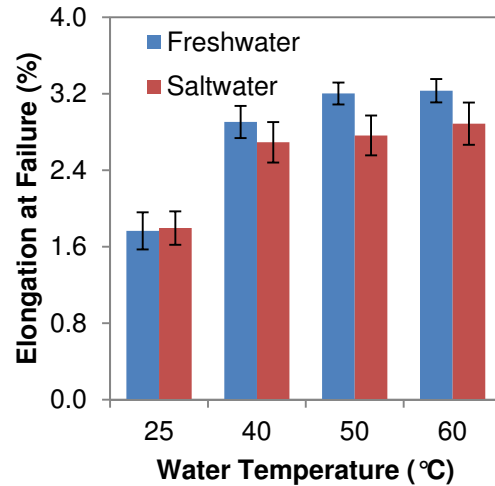


Figure 31: Elongation at failure of hydrothermally-aged composite PA12

Redried Raw PA12

Figure 32 and Figure 33 shows the yield strength and elongation at yield of raw PA12 after redrying, respectively. Please note that the baseline yield strength was 40.1 MPa and the baseline elongation at yield was 2.95%. The yield strength of raw PA12 after redrying is nearly completely recovered with the lowest recovery of 92%, which occurred in specimens that were redried after aging at 60°C. The elongation at yield results show a nonuniform trend that may be the result of the relatively large uncertainty in the results. Despite the large uncertainty, the results show good recovery of baseline properties, with the maximum disparity of 20% greater elongation at yield relative to baseline results occurring in specimens aged at 50°C.

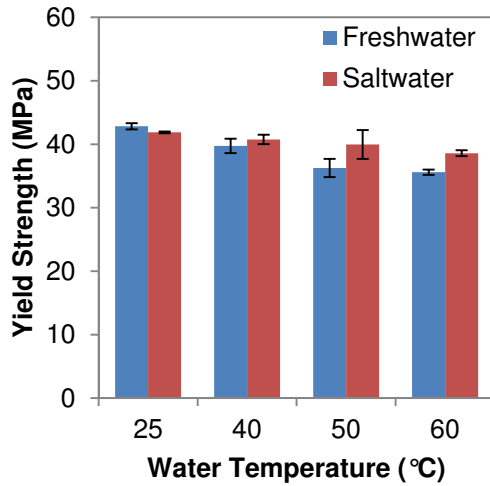


Figure 32: Yield strength of redried raw PA12

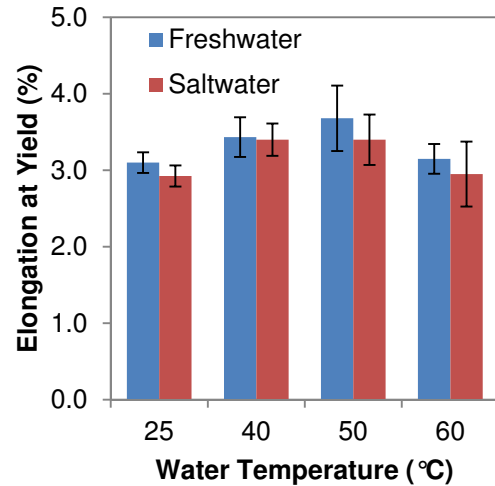


Figure 33: Elongation at yield of redried raw PA12

Figure 34 shows the longitudinal elastic modulus of raw PA12 after redrying. Please note that the baseline longitudinal elastic modulus was 1.46 GPa. The trends are similar to those for the yield properties, with general good recovery of baseline properties regardless of aging temperature or salinity. The maximum disparity from baseline results occurred in the specimens redried after aging at 50°C, which showed a 17% reduction in elastic modulus after redrying. Among all aging conditions, the average recovery of elastic modulus was 90%.

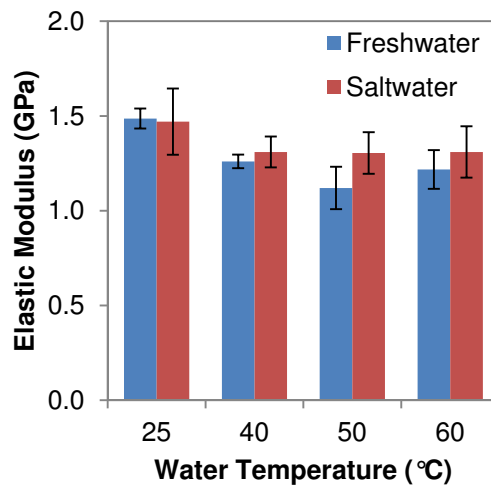


Figure 34: Elastic modulus of redried raw PA12

Figure 35 shows the failure strength of raw PA12 after redrying. Please note that the baseline failure strength was 43.8 MPa. The results in general show excellent recovery of baseline properties and improvements relative to baseline properties in some cases. However, it is not expected that redrying after aging results in improved failure strength.

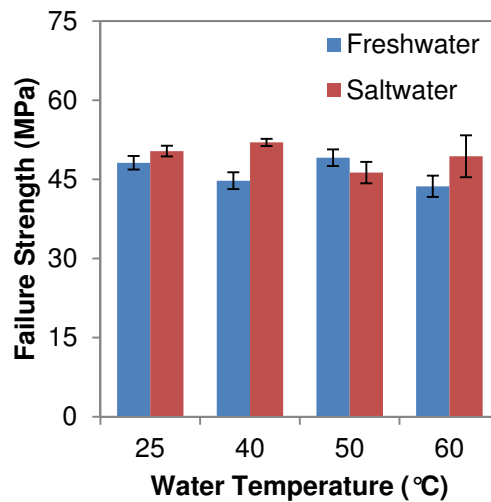


Figure 35: Failure strength of redried raw PA12

Redried Composite PA12

Figure 36 and Figure 37 shows the yield strength and elongation at yield of composite PA12 after redrying. Please note that the baseline yield strength was 91.5 MPa and the baseline elongation at yield was 0.71. Among all temperature and salinity conditions, the yield strength and elongation at yield of redried composite PA12 show excellent recovery of baseline properties, although recovery at higher temperatures is slightly less than at lower temperatures. At water temperatures of 50 and 60°C, recovery of yield strength was 92% of the baseline value and the elongation at yield results showed only a 1% increase relative to the baseline value.

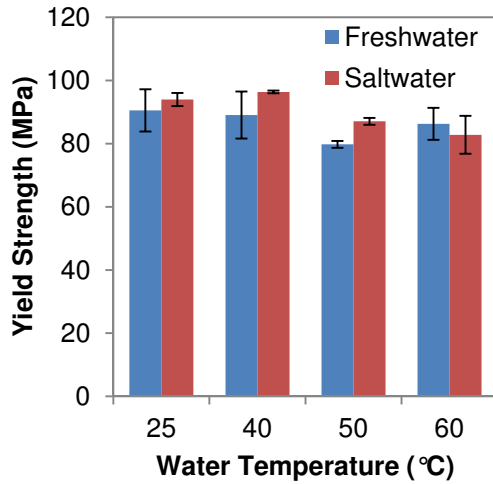


Figure 36: Yield strength of redried composite PA12

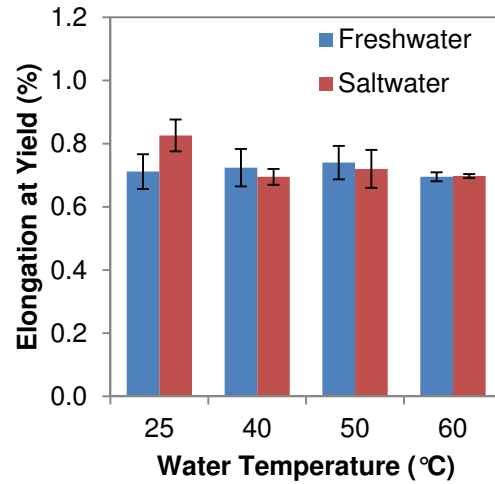


Figure 37: Elongation at yield of redried composite PA12

Figure 38 shows the longitudinal elastic modulus of composite PA12 hydrothermally-aged at several water temperatures and salinities. Please note that the baseline longitudinal elastic modulus was 18.5 GPa. The trends revealed that the elastic modulus of redried composite PA12 is not significantly affected by the presence of water and that recovery was slightly less as temperature increased (i.e., the lowest recovery of 89% of the baseline value occurred at a water temperature of 60°C).

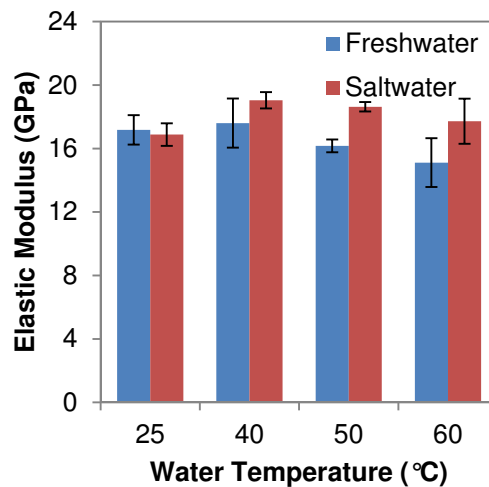


Figure 38: Elastic modulus of redried composite PA12

Figure 39 and Figure 40 shows the failure strength and elongation at failure of composite PA12 hygrothermally-aged at several water temperatures and salinities. Please note that the baseline failure strength was 105.0 MPa and the baseline elongation at failure was 1.38%. Similar to the trends seen in the elastic modulus, redried composite PA12 showed excellent recovery of properties although property recovery was slightly less at higher temperatures. Nonetheless, for samples aged at 60°C and then redried, the failure strength was recovered to 92% of its baseline value and elongation at failure increased by only 2% relative to its baseline value.

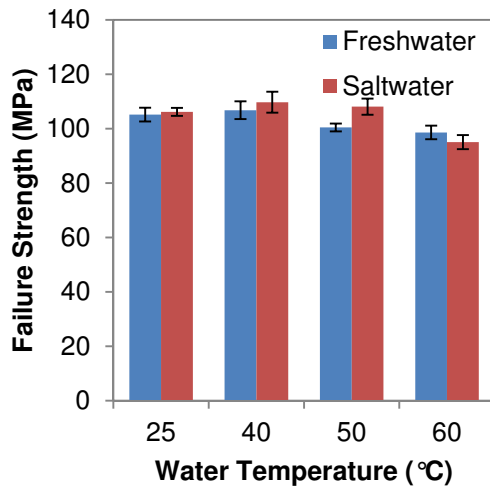


Figure 39: Failure strength of redried composite PA12

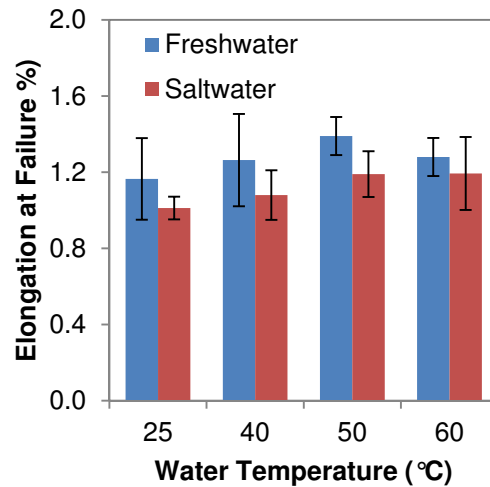


Figure 40: Elongation at failure of redried composite PA12

Trends in Property Change of Raw and Reinforced PA12

A summary of the change in mechanical properties resulting from the addition of carbon fibers to the PA12 matrix, hygrothermal aging and redrying after hygrothermal aging can be seen in Figure 41. Please note that the stress-strain curves of the raw PA12 have been truncated for clarity. The addition of the carbon fibers led to a dramatic shift in material behavior from ductile to brittle with a dramatic increase

in stiffness and strength and reduction in ductility. Hygrothermal aging at 60°C reduced stiffness and strength and increased ductility in both materials, although the effect was more pronounced in raw PA12. Both raw and reinforced PA12 experienced excellent recovery of mechanical properties after redrying.

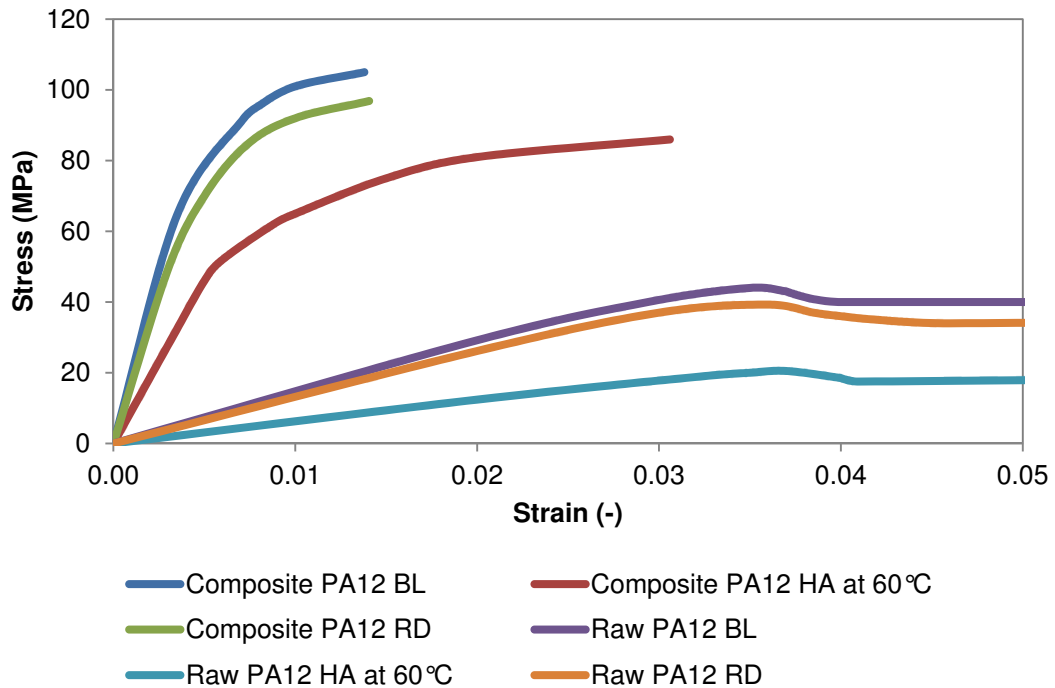


Figure 41: Stress-strain behavior of raw and reinforced PA12

Discussion of Tensile Test Results

The excellent recovery of stress-strain behavior after redrying indicates that the primary mechanism of hygrothermal aging in unreinforced PA12 and fiber reinforced PA12 may be increased plasticization due to the reversible disruption of secondary bonds (van der Waals forces) between the polymer molecules due to the ionization in the water or dilatational effects. This results in a decrease in the degree of crystallinity, and a decrease in the associated glass transition temperature, stiffness, and strength of the polymer matrix. The physical nature of plasticization is indicated by the almost complete recovery of stress-strain properties upon removal of the

moisture. One way that this can be confirmed would be to use deionized water, but that was beyond the scope of the current study.

It appears from the aged raw PA12 results that there is only an effect from the moisture on the degradation of mechanical properties, which was most likely due to short-range reconfiguration of the molecular structure and reduction of Van der Waal's forces that reduced material strength 50% and increases flexibility 100%. However, there was not a substantial change in the ultimate strength and elongation at failure, which are more dependent on the long-range characteristics of the polymer. In the reinforced PA12, there is an additional effect of temperature, which is likely due to decohesion at the fiber-matrix interface that increased flexibility 50% and decreased strength 30%, while increasing elongation at failure by 100%. However, in general the fibers nonetheless substantially improve the stiffness and strength of the aged polymer at the expense of ductility.

It is noteworthy that there is some variation in mechanical properties after redrying and there is a trend of reduced recovery at the higher conditioning temperatures of 50 and 60°C. In the unreinforced polymer, the higher conditioning temperature may have resulted in some hydrolysis of the polymer bonds, which would result in a permanent change in mechanical properties. If hydrolysis is at fault for the slight reduction in properties after redrying, it appears that PA12 is susceptible to hydrolysis only at elevated temperatures for the duration of the present study.

In the reinforced PA12 material system, hydrolysis could have also affected the strength of the raw polymer. In addition, the action of the water may have resulted in the partial disruption of bonds between the fiber and matrix (i.e., debonding) and

the formation of microcavities that filled with water during aging. Upon redrying, microcavities previously filled with water would have served as stress concentrators that could have initiated matrix cracking, which would have reduced composite stiffness and strength [68]. If these damage mechanisms (i.e., hydrolysis, debonding and microcavity formation) were present, they appear to have affected the mechanical properties of the composite only at the higher conditioning temperatures and their effect on property recovery was modest. It is possible that their effect could increase with time an increasing temperature and thus, designers must test their material systems under the appropriate conditions for a sufficient duration to ensure the effects of these damage mechanisms do not reduce system performance or safety over time.

Summary of Findings

Raw and carbon fiber reinforced PA12 specimens were exposed to various water conditions until saturation was achieved. The equilibrium moisture content of raw polymer samples was between 1.483 and 1.567 weight % and the equilibrium moisture content of fiber reinforced polymer samples was between 0.539 and 0.586 weight %. The difference in moisture absorption was attributed to the presence of the fibers, which do not absorb moisture, and other changes resulting from the addition of the fibers, such as reducing the free volume through increases in crystallinity of the polymer matrix or through the presence of additives that promote adhesion of the fibers to the polymer matrix. In samples of both materials, salinity did not affect equilibrium moisture content and there was a general trend of slightly increasing equilibrium moisture content with increasing water temperature.

The tensile properties of raw and carbon fiber reinforced PA12 specimens were studied prior to aging, after aging and after redrying after aging. The addition of the carbon fibers to the PA12 matrix dramatically increased the stiffness and strength of the material system while changing the material behavior from ductile to brittle. The raw and carbon fiber reinforced PA12 materials experienced reductions in elastic modulus, yield strength and failure strength, and increased ductility after hygrothermal aging, although the fiber reinforced PA12 had greater retention of properties. The effects of hygrothermal aging were more significant at higher temperatures but the presence of salt in the water did not appear to change the material behavior significantly. The specimens of both materials that were redried after hygrothermal aging exhibited excellent recovery of their baseline properties, which indicates that the primary mechanism by which hygrothermal aging occurs in these materials is physical.

Chapter 5: Mechanical Modeling

Motivation

A finite element model of a laboratory scale prototype polymer composite heat exchanger was developed to assess the structural performance of the anisotropic composite material described in Chapter 3. The model was implemented to determine the effects of orthotropic reinforcement of the polymer resulting from the addition of carbon fibers to the polymer matrix and the injection molding process. The model allowed for a comparison of stress-strain behavior among the polymer composite and conventional materials implemented in corrosion-resistant heat exchange applications and served as a baseline for later combined thermomechanical modeling.

Operating Conditions

The Abu Dhabi Gas company, a subsidiary of the Abu Dhabi National Oil Company, processes and distributes natural gas in the United Arab Emirates. Seawater is one coolant used in the liquefaction of natural gas. Heat exchangers located in the third train of the Das Island liquefied natural gas facility (see Figure 42) were the focus of the present analysis. The heat exchangers cool various gases (e.g., steam, propane, hydrocarbon vapor, etc.) using seawater. The inlet pressures of the gases and the seawater for various heat exchangers in the third LNG train are shown in Figure 43. The pressure of the gas ranges from near atmospheric to 5.87 MPa and the pressure of the seawater is generally around 0.40 MPa. Based on this information, finite element models were conducted using boundary conditions corresponding to a seawater pressure of 0.50 MPa and gas side pressures of 0.50 MPa and 5.0 MPa to

assess the structural performance of polymer composite heat exchangers over a range of possible operating conditions.



Figure 42: Das Island seawater intake and outlet [90]

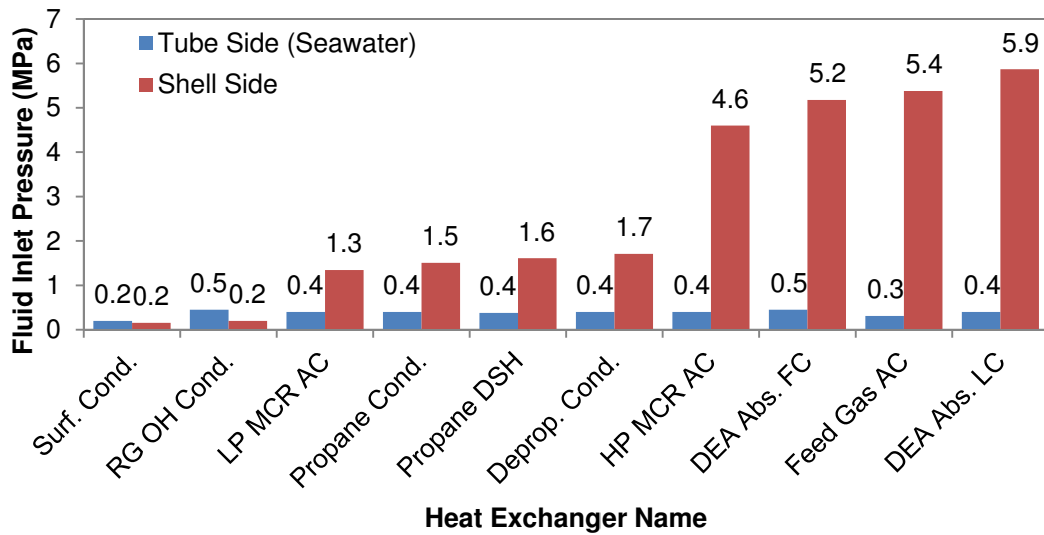


Figure 43: Fluid inlet pressures for heat exchangers in Das Island third LNG train [91]

Finite Element Model

Finite element modeling was employed to assess the stress distributions that develop in isotropic and anisotropic heat exchanger modules when they are subjected to pressure loading from their working fluids. The desktop computer utilized for the numerical simulations was a Dell Optiplex 960 with an Intel Q9550 quad-core

processor operating at 2.83 GHz with 8.0 gigabytes of random access memory and 320 gigabytes of hard disk storage. The finite element software employed for the studies was Mechanical ANSYS Parametric Design Language (APDL) version 12.1, which is referred to as ANSYS throughout the remainder of the document.

Brick elements were selected rather than tetrahedral elements because brick elements enable the use of mapped meshing, whereas tetrahedral elements require the use of free meshing in commercial finite element software ANSYS. Mapped meshing offers several advantages over free meshing [92], which include that brick meshing is a highly controllable meshing process, produces very repeatable results, allows for easier convergence checking and can be optimized to maximize accuracy while minimizing computation time.

The brick element used through the present analysis was SOLID226, a three-dimensional 20-node coupled field solid shown in Figure 44. Each of the 20 nodes can have up to five degrees of freedom, which are x-displacement, y-displacement, z-displacement, temperature and voltage. For the present analysis, either structural or structural-thermal studies were completed and thus, the degrees of freedom were limited to displacement and temperature.

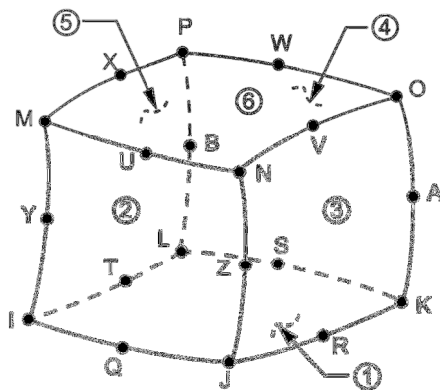
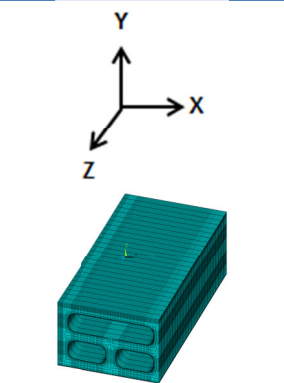


Figure 44: SOLID226 brick element [93]

Based on the use of transversely isotropic materials, the required material property inputs were elastic moduli, Poisson’s ratios, shear moduli, thermal conductivities and coefficients of thermal expansion. Additional material properties (e.g., specific heat capacity) were not required because all analyses were completed at steady state. The mechanical properties input into the mechanical model are provided in Table 11.

Table 11: Mechanical properties input into finite element model

Property	Plate	Fin
E_x (GPa)	18.46	3.18
E_y (GPa)	3.18	18.46
E_z (GPa)	3.18	3.18
ν_{xy} (-)	0.339	0.058
ν_{yz} (-)	0.513	0.339
ν_{xz} (-)	0.339	0.513
G_{xy} (GPa)	1.01	1.01
G_{yz} (GPa)	1.05	1.01
G_{xz} (GPa)	1.01	1.05



Prototype Heat Exchanger

Using the reinforced PA12 described previously, finned plates were injection-molded and assembled into a crossflow configuration. Due to manufacturing constraints, the laboratory heat exchanger was limited in size to a cube approximately 5 cm on a side. A picture of the assembled heat exchanger is shown in Figure 45, where three air channels and three water channels can be seen. The air channels can be distinguished by the presence of rectangular fins, which were added to compensate for the low airside heat transfer coefficient. These fins were not required on the waterside because of the high heat transfer coefficient provided by the flow of water.



Figure 45: Isometric view of prototype heat exchanger [34]

An isometric view and the dimensions of the prototype heat exchanger are shown in Figure 46. Note that the plate, wall, fin thickness of 2.5 mm was kept constant throughout the exchanger to adhere to established injection-molding guidelines.

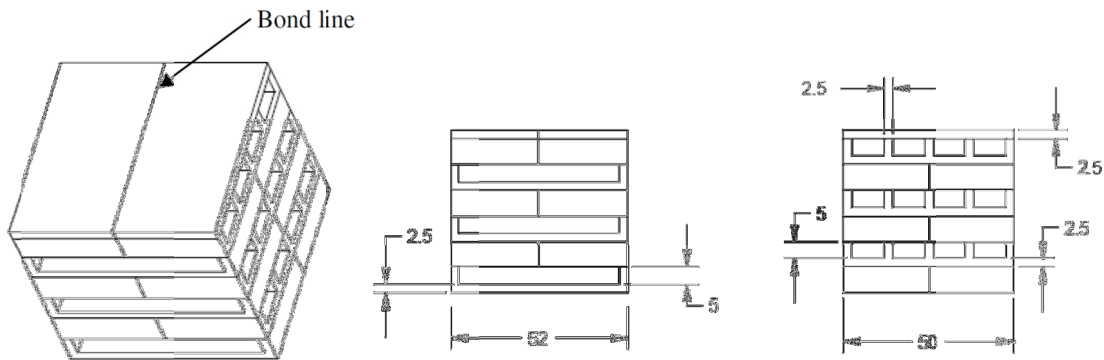


Figure 46: Heat exchanger dimensions (units: mm) [34]

Initial structural modeling revealed that an additional waterside fin – although not required for thermal purposes due to the high heat transfer coefficient ($\sim 1000 \text{ W/m}^2\cdot\text{K}$) – was required to reduce the stress magnitudes resulting from the application of the waterside pressure load. The inclusion of the additional fin was maintained during thermal and thermomechanical modeling for consistency and its effect on the heat transfer rate was considered negligible.

Mesh Independence Study

Mesh Parameters

A mesh independence study was performed to validate the numerical modeling results for structural loading of polymer composite heat exchangers. The heat exchanger geometry was identical to the geometry described previously with the exception of the length in the fluid axial direction (z-direction), which was shortened from 50 mm to 5 mm to reduce computation time. The x-direction is along the width of the heat exchanger and the y-direction is along the height of the heat exchanger. The mesh parameters that were varied were the number of divisions in the x-y plane (see Figure 47), the spacing ratio in the x-y plane (see Figure 48), the element size in the x-y plane (see Figure 49) and the element size in the z-plane (see Figure 50). Please note that the mesh independence study was completed for structural loading only because structural stress concentrations are often points of failure and, at the anticipated operating temperatures, there was no comparable thermal failure point in the heat exchanger.

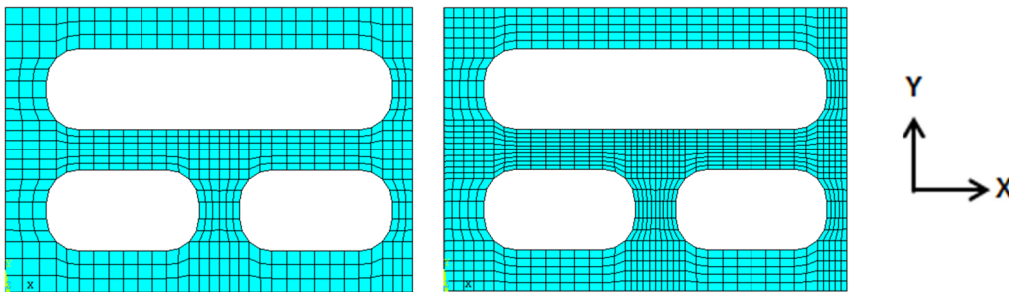


Figure 47: Variation of number of divisions parameter (left: 3, right: 5)

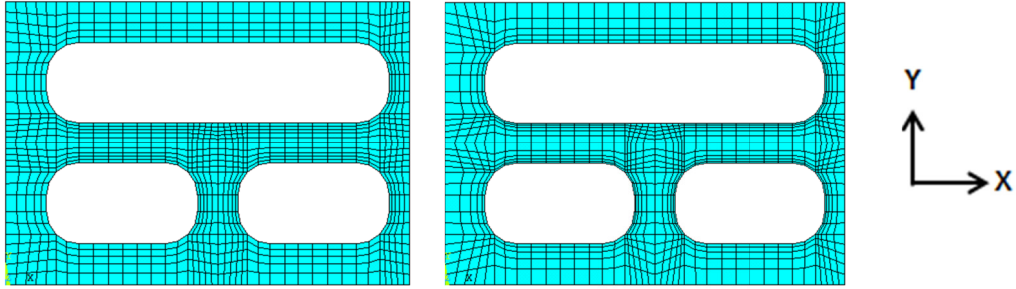


Figure 48: Variation of spacing ratio parameter (left: 2, right: 5)

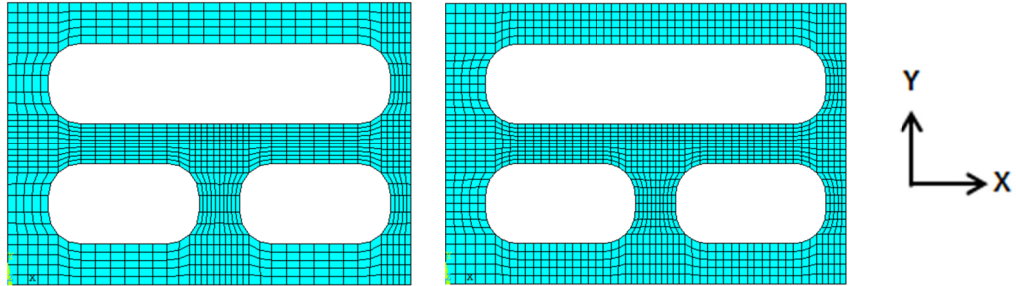


Figure 49: Variation of x-y element size parameter (left: 0.50 mm, right: 0.25 mm)

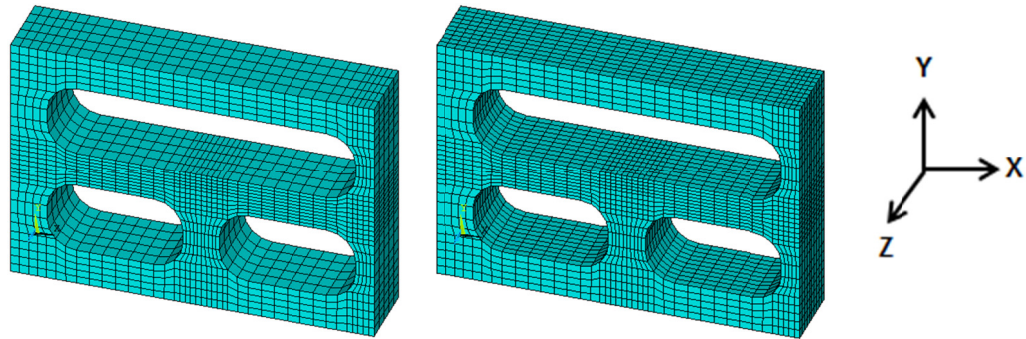


Figure 50: Variation of z element size parameter (left: 1.0 mm, right: 0.5 mm)

The mesh parameters were each varied from a low value to a middle value to a high value, as indicated in Table 12. The values shown represent a suitable range of values for the current geometry given the applied loads and constraints (this assumption was validated by the results that are provided later in this section).

Table 12: Mesh parameters and their values

Parameter	Number of divisions in x-y plane	Spacing ratio in x-y plane	Element size in x-y plane	Element size in z-plane
Low value	5	2	1.00	1.00
Middle value	10	10	0.50	0.50
High value	20	20	0.10	0.25

Modeling Results

Based on the mesh parameters listed in Table 12, 81 simulations were required but computational limitations reduced the number of simulations to 74. The results of the remaining 74 simulations are shown in Figure 51 (x-direction), Figure 52 (y-direction), Figure 53 (z-direction) and Figure 54 (y-z-direction). The y-z- and x-z-direction stresses are not shown because in all simulations, the stress magnitudes in these directions were modest (i.e., 2.0-2.9 MPa) and showed little variation with element count. Although some scatter is evident in each figure due to the nature of the mesh refinement study (i.e., the plots show the variation of multiple mesh parameters simultaneously), the results indicate that the maximum x- and y-direction stress increase with increasing element count, the maximum x-y-direction stress decreases with increasing element count and the z-direction stress magnitude shows opposing trends. Accordingly, it was concluded that the most accurate x- and y-direction stresses were the largest values obtained and the most accurate x-y-direction stresses were the smallest values obtained. The z-direction stress magnitude was not included in the mesh independence study because of the opposing trends seen with increasing element count. Thus, the accepted x-, y- and x-y-direction stress magnitudes were 50.7, 78.6 and 14.6 MPa, respectively.

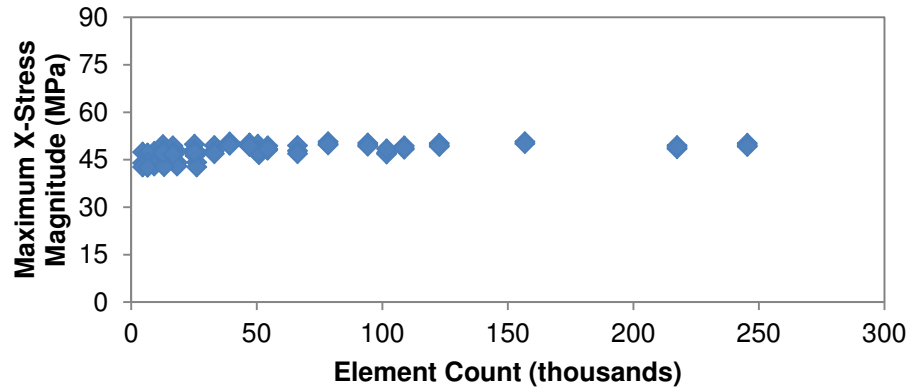


Figure 51: Mesh independence study for x-direction stress magnitude

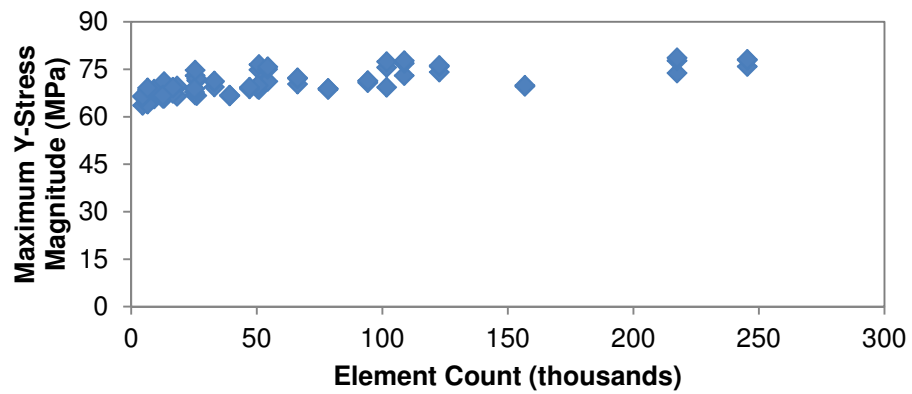


Figure 52: Mesh independence study for y-direction stress magnitude

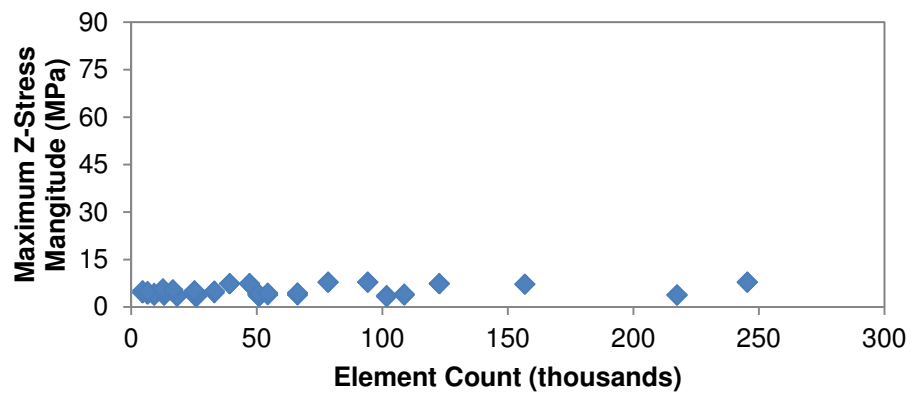


Figure 53: Mesh independence study for z-direction stress magnitude

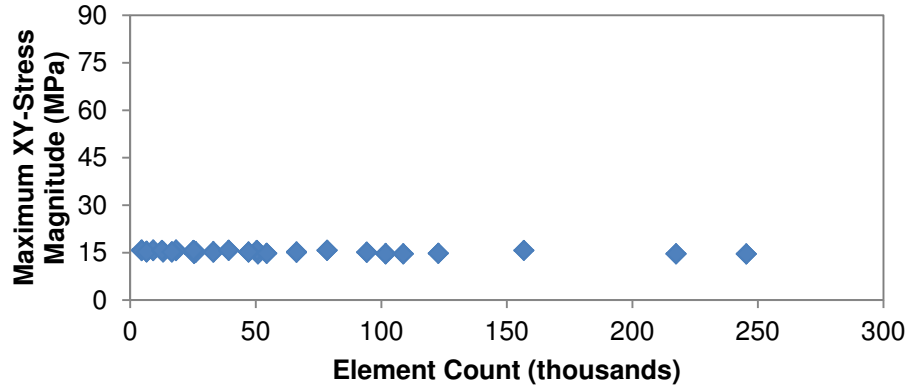


Figure 54: Mesh independence study for y-z-direction stress magnitude

The performance of the model as a function of the mesh parameters described previously was measured using the square root of the sum of the error (\sqrt{SE}):

$$\sqrt{SE} = \sqrt{(S_x - 50.7 \text{ MPa})^2 + (S_y - 78.6 \text{ MPa})^2 + (S_{xy} - 14.6 \text{ MPa})^2} \quad (26)$$

where S_x , S_y and S_{xy} are the magnitudes of the maximum stresses in the x-, y- and x-y-directions, respectively. The maximum allowable error was set to 5% in each of the three stress magnitudes, which resulted in a maximum allowable \sqrt{SE} of 4.8 that was achieved in 15 of the mesh configurations. Although 15 mesh configurations achieved less than the maximum allowable error, the computation time among the mesh configurations varied widely, as shown in Figure 55.

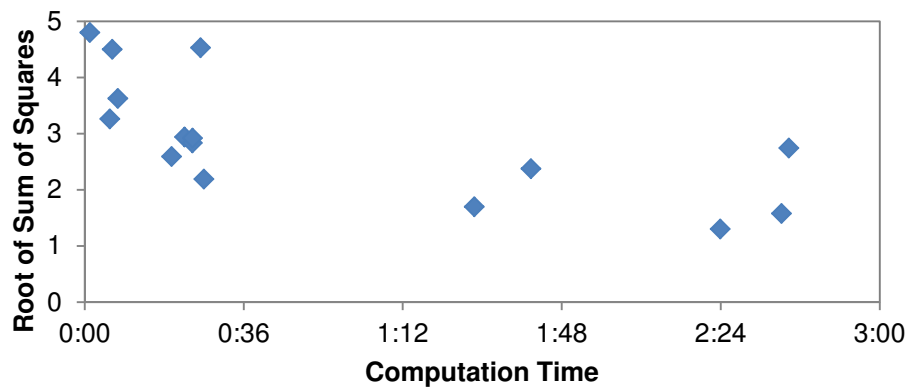


Figure 55: Error in stress magnitude as a function of computation time

Parameter Selection

The mesh configuration with the minimum runtime of 68 seconds had five divisions in the x-y plane, a spacing ratio of 20 in the x-y plane, 0.1 mm element size in the x-y plane and 1.0 mm element size in the z-plane, as shown in Figure 56.

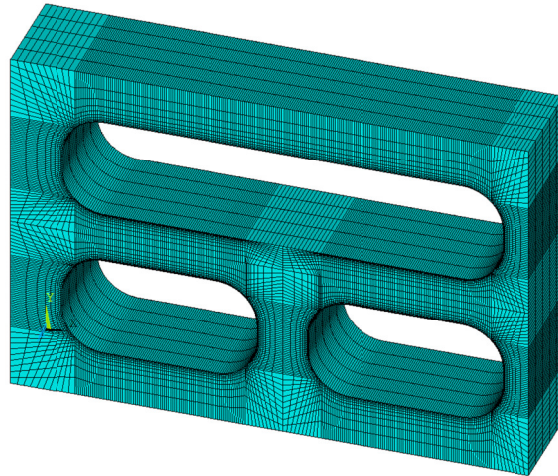


Figure 56: High accuracy, low runtime mesh configuration

Although the mesh configuration described previously met allowable error constraints, it was found that the mesh was not appropriately refined to allow for the most accurate determination of the maximum x-magnitude direction. Please note that the location of the maximum x-stress location, which is denoted ‘MX’ in Figure 57, does not correspond to an area where the mesh is sufficiently refined to capture the stress magnitude in the region. The locations of other maximum stress magnitudes corresponded with areas of mesh refinement and thus additional refinement for other directions was unnecessary.

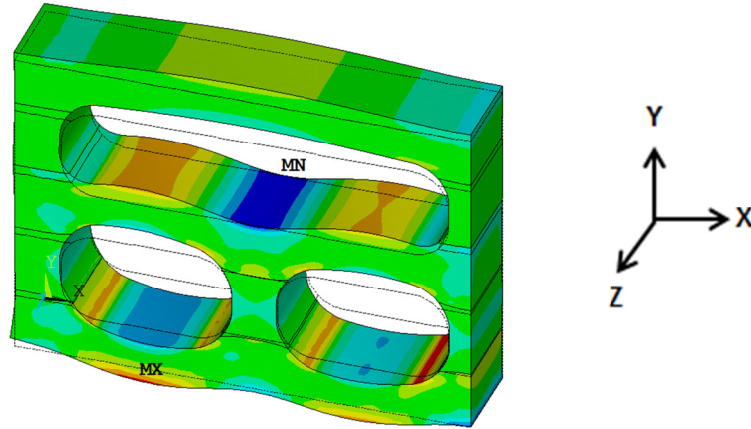


Figure 57: X-direction stress contours

Additional Refinement

A change in the volume meshing procedure was made to ensure that the mesh was refined in the location of the maximum x-direction stress magnitude, as shown in Figure 58. The volume count was increased from 53 to 80 to allow for enhanced refinement capability and the new volumes are highlighted in blue. Using the same mesh parameters selected above that offered a balance of accuracy and computation time, the additional volumes reduced the \sqrt{SE} from 4.80 to 3.91. Although the additional volumes allowed for greater refinement and improved accuracy, their inclusion increased element and runtime and thus, the mesh parameters were evaluated again to maintain accuracy while minimizing computation time.

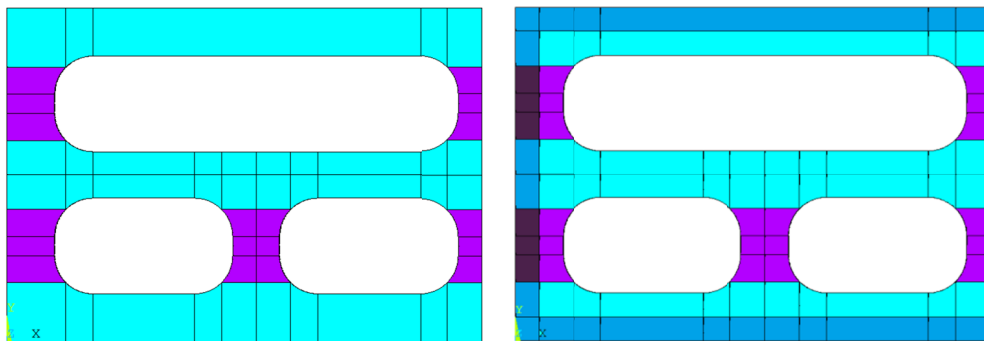


Figure 58: Original (left) and refined (right) volume assignments

Each of the mesh parameters were varied sequentially to achieve the goal of maintaining result accuracy to within the threshold value described previously while minimizing computation time. The sequence of adjustment was element size in the x-y plane, element size in the z-plane, number of divisions in the x-y plane and spacing ratio in the x-y plane. Variation of these parameters revealed that the element size in the x-y plane could be increased from 0.1 mm to 0.2 mm, element size in the z-plane could be increased from 1.0 mm to 2.0 mm and the spacing ratio could be decreased from 20 to 15. These changes reduced the element count more than 77% from 507,400 to 114,700, while increasing the \sqrt{SE} value slightly from 3.91 to 4.10, which was still below the threshold limit of 4.80. Please note that the element count decrease noted was for the full-length heat exchanger model (50 mm), not the heat exchanger model used for refinement that was only 5 mm in length. Figure 59 shows the final, refined mesh on the full-length heat exchanger model.

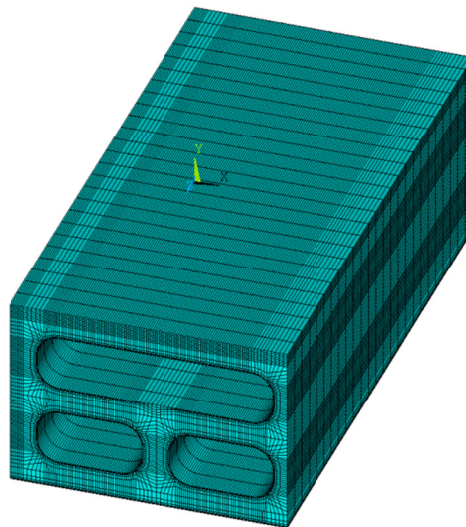


Figure 59: Refined brick mesh on heat exchanger

Model Verification

A model verification process was completed to ensure that the stress magnitudes calculated by the finite element model agreed with established mechanics

of materials understanding. The verification process was achieved in an isotropic titanium heat exchanger exposed to an applied airside pressure of 1.0, 3.0 and 5.0 MPa and no waterside pressure. Linearly elastic isotropic materials exposed to such loads should experience maximum stress magnitudes that increase proportionately to the applied pressure. The maximum stress magnitudes experienced by the titanium HX as a function of airside pressure are shown in Table 13. The results reveal that the model predicts the maximum stress magnitudes as expected, with the maximum directional stresses increasing proportionately to the applied airside pressure.

Table 13: Maximum stresses in isotropic HX as a function of airside pressure

Airside Pressure (MPa)	X Stress (MPa)	Y Stress (MPa)	XY Stress (MPa)
1.0	5.5	6.8	3.9
3.0	16.5	20.4	11.8
5.0	27.5	33.9	19.7
Stress ratio between 1.0 MPa and 3.0 MPa	3.00	3.00	2.99
Stress ratio between 1.0 MPa and 5.0 MPa	5.00	4.99	5.00

An additional test that serves to verify the modeling results is to study the normal stress that develops at the surface exposed to the pressure load because the stress at the surface should equal the pressure at this surface. The directional stress contours were plotted on the HX geometry to study the normal stress that developed at the surface exposed to the pressure load. The results revealed that – as one would expect – the normal stress at these surfaces was equal to the applied pressure. Figure 60 shows the y-direction stress magnitudes in an airside channel of an isotropic heat exchanger exposed to an airside pressure of 1.0 MPa. The results reveal that at the top and bottom of the channel where the y-direction stress represents the normal stress, the stress at the wall is compressive in nature and equal in magnitude to the pressure.

Results for other pressures and the x-direction stress magnitude are consistent with the results shown in Figure 60.

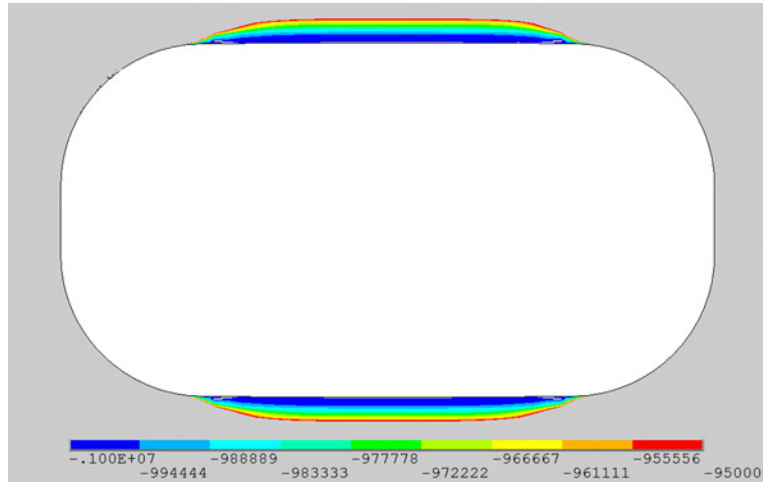


Figure 60: Y-direction stress magnitudes in an airside channel of an isotropic heat exchanger exposed to an airside pressure of 1.0 MPa (Units: Pa)

Results and Discussion

Comparison of Corrosion-Resistant Materials

Maximum Stress Magnitudes

Structural analysis of composite PA12 and common corrosion resistant heat exchanger materials was completed using an airside pressure of 5000 kPa and waterside pressure of 500 kPa. These stress magnitudes represent the near maximum stresses seen in the third LNG train at the Das Island LNG processing facility. The stress distributions that developed in composite PA12 were compared to those that developed in PTFE ($E=0.60$ GPa, $\nu=0.46$) and Titanium Grade 2 ($E=105$ GPa, $\nu=0.37$). The maximum stresses that developed in each material are shown in Figure 61. Please note that the yz- and xz-stresses are not shown because they are negligible for the current loading conditions.

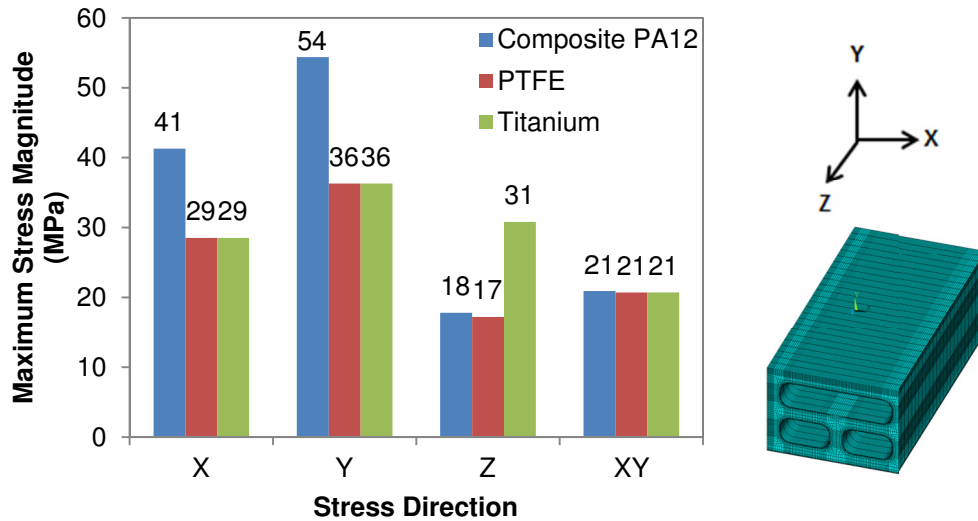


Figure 61: Maximum stress development in heat exchangers fabricated from various materials subjected to mechanical loading

The results in Figure 61 show that stress development in linearly elastic, isotropic materials is a function of geometry only in the absence of boundary conditions, as shown by identical x-, y- and xy-stresses for PTFE and titanium. This is consistent with analytical models for pressure vessels. The z-direction stresses differ due to the imposed constraint from the boundary condition in this direction, which leads to a plane strain condition. In the PCHX, higher stresses develop in those direction that are reinforced by aligned carbon fibers, as seen in the higher x- and y-stresses relative to the isotropic materials.

The highest stresses that develop in the PCHX are in the two-directions with longitudinal reinforcement by carbon fibers, which are the regions with highest stiffness and strength. The mechanical loading results reveal that a PCHX – if appropriately designed – can withstand the stresses that develop from the pressurized fluids in LNG heat exchange processes. Nonetheless, the high magnitudes of these stresses represent a significant fraction of the yield strength of this material, which

could lead to plastic deformation over time via creep. Furthermore, the addition of thermal loading could reduce the stiffness and strength of the polymer composite, especially as the fluid temperature approaches the glass transition temperature of the material system, which could lead to failure.

Locations of Maximum Stress Magnitudes

The location of the maximum stress magnitudes aligned for the PCHX and HXs fabricated from isotropic materials for several of the directional stresses. Figure 62 shows the location of the x-, y- and xy-direction stresses as a function of airside pressure. In general, the location of the maximum directional stresses changed when the airside pressure was increased from 0.5 MPa to 5.0 MPa; at the lower pressure, the waterside had less reinforcement because the waterside has fewer fins but at the high pressure, the load was sufficiently high to change the maximum stress location to the gas side despite the additional fin. Please note that the stresses were independent of the axial length along the heat exchanger due to the symmetry of the loading and boundary conditions.

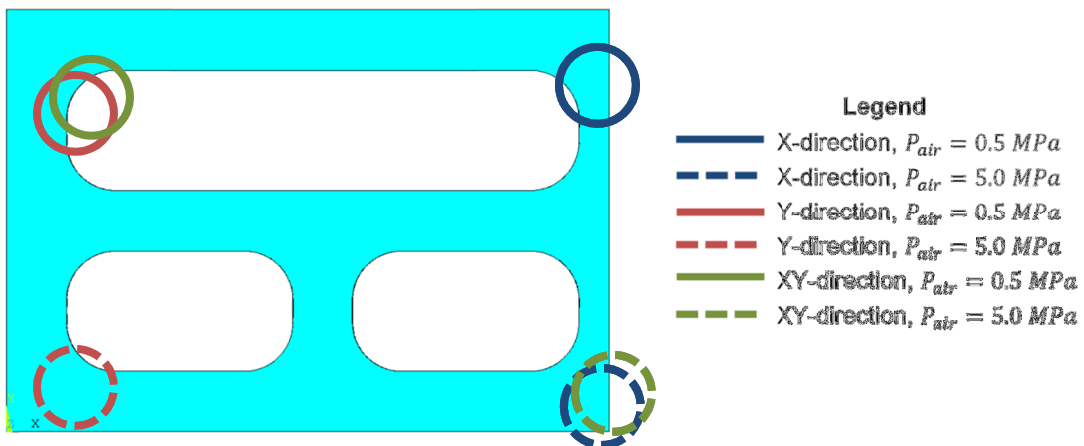


Figure 62: Maximum x-, y-, and xy-stress locations in isotropic and anisotropic heat exchangers

The location of the maximum z-direction stress was different in the PCHX and isotropic HX for an airside pressure of 0.5 MPa. In the PCHX, the maximum occurred in the upper left corner of the waterside channel (near the maximum xy-direction stress for an airside pressure of 0.50 MPa) and in the isotropic HX, the maximum occurred in the upper right corner of the waterside channel (near the maximum x-direction stress for an airside pressure of 0.50 MPa). In both the PCHX and isotropic HX, the maximum z-direction stress for an airside pressure of 5.0 MPa occurred in the lower left corner of the leftmost airside channel (near the maximum y-direction stress for an airside pressure of 5.0 MPa).

Simplification of Modeling

A study was conducted to determine whether an isotropic material with properties that were between the longitudinal and transverse properties of the polymer composite could represent the mechanical behavior of the composite. Modeling a set of transversely isotropic materials as a single isotropic material would simplify the modeling process and reduce the required computation time.

For the heat exchanger model using isotropic material properties, a range of elastic moduli (2 to 6 GPa) and range of Poisson's ratios (0.24 to 0.44) served as the input mechanical properties because these values cover most of the range of the orthotropic hygrothermally-aged mechanical properties previously used for modeling. The applied waterside pressure was 5.87 MPa and the applied airside pressure was 0.40 MPa, which were the values for the maximum fluid pressures seen in the Das Island third LNG heat exchanger train. Table 14 shows the maximum stress magnitudes resulting from the pressure application in the transversely isotropic and

isotropic heat exchanger models. The results reveal that, in general, the isotropic model significantly underestimates the maximum x- and y-direction stress magnitudes and significantly overestimates the maximum xy-direction stress magnitudes relative to the transversely isotropic modeling results. The results indicate that, over the range of isotropic properties studied, the stress distributions of isotropic models do not replicate the stress distributions of a transversely isotropic heat exchanger model. As such, the transversely isotropic model cannot be simplified to an isotropic material with averaged properties.

Table 14: Maximum stresses from isotropic and transversely isotropic finite element heat exchanger models

Elastic Modulus (GPa)	Poisson's Ratio	Max. X-Stress (MPa)	Max. Y-Stress (MPa)	Max. Z-Stress (MPa)	Max. XY-Stress (MPa)	Max. YZ-Stress (MPa)	Max. XZ-Stress (MPa)
2	0.24	33.5	42.5	8.3	23.4	1.7	3.4
	0.34	33.7	43.0	11.9	23.4	2.4	4.9
	0.44	34.7	43.9	15.9	23.5	3.1	6.3
4	0.24	33.5	42.4	8.3	23.4	1.7	3.4
	0.34	33.8	43.0	11.9	23.4	2.4	4.9
	0.44	34.6	44.3	15.9	23.5	3.1	6.3
6	0.24	33.6	42.5	8.3	23.4	1.7	3.4
	0.34	33.8	43.0	11.9	23.4	2.4	4.9
	0.44	34.7	44.3	15.9	23.5	3.1	6.3
Transversely isotropic		53.7	73.7	10.0	14.7	3.0	3.1

Summary of Findings

A mesh independence study was performed on a structural model of a polymer composite heat exchanger and it was found that the x-, y-, z-, and xy-direction stresses were most important for the present analysis. Analysis of the heat exchangers fabricated from corrosion-resistant materials revealed that the isotropic materials have more uniform directional stress magnitudes than anisotropic polymer composite heat exchangers, which experience higher stress magnitudes in directions with longitudinal fiber reinforcement. The stresses resulting from an airside pressure

of 5.0 MPa and a waterside pressure of 0.5 MPa were below the yield strength of the polymer composite, although a more sophisticated model incorporating thermal stresses and temperature-dependent mechanical properties is required to more thoroughly assess the structural integrity of polymer composite heat exchangers under combined thermomechanical loading.

Chapter 6: Thermal Modeling

Motivation

A laboratory scale polymer composite heat exchanger was assembled to assess the effect of the addition of carbon fibers to the polymer matrix on the heat transfer rate of the heat exchanger. The laboratory scale heat exchanger was assembled from finned plates that were injection molded and thus subject to anisotropic thermal properties. The experimental studied served to assess the improvement in heat transfer rate and as a validation tool for a thermal finite element model. After calibrating the thermal performance of the finite element model, the heat transfer rates of heat exchangers fabricated from competitive corrosion-resistant materials were compared to those for the PCHX over a range of fluid properties. The modeling allowed for thorough investigation of the temperature profile of the heat exchanger and later served as a baseline from combined thermomechanical loading studies.

Experimental Study

Test Facility

In order to explore the behavior of a PCHX in a gas-to-liquid heat exchange application, the thermal performance of a laboratory-sized heat exchanger was studied experimentally. The heat exchanger test facility is shown in Figure 63. Ambient air is drawn at a flowrate of 1800-3000 cm³/s by a fan before passing through a heater and a flow straightener and being directed downstream toward the heat exchanger. Air velocity is measured at a downstream point where the velocity profile is fully developed. A manifold then directs the flow into the PCHX, where the

temperature is measured at the inlet and outlet. Finally, the air is exhausted into the ambient. Cooling water is directed to the heat exchanger from the building cold water supply. The flow rate is measured using a vortex-shedding flow meter and the temperature is stabilized to a constant value using an inline heater. The water temperature is measured at the inlet and at the outlet of the PCHX.

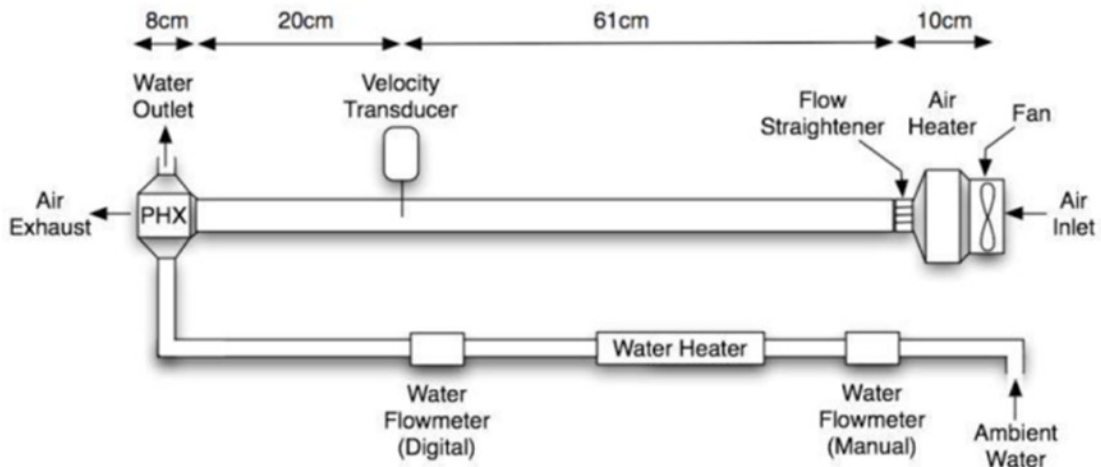


Figure 63: Heat exchanger test facility [34]

Although PCHXs are proposed for seawater cooling applications, in particular in LNG applications at the Das Island processing facility, natural gas (which is primarily methane) was not used as the working fluid in the experimental study because: (1) air has a considerably lower specific heat capacity ($1006 \text{ J/kg}\cdot\text{K}$) than methane ($2293 \text{ J/kg}\cdot\text{K}$) at 50°C and thus a higher temperature drop and lower experimental error is achieved with air and (2) safety issues are minimized. As air was the experimental working fluid, the thermal model also used air as the working fluid. A seawater-natural gas heat exchanger would have a less dominate gas side thermal resistance than a seawater-air heat exchanger and thus, the heat exchanger

geometry would be adjusted to further reduce the conduction resistance in this application.

Temperature and flowrate measurements of the air and water were acquired real-time on a desktop computer using LabVIEW software, which simultaneously displayed and stored the acquired data. The air velocity transducer was part number FMA-902-V-S, provided by Omega Engineering, and the water flow meter was part number FLP04-L1NA, provided by Sparling Instruments. The air and water meters provided digital outputs that were processed and recorded through the computer discussed previously.

The air heater was Farnam Custom Products part number 20055K111, which was capable of providing up to 200 W of heat via a resistive wire coiled within an enclosure. A water heater was used to compensate for variation in the building water supply temperature. The water was heated using Omegalux model AHPF-121, available from Omega Engineering and capable of providing up to 1200 W. The heaters were powered using variable voltage output transformers to regulate the heat input to the fluids.

Temperature measurements were found using J-type iron-constantan thermocouples with a 1/16" stainless steel sheath. The thermocouples were placed at the inlet and outlet of six of the twelve air channels. The water temperature was measured using two thermocouples, one at the inlet and one at the outlet, because the water temperature was not expected to change significantly. The thermocouples served to verify this assumption.

The thermocouples were connected to a USB-TC thermocouple input module from Measurement Computing. Cold junction compensation was provided through two integrated high resolution temperature sensors in the module. The signals from the flow meters were read using a USB-6008 multifunction data acquisition unit from National Instruments. The input modules were connected to a desktop computer running LabVIEW 8.5 to acquire, process and store experimental data.

Heat Transfer Rate in Crossflow Heat Exchanger

Prior to discussing experimental results, an overview of analytical modeling of a crossflow heat exchanger is presented. The heat transfer rate (\dot{q}) of a heat exchanger can be calculated using the ε -NTU method, as shown in Equation 27:

$$\dot{q} = \varepsilon \dot{q}_{max} = \varepsilon C_{min} (T_{i,1} - T_{i,2}) \quad (27)$$

where C_{min} is the smallest heat capacity of the two fluids. The effectiveness (ε) of a crossflow heat exchanger with both fluids unmixed can be calculated according to Equation 28:

$$\varepsilon = 1 - e^{\left[\left(\frac{1}{C_r} \right) (NTU)^{0.22} \left\{ e^{[-C_r (NTU)^{0.78}] - 1} \right\} \right]} \quad (28)$$

where C_r is the ratio of the fluids' heat capacities and NTU is the number of transfer units, defined by Equation 29.

$$NTU = \frac{UA}{C_{min}} \quad (29)$$

The overall thermal conductance (UA) of the heat exchanger was calculated using a network of convection and conduction thermal resistances in the heat exchanger module, as shown in Equation 30:

$$UA = \frac{1}{\frac{1}{\eta_{fin,o,1} h_1 A_{t,1}} + \frac{t_b}{k A_w} + \frac{1}{\eta_{fin,o,2} h_2 A_{t,2}}} \quad (30)$$

where h is the heat transfer coefficient, η_f is the surface efficiency (a function of fin efficiency) and k is the through wall thermal conductivity.

Entry Region

The maximum air flowrate used in this laboratory prototype PCHX was 3000 cm³/s, which translates to a maximum Reynolds number of ~1900 in the heat exchanger channels. Therefore, the flow can be considered exclusively laminar. Due to the short length of the heat exchanger, thermal and hydrodynamic entry lengths must be considered prior to calculating heat transfer coefficients and friction factors.

The hydrodynamic entry length ($x_{fd,h}$) is the axial position at which the momentum boundary layer thickness is equal to half the width of the channel. It can be written as [94]:

$$\frac{x_{fd,h}}{D_h} \approx 0.06 Re_{D_h} \quad (31)$$

where D_h is the channel hydraulic diameter and Re_{D_h} is the Reynolds numbers. Using the lowest Reynolds number seen in the experiment (645) and the airside hydraulic diameter (6.5 mm), the shortest hydrodynamic entry length is 25 cm, which is longer than the channel length and therefore, the velocity profile of the air is always developing in the prototype heat exchanger.

The thermal entry length ($x_{fd,th}$) can be approximated by Equation 32 [95]:

$$\frac{x_{fd,th}}{D_h} \approx 0.05 Re_{D_h} Pr \quad (32)$$

where Pr is the Prandtl number. At the lowest experimental flowrate, the thermal entry region is 15 cm long and thus, fully developed conditions are never achieved in the present heat exchanger.

Friction Factor

The product of the fully developed friction factor (f_{fd}) and the Reynolds number is a function of the channel aspect ratio AR , defined as [96]:

$$f_{fd} = \frac{96}{Re_{D_h}} \left(1 - 1.3553AR + 1.9467AR^2 - 1.7012AR^3 + 0.9564AR^4 - 0.2537AR^5 \right) \quad (33)$$

Using this result and the dimensionless position (L^+), the apparent friction factor is [96]:

$$\bar{f} \approx \frac{4}{Re_{D_h}} \left[\frac{3.44}{\sqrt{L^+}} + \frac{\frac{1.25}{4L^+} + \frac{f_{fd}Re_{D_h}}{4} - \frac{3.44}{\sqrt{L^+}}}{1 + \frac{0.00021}{(L^+)^2}} \right] \quad (34)$$

where the dimensionless position is a function of channel length L :

$$L^+ = \frac{L}{D_h Re_{D_h}} \quad (35)$$

Nusselt Number

The Nusselt number for a laminar, hydrodynamically and thermally fully developed flow in a rectangular duct exposed to a uniform heat flux or uniform wall temperature is provided by Shah and London [96]. The correlation for constant wall temperature is:

$$Nu_{fd,Temp} = 7.541 \left(1 - 2.610AR + 4.970AR^2 - 5.119AR^3 + 2.702AR^4 - 0.548AR^5 \right) \quad (36)$$

and the correlation for constant heat flux is:

$$Nu_{fd,H} = 8.235 \left(1 - 2.042AR + 3.085AR - 2.477AR^3 + 1.058AR^4 - 0.186AR \right) \quad (37)$$

where AR is the channel aspect ratio.

Since the boundary condition in the heat exchanger was not known a priori on the airside, the average of the values calculated in Equations 36 and 37 were used for the air heat transfer coefficient. For the waterside, the heat transfer coefficients were high and there was a near-zero axial temperature increase. Thus, a constant temperature boundary condition, along the waterside wall was assumed and Equation 31 was used for the momentum entry length.

The values of the Nusselt number for simultaneously hydrodynamically and thermally developing flow in a rectangular duct with constant wall temperature and constant heat flux for $Pr = 0.72$ were provided by Wibulswas [95]. A later refinement by Kakac [97] provided a method to interpolate the table of data and correct for Prandtl number effects. A dimensionless length appropriate for a thermally developing flow is L^* , sometimes referred as the inverse Graetz number (Gz):

$$L^* = \frac{1}{Gz} = \frac{L}{D_h Re_{D_h} Pr} \quad (38)$$

Experimental Results

For the current experiments, while the air flow rate was varied from 1800 cm^3/s to 3000 cm^3/s , the volumetric flowrate of the cooling water was held constant at $\sim 60 \text{ cm}^3/\text{s}$, the water inlet temperature was always 15°C and the air inlet temperature was always 50°C . Using the inlet and outlet temperatures and the measured flow

rates, the heat transfer rate (q) can be calculated with a simple heat balance on either the airside or the waterside, as:

$$\dot{q} = \dot{m}_1 c_{p,1} (T_{i,1} - T_{o,1}) = \dot{m}_2 c_{p,2} (T_{o,2} - T_{i,2}) \quad (39)$$

where \dot{m} is the fluid mass flowrate, c_p is the fluid specific heat capacity and T_i and T_o are fluid inlet and outlet temperatures. However, due to the negligible water temperature rise ($< 0.06^\circ\text{C}$) and the relative uncertainty of the water temperature measurements experienced in these experiments, only the airside sensible heat loss will be used to establish the PCHX heat transfer rate.

The values calculated using the airside of Equation 34 are plotted in Figure 64 with error bars indicating the relatively high experimental uncertainty of 16%, which was caused by the small magnitude of the airside temperature drop (6°C at $1800 \text{ cm}^3/\text{s}$ and 5°C at $3000 \text{ cm}^3/\text{s}$) relative to the thermocouple uncertainty ($\sim 0.44^\circ\text{C}$). Figure 64 reveals that the laboratory PCHX successfully transferred between 12 W and 16 W across the range of imposed airside flow rates. As expected, the heat transfer rate increased asymptotically with increasing mass flowrate, reflecting the decrease in the air temperature drop (and resulting increase in the average temperature difference from the air to the water) across the heat exchanger as the flow rate increased. An analytical prediction of the heat transfer rate can be obtained using Equations 22-25 with assumed values of thermal conductivity. As may be seen in Figure 64, a prediction based on the raw polymer thermal conductivity of $0.25 \text{ W/m}\cdot\text{K}$ underestimates the heat transfer rate by approximately 40%. Consequently, it is clear that the presence of the carbon fibers enhanced the thermal transport capability of the PCHX.

The relatively larger experimental uncertainty in this series of tests made it difficult to extract a precise value of effective thermal conductivity from these results. However, as can be seen in Figure 64, while a prediction based on the presumed aligned direction conductivity, $k = 9.25 \text{ W/m}\cdot\text{K}$, provides a large overestimate of the heat transfer rate, a prediction based on the presumed transverse thermal conductivity, $k = 0.73 \text{ W/m}\cdot\text{K}$, falls within the error bracket of the measured values. This result is not unexpected because the through wall conductivity, which is expected to be near the transverse thermal conductivity, has a much more significant effect on heat transfer rate than does the aligned thermal conductivity expected in the fins. It is noteworthy that the harmonic mean of the aligned and transverse thermal conductivities, defined as:

$$k_{harmonic} = \frac{2k_L k_T}{k_L + k_T} \quad (40)$$

can be expected to provide a first estimate of the effective conductivity in a composite material with multi-dimensional heat flow [98]. For the stated conditions, $k_{harmonic}$ was $1.35 \text{ W/m}\cdot\text{K}$ and provided very satisfactory agreement with the experimental data, as shown in Figure 64.

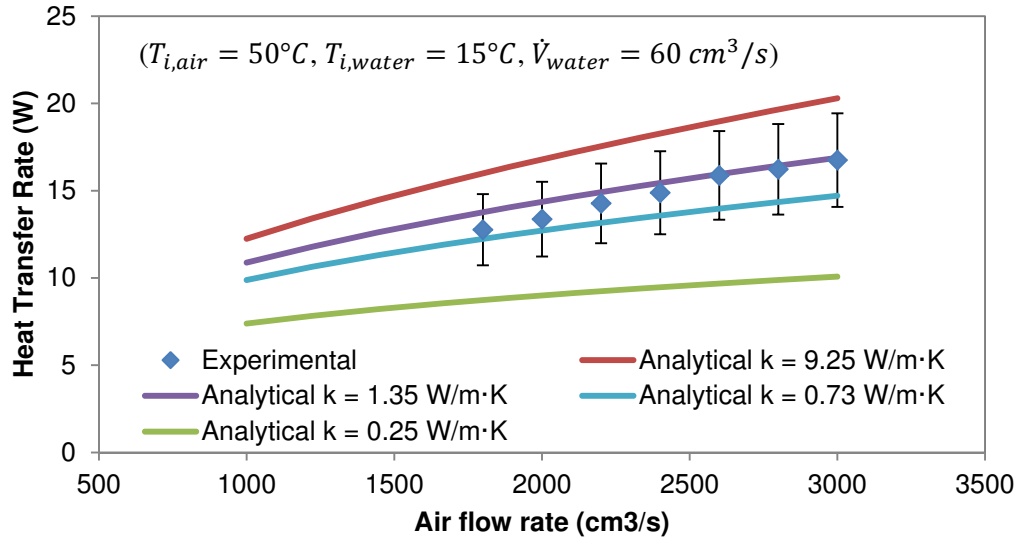


Figure 64: Experimental and analytical heat transfer rates

Numerical Study

Purpose

Numerical modeling was employed to assess the effect of anisotropy on the heat transfer rate of polymer composite heat exchangers. Simplified analytical models are useful when using average heat transfer coefficients, average fluid temperatures and isotropic materials; however, the usefulness of such models is limited when exploring the effects of local fluid temperatures and local heat transfer coefficients, as well as anisotropic material properties. Numerical modeling – as a result of the advent of high performance computing – allows for reasonably quick and accurate solutions to the differential equations governing heat transfer for an endless collection of conditions. Furthermore, the complexity of the modeled problem is limited only by the available inputs to the model and computation speed. As such, finite element modeling was utilized to assess the local and global performance of polymer composite heat exchangers, which was compared to the performance of isotropic heat

exchangers to determine the improvement relative to raw polymers and the performance gap remaining between polymer composites and metals.

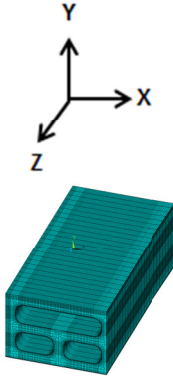
Model Parameters

Material Properties

The material properties of the polymer composite that were input into the finite element model are provided in Table 15.

Table 15: Thermal material properties input into finite elemnt model

Property	Plate	Fin
$k_x (W/m \cdot K)$	9.25	0.73
$k_y (W/m \cdot K)$	0.73	9.25
$k_z (W/m \cdot K)$	0.73	0.73
$\alpha_x (\mu m/m/^\circ C)$	1.98	122
$\alpha_y (\mu m/m/^\circ C)$	122	1.98
$\alpha_z (\mu m/m/^\circ C)$	122	122



Geometry

The heat exchanger studied for the thermal modeling of the PCHX had identical dimensions to the heat exchanger studied for structural modeling. Please see the geometry section of the structural modeling section for more information. The air inlet and water outlet are identified in Figure 65, reflecting the counterflow configuration of the modeled heat exchanger.

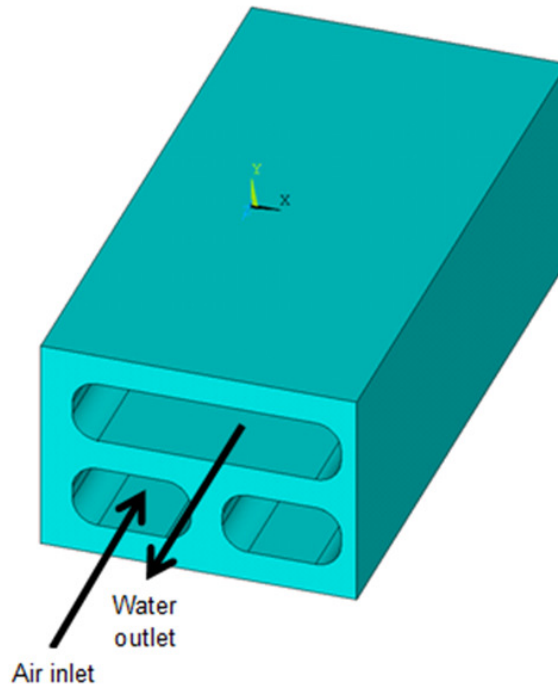


Figure 65: Fluid inlet and outlet on heat exchanger

It is noteworthy that the experimental heat exchanger is in a cross-flow configuration whereas the numerical model heat exchanger is in a counter-flow configuration. The experimental heat exchanger was configured as cross-flow to allow for simpler manifolds and the numerical model was configured as counter-flow for higher effectiveness, which may be an important factor in later optimization of the PCHX. For comparison of cross-flow and counter-heat exchangers, an F factor is typically applied to the log mean temperature difference (LMTD) of the counter-flow heat exchanger. The F factor is 1 when the temperature change of one fluid is negligible [99], which was the case for the validation studies since the temperature rise of the water was always $< 0.06^{\circ}\text{C}$. Thus, it was possible to compare the heat transfer performance of the cross-flow and counter-flow heat exchangers directly.

Fluid Characteristics

Nusselt numbers for laminar, hydrodynamically and thermally developing flow based on the work of Shah and London [96] were used to calculate local heat transfer coefficients. Nusselt numbers for uniform surface temperature were used on the waterside due to the high heat transfer coefficient and an average of Nusselt numbers for uniform surface temperature and uniform surface flux were used for the airside because the surface condition was initially unknown. The water temperature was assumed constant at 15°C and the air temperature was estimated using the energy balance and an inlet temperature of 50°C based on the experimental setup. The pressure of both fluids was assumed to be 100 kPa.

Figure 66 shows the air and water heat transfer coefficients as a function of axial distance, reflecting the counterflow configuration and the entry points of the water and air on opposite sides of the heat exchanger. The low airside heat transfer coefficient is the dominant thermal resistance in the heat exchanger.

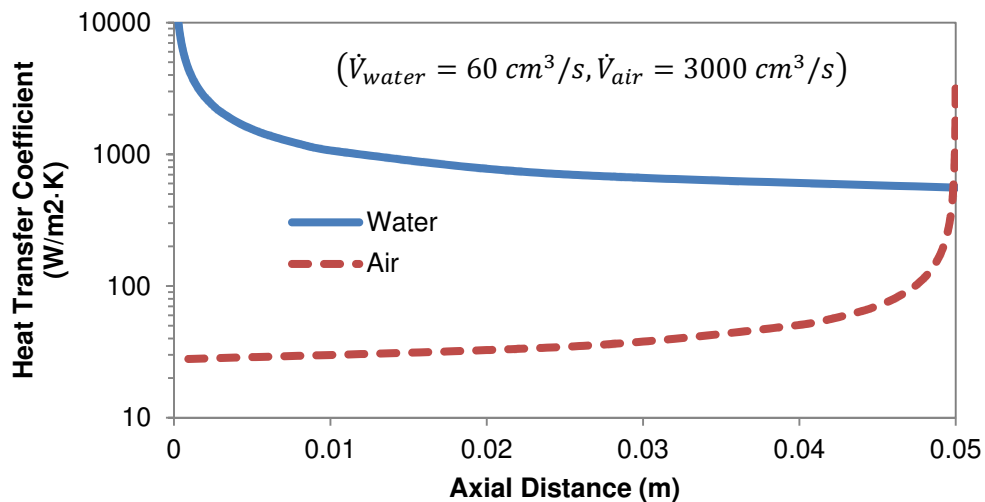


Figure 66: Calculated local heat transfer coefficients for air and water in a counter flow configuration

Model Validation

The finite element model was validated against the experimental heat transfer rate results to ensure the model accurately captured thermal performance of the PCHX. The heat transfer rate of the numerical model was calculated by integrating the surface heat flux over the area separating the air and water channels. Figure 67 compares the experimental and numerical heat transfer rates based on a constant water flow rate of $60 \text{ cm}^3/\text{s}$. The numerical heat transfer rates, using the aligned and transverse thermal conductivities predicted by the Nielsen Equation (described previously) agreed with experimental results within experimental uncertainty at all airside flow rates.

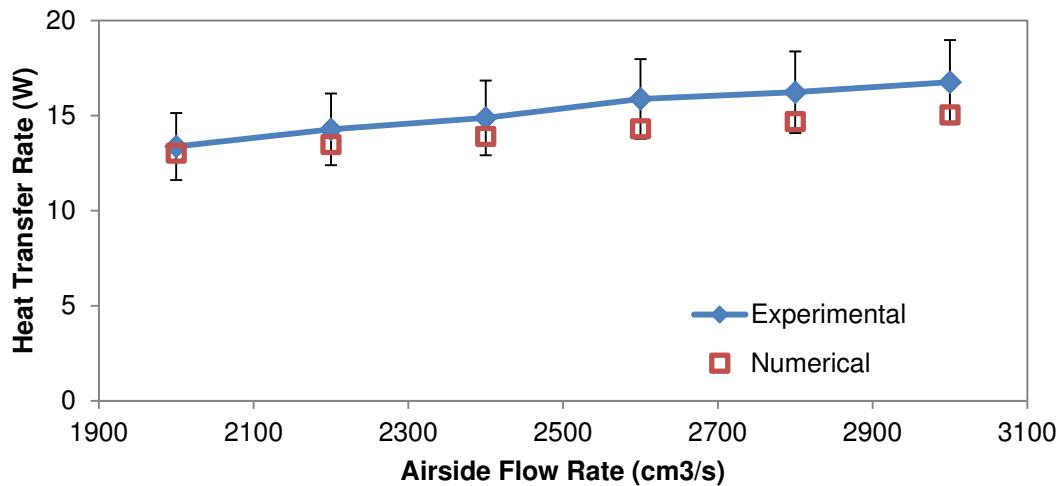


Figure 67: Numerical and experimental results

As shown in Figure 67, the disparity between the experimental and numerical heat transfer rates increases as the airside flow rate increases and thus, the airside heat transfer coefficient increases. It is possible that the growing disparity is the result of the conservative assumption that the through wall conductivity in the heat exchanger plates was equal to the transverse thermal conductivity of a fiber reinforced polymer

with perfectly aligned fibers. As the airside heat transfer coefficient increases and the airside thermal resistance decreases, the transverse thermal conductivity contributes more significantly to the heat exchanger's total thermal resistance. The thermal conductivities were modeled as such because the present modeling is most conservative and thus, any practical implementation of injection molded polymer composite heat exchangers should lead to higher heat transfer rates than those predicted in the present study.

Please note that the numerical heat transfer rate, which was found by multiplying the heat transfer rate of one symmetric module by six to approximate the heat transfer rate of the experimental assembly (three modules) provides only a first order comparison. In the experimental HX assembly, two of the three airside channel levels have water channels both above and below, which is different than the numerical model, which only considers heat transfer between one airside channel level and one adjacent waterside channel level. Furthermore, the thermal conductivity applied in the numerical model is a worst case scenario and it is expected that the through wall thermal conductivity of the experimental HX is higher. Consequently, the comparison of the numerical and experimental heat transfer rates is not valid as a direct comparison but nonetheless serves to ensure the model provides a reasonable heat transfer rate. In all heat transfer rate comparisons that follow, only one set of adjacent air and water channels is considered to avoid this complication.

Heat Transfer Rate Comparisons

The heat transfer rate of a single set of adjacent air and water channels was compared with predictions for an identical heat exchanger fabricated from Titanium

Grade 2 ($k=16.4 \text{ W/m}\cdot\text{K}$) and PTFE ($k=0.28 \text{ W/m}\cdot\text{K}$), two materials previously used in corrosion resistant heat exchangers. The air pressure was set to 100 kPa, 500 kPa and 5000 kPa and the air inlet temperature was set to 50°C and 150°C, in order to match the experimental parameters and cover a range of temperature and pressures seen in gas-liquid heat exchangers. For all simulations, the air flowrate was 1000 cm^3/s . The airside heat transfer coefficients for the range of conditions studied are shown in Figure 68. The results show that the airside pressure significantly affects the heat transfer rate (assuming constant volumetric flowrate) because of the significant increases in air density and thus, mass flow rate as the pressure increases. The inlet temperature of the water has a much less significant effect in heat transfer coefficient, as high temperatures lead to slightly lower heat transfer coefficients because density is inversely proportional to temperature.

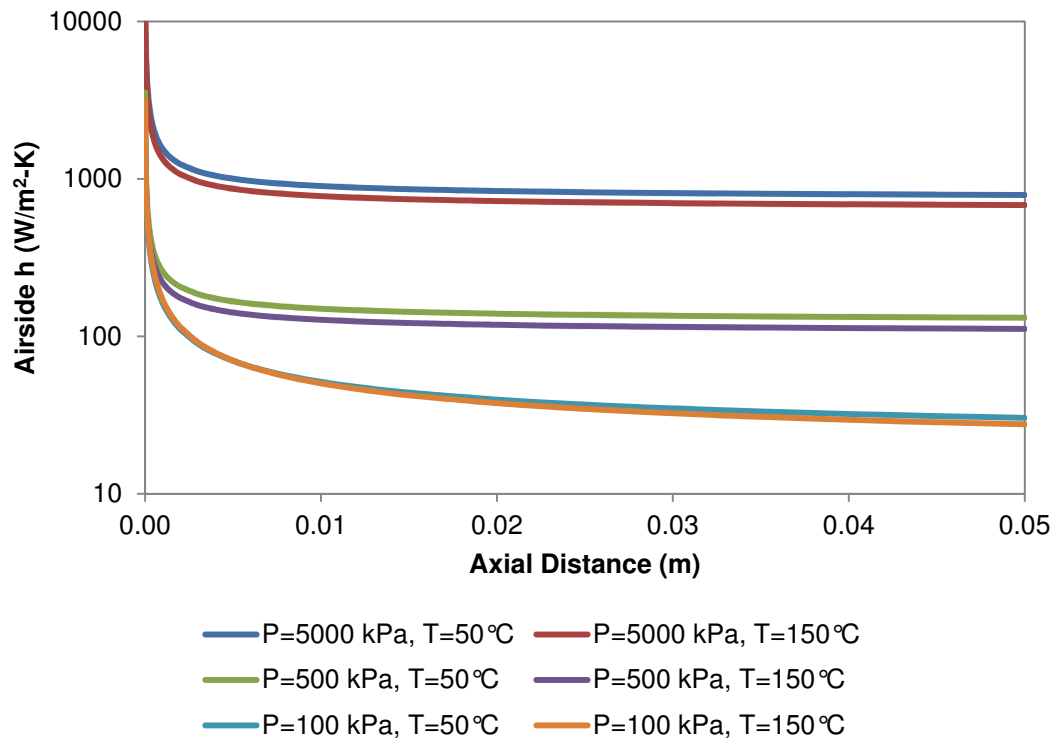


Figure 68: Airside heat transfer coefficients over range of conditions

For all simulations, the water flow rate was $20 \text{ cm}^3/\text{s}$ and the water inlet temperature was 15°C . The heat transfer rate results are shown in Figure 69. For an airside pressure of 100 kPa, the PCHX performed 70.0% better than the PTFE HX and 28.2% worse than the titanium HX. As the airside pressure increased and the airside heat transfer coefficients improved, the composite further outperformed the PTFE (by 87.0% and 112.7% at 500 kPa and 5000 kPa, respectively) and further underperformed relative to the titanium (by 48.3% and 69.6% at 500 kPa and 5000 kPa, respectively). These results reflect the growing importance of the through-wall conduction resistance as the pressure increases diminish the convective resistance. Please note that the use of conservative through wall thermal conductivity predictions contributes significantly to the heat transfer performance of the PCHX and that practical implementation of PCHX might achieve higher through wall conductivities and lower aligned conductivities than those applied for the present analysis.

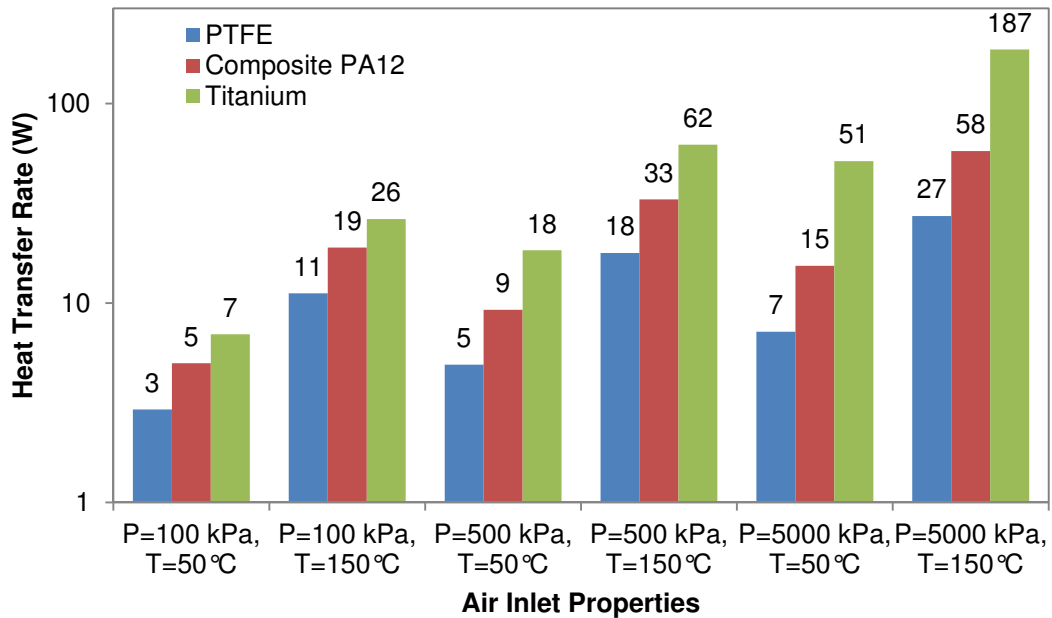


Figure 69: Heat transfer rate of heat exchangers made from various materials

The higher heat transfer rate of the titanium heat exchanger relative to the PCHX can be partially attributed to better spreading, which resulted from the much high z-direction conductivity of the titanium (16.4 W/m·K) relative to the low z-direction conductivity of the polymer composite (0.73 W/m·K). The effect of this large disparity in z-direction conductivity is evident in Figure 70, which shows the temperature profiles of the titanium and polymer composite heat exchangers. The lower wall temperature of the titanium heat exchanger is also evident, which is required to achieve a higher heat transfer rate at the same heat transfer coefficient and similar fluid temperatures (i.e., the average gas temperature in the titanium HX is slightly lower than in the PCHX because more heat is removed from the gas in the titanium HX). For example, at the air inlet of the heat exchangers, the maximum temperature of the PCHX approaches 50°C and the titanium HX maximum is about 40°C. The higher temperature seen in the PCHX could play an important role in the development of thermomechanical stress, discussed in more detail in Chapter 7. The cooler temperature of the wall on the waterside of the PCHX (i.e., 15-20°C) relative to the same location in the titanium HX (i.e., 30-35°C) hints at the improved heat transfer rate of the HX, resulting from a larger temperature difference between the wall and fluid throughout the heat exchanger axial length.

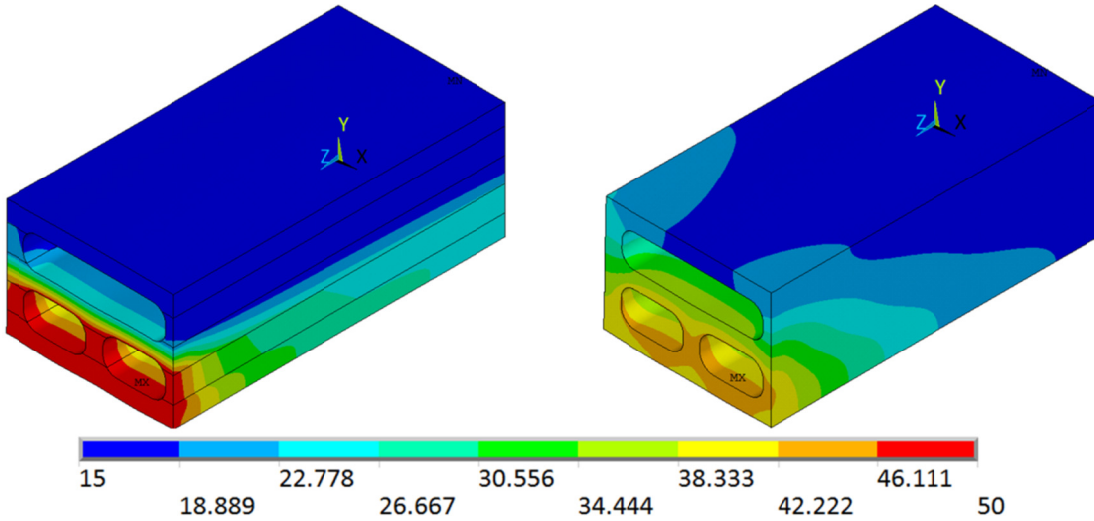


Figure 70: Temperature distributions of PCHX (left) and Ti HX (right) (units: °C)

Discussion

Analytical Heat Transfer Rate Predictions

A critical component of the present heat transfer analysis is that the dominant thermal resistance in a gas-to-liquid heat exchanger is the gas side convective resistance, despite the modest through wall thermal conductivity of the polymer composite. The heat transfer rate can be estimated according to Equations 41-42:

$$q = UA \times LMTD \quad (41)$$

$$UA = \frac{1}{R_{th}} = \frac{1}{(\eta_{fin}hA)_{cold}} + \frac{t}{kA} + \frac{1}{(\eta_{fin}hA)_{hot}} \quad (42)$$

where q is the heat transfer rate, UA is the overall conductance of the heat exchanger, $LMTD$ is the log mean temperature difference of the two fluids, η is the surface efficiency, h is the heat transfer coefficient, A is the area, t is the wall thickness and k is the through wall thermal conductivity. For the heat exchanger geometry of the present study, an assumed $LMTD$ of 50°C and a waterside heat transfer coefficient of $1000 \text{ W/m}^2\cdot\text{K}$, the effect of the airside heat transfer coefficient on heat transfer rate is shown in Figure 71. It can be seen that – for low gas side heat transfer coefficients

(i.e. $< 100 \text{ W/m}^2\cdot\text{K}$), increasing the through wall thermal conductivity above $\sim 10 \text{ W/m}\cdot\text{K}$ has little effect on heat transfer rate. However, as the heat transfer coefficient of the gas increases, the effect of the through wall thermal conductivity increases and thus, higher conductivities are required to achieve higher heat transfer rates. Thus, for high gas pressure and density, improving the through wall thermal conductivity of polymer composites will result in the greatest improvement in heat transfer rate.

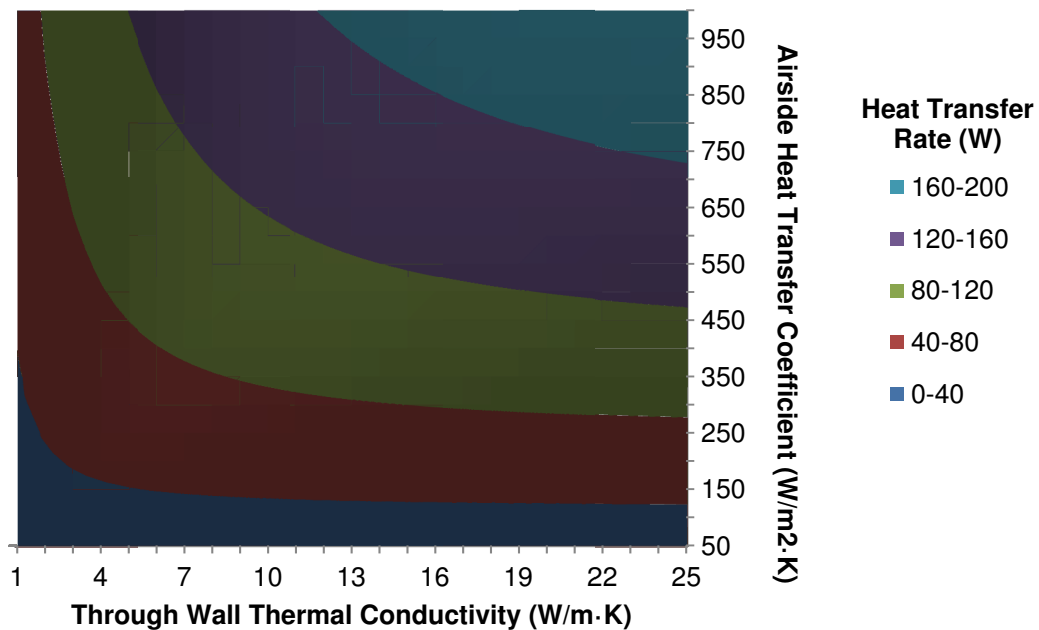


Figure 71: Map of heat transfer rate using simplified network model

As seen above, the heat transfer rate is a function of the surface efficiency, which is a function of the fin efficiency. In injection-molded polymer composite finned plates, the fin longitudinal thermal conductivity is high because it is in the same direction as the flow. Figure 72 shows the fin efficiency as a function of longitudinal thermal conductivity and heat transfer coefficient. Although injection-molded plate-fins suffer from low through wall conductivity, the longitudinal

conductivity of the fins is sufficiently high to attain much higher fin efficiencies than those seen in raw polymers. At a longitudinal conductivity of 10 W/m·K, polymer composites achieve a fin efficiency of ~80% for a heat transfer coefficient of 200 W/m²·K, whereas a raw polymer achieves a fin efficiency of only ~20%. This behavior is particularly important for the gas side of gas-to-liquid heat exchangers where area enhancement is particularly important to achieve higher heat transfer rates. Based on these observations, it is shown that the fin longitudinal conductivity can be sufficiently high to offer comparable fin efficiencies to metals at low heat transfer coefficients, where additional fin area greatly improves heat transfer rate. However, the fin longitudinal conductivity is the maximum achievable value for the present modeling and the conductivity varies with manufacturing process (i.e., extrusion could provide higher conductivity in the direction of extrusion).

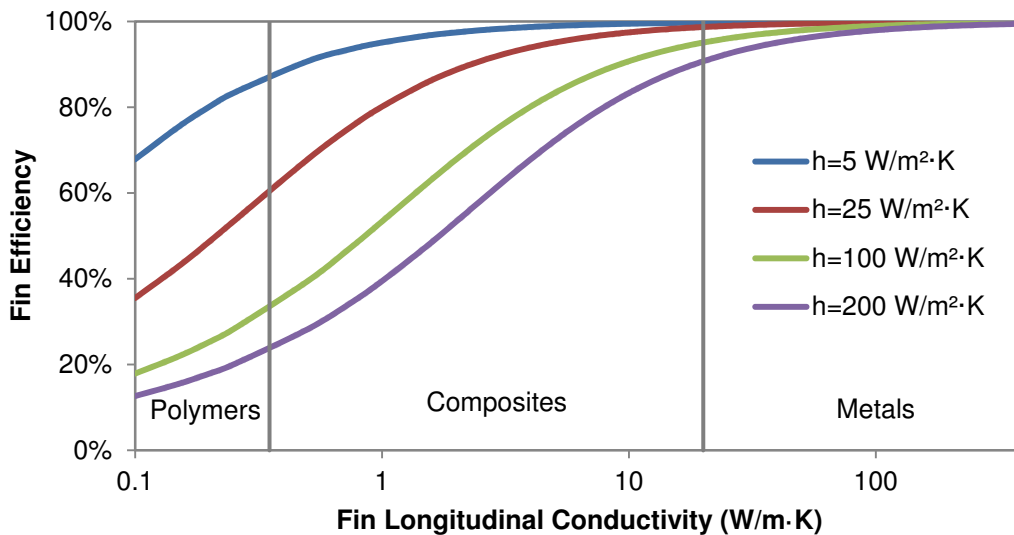


Figure 72: Fin efficiency as a function of conductivity and heat transfer coefficient (fin height: 5.0 mm, fin thickness: 2.5 mm)

Summary of Findings

The experimental polymer composite heat exchanger apparatus revealed that the effective thermal conductivity of the anisotropic polymer composite was approximately equal to the harmonic mean of the longitudinal and transverse conductivities for the present study. As one would expect, the heat transfer rate of the PCHX was closer to an analytical model using only the transverse thermal conductivity than to an analytical model using the longitudinal conductivity, which confirmed that the through wall conductivity is the more important thermal conductivity for the present heat exchanger geometry and mold design.

Thermal modeling of polymer composite heat exchangers in gas-liquid applications revealed that the dominant thermal resistance was the airside heat transfer coefficient while operating in at near ambient conditions. In these conditions, the higher thermal conductivity of titanium offered only modest improvements in heat transfer rate (28% better than the PCHX), although the PCHX outperformed raw PTFE by 70%. However, as the airside pressure increased at constant airside volumetric flowrate, the airside convective resistance diminished and the through wall thermal conductivity became the dominant thermal resistance. At an airside pressure of 5000 kPa, the PCHX outperformed PTFE by 113% but underperformed titanium by 70%.

Chapter 7: Thermomechanical Modeling

Motivation

It is well documented that the injection molding of polymer-fiber composites results in local and global anisotropy in thermomechanical properties. In particular, the stiffness, deformation behavior, coefficient of thermal expansion and thermal conductivity vary significantly with fiber orientation. The present thermomechanical modeling aimed to quantify the effects of the mismatch in thermomechanical properties in various regions of the polymer composite heat exchanger. Combined thermomechanical loading in PCHXs is of particular interest due to the anisotropy present in the elastic modulus and coefficient of thermal expansion, not only within the same section of the heat exchanger (i.e., fins or plates) but also between adjacent sections that have a direct interface (i.e., where the fins meet the plates). Thermomechanical modeling must inform the heat exchanger design process to ensure the desired heat transfer performance is achieved while ensuring the structural integrity of the heat exchanger despite local and global anisotropy in thermomechanical properties.

Thermal Stress Development

Elastic axial stress (σ) resulting from thermal expansion of a constrained structural member can be calculated according to:

$$\sigma = \alpha E \Delta T \quad (43)$$

where α is the coefficient of thermal expansion (CTE), E is the elastic modulus and ΔT is the temperature change from the initial constrained, unstressed state. The elastic

modulus and CTE of various polymers and metals can be found in Figure 73, where it can be seen that polymers have low moduli (~1 GPa) and high CTEs (~100 $\mu\text{m}/\text{m}/^\circ\text{C}$) whereas metals have higher moduli (~100 GPa) and modest CTEs (~10 $\mu\text{m}/\text{m}/^\circ\text{C}$).

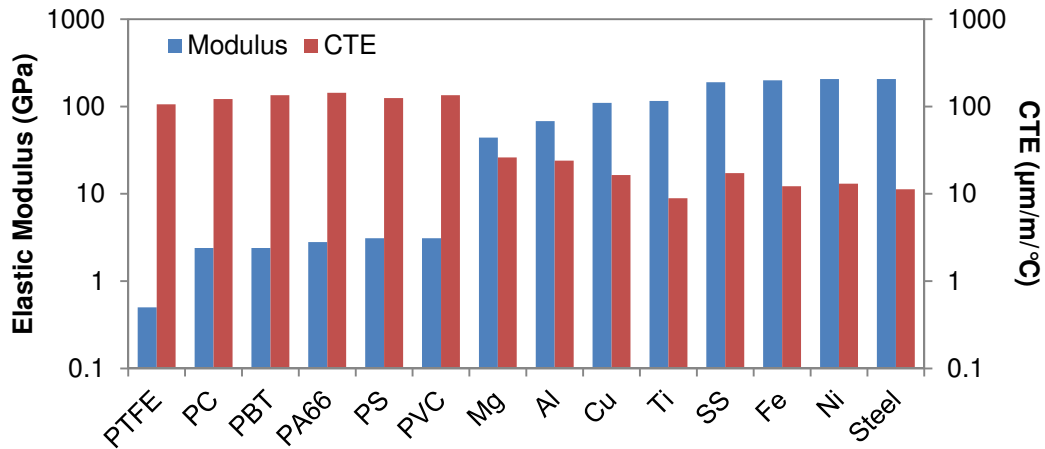


Figure 73: Elastic modulus and CTE of polymers and metals [100]

Based on the equation for thermal stress development in a constrained structural member, the importance of the product of the elastic modulus and CTE is evident. The product of the elastic modulus and CTE for common polymers and metals is shown in Figure 74, where it is evident that – under the same constraints and temperature change – metals develop higher thermal stresses. However, the higher strength of metals partially offsets concern about these materials.

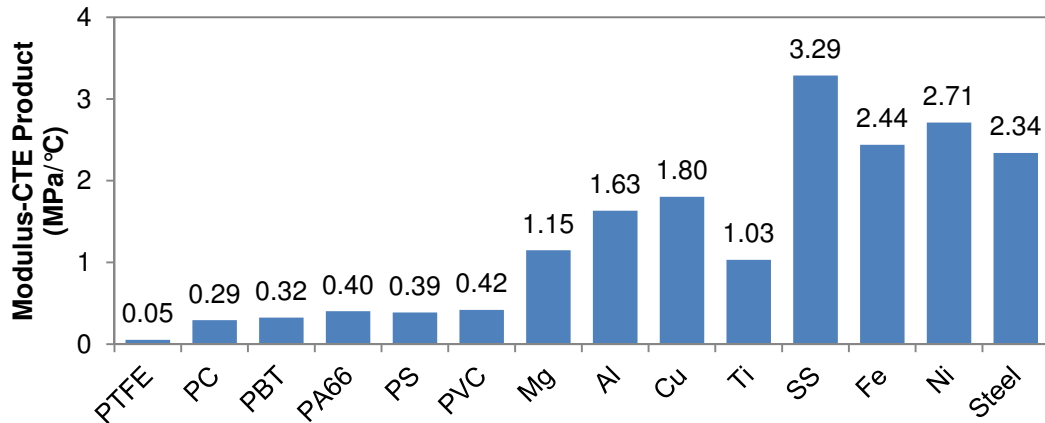


Figure 74: Modulus-CTE product of polymers and metals [100]

Although the modulus-CTE product is higher in metals than in polymers, the yield stress of metals is generally higher. As such, a normalized modulus-CTE product provides a fairer comparison of materials. Taking the inverse of the normalized modulus-CTE product provides the temperature change that a constrained rod made of that material can survive before yielding. This estimate is limited in scope in that it assumes that material properties are constant and deformation is linear during the temperature change, which is untrue over large temperature changes. Nonetheless, the inverse normalized modulus-CTE product provides a first order comparison among materials. Figure 75 provides the yield strength and inverse normalized modulus-CTE product of common polymers and metals.

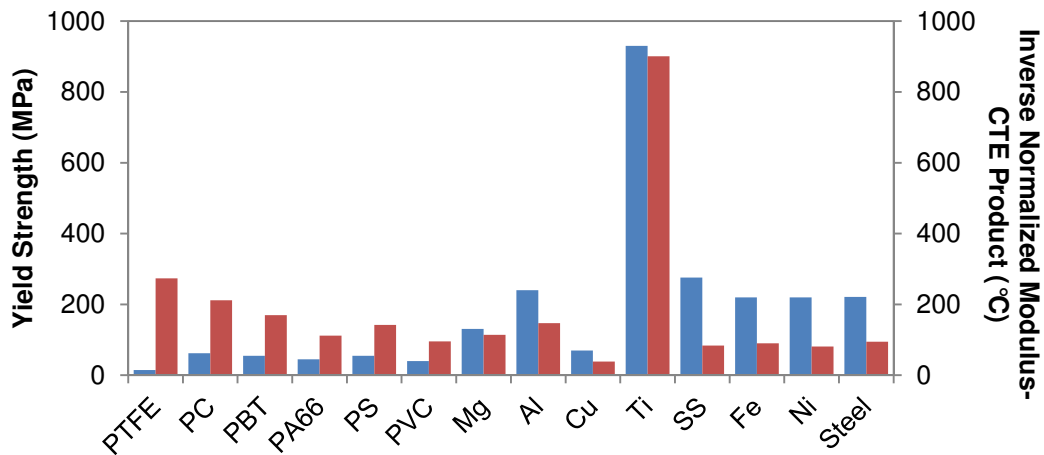


Figure 75: Yield strength and inverse normalized modulus-CTE product of polymers and metals [16] [100]

Figure 75 reveals that, in general, the inverse normalized modulus-CTE product is higher for polymers than for metals. This conclusion is limited in scope because the mechanical properties of polymers degrade at much lower temperatures than in metals. The higher yield strength of metals reveals that metals are more competitive with polymers using this metric rather than the modulus-CTE product

alone. The most notable result from Figure 75 is that titanium can, under the assumptions of this metric, undergo 900°C of temperature change in a constrained rod before yielding. The extraordinary yield strength of titanium (930 MPa) accounts for the performance in this metric. Although the high yield strength of titanium is desirable in some applications, such a large yield strength could indicate that titanium is being underutilized in the applications study in this section. Titanium is expensive and energy intensive and thus, its excellent yield strength may indicate that it is more useful to implement this material in applications requiring much higher strength materials. The geometry of a titanium heat exchanger could be optimized so that the stress magnitudes approach the yield stress, which could be achieved by using thinner fins and plates. The limit of this approach would be based on manufacturing, as only low-cost high-volume manufacturing methods are cost- and energy-effective in regard to seawater heat exchangers.

Thermal stress development in anisotropic composite materials is of particular concern – especially in injection molded specimens – where both local and global anisotropy can increase stress magnitudes. The composite material of present interest demonstrates transversely isotropic materials, with modest modulus (18.5 GPa) and low CTE (1.98 $\mu\text{m}/\text{m}/^\circ\text{C}$) longitudinal to the fibers and low modulus (3.2 GPa), and high CTE (122 $\mu\text{m}/\text{m}/^\circ\text{C}$) transverse to the fibers. Thus, the modulus-CTE product in the longitudinal to the fiber direction is a very low 0.0366 MPa/°C and the modulus-CTE product in the transverse to the fiber direction is 0.3904 MPa/°C. The modulus-CTE product differs by more than an order of magnitude, which could result in stress development within individual components (i.e., fins and plates), as well as at the

junction between fins and plates, which have different flow orientations and thus, different direction material properties.

Operating Conditions

Structural analysis was performed under combined pressure and convection loading to assess the effects of anisotropic thermomechanical properties on the stress distributions in the heat exchanger. Analysis was completed using a water flowrate of 20 cm³/s, inlet temperature of 15°C and pressure of 500 kPa. The air flowrate was 3000 cm³/s, the pressure was 500 kPa or 5000 kPa and the inlet temperature was 50°C or 150°C. The baseline (zero-stress) state of the heat exchanger was set at 25°C.

Results

Composite Polyamide 12

Maximum Stress Magnitudes

The stress magnitudes that developed from combined thermomechanical loading of the composite PA12 are shown in Figure 12. The results reveal that the stress levels do not exceed the expected yield strength of the polymer composite in either the longitudinal or transverse to the fiber directions for the loading conditions with an air inlet temperature of 50°C or without convection effects. The thermal stress development at high temperatures leads to very high stresses that exceed the yield strength of the composite. For reference, the longitudinal to the fiber yield strength was experimentally determined to be 91.5 MPa.

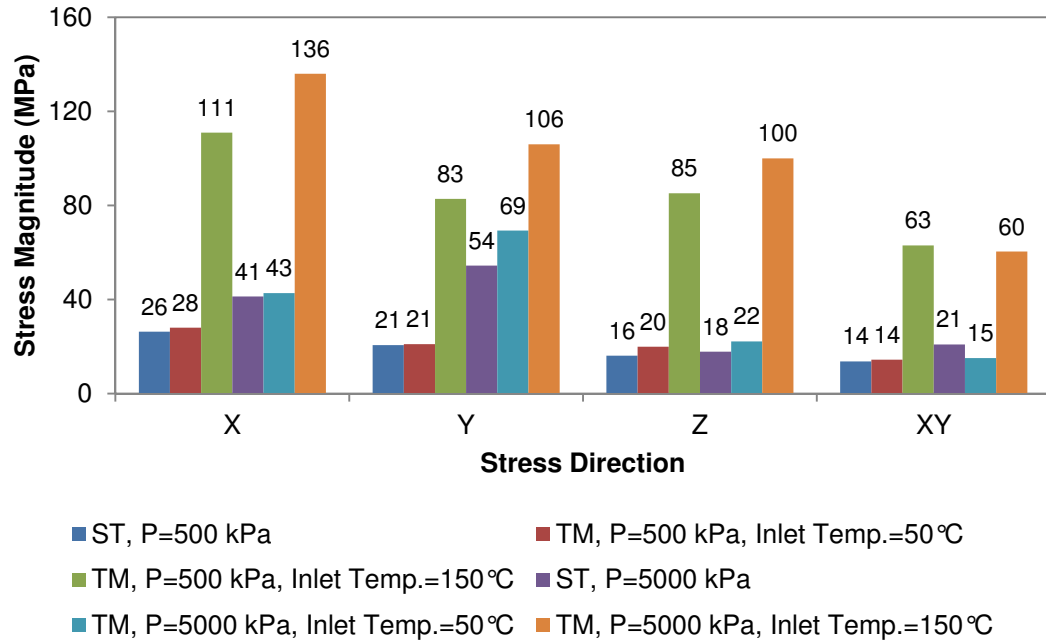


Figure 76: Maximum stress development from thermomechanical loading of PCHX (ST: structural only loading. TM: thermomechanical loading)

The results show that anisotropic materials, such as injection-molded fiber-reinforced polymers, are sensitive to the disparity in thermomechanical properties that occurs at the juncture between component sections with different fiber orientations, such as the juncture between the fins and the plates of the PCHX. This result is evident in the large stress magnitudes for the combined loading scenarios when the inlet air temperature was 150°C. The stresses that developed from application of pressure loads only and from the combined application of pressure loads and convection from air with a modest inlet temperature of 50°C were much smaller in magnitude than those that developed from the combined application of pressure loads and convection from air with an inlet temperature of 150°C. For example, in the y-direction, when the air pressure was 500 kPa, the increase in stress magnitude relative to structural only loading for combined loading with an inlet temperature of 50°C was 1.9%; the increase was 302% for an inlet temperature of 150°C. Similar results are

seen in the x-, z- and xy- maximum stress magnitudes, where the increase over the structural only results for the 150°C combined loading results (with $P_{air} = 500 \text{ kPa}$) was 322%, 429% and 460%, respectively. The increases in x-, z- and xy- stress magnitude relative to the structural only results for the 50°C combined loading (with $P_{air} = 500 \text{ kPa}$) results was only 6.5%, 24% and 5.1%, respectively

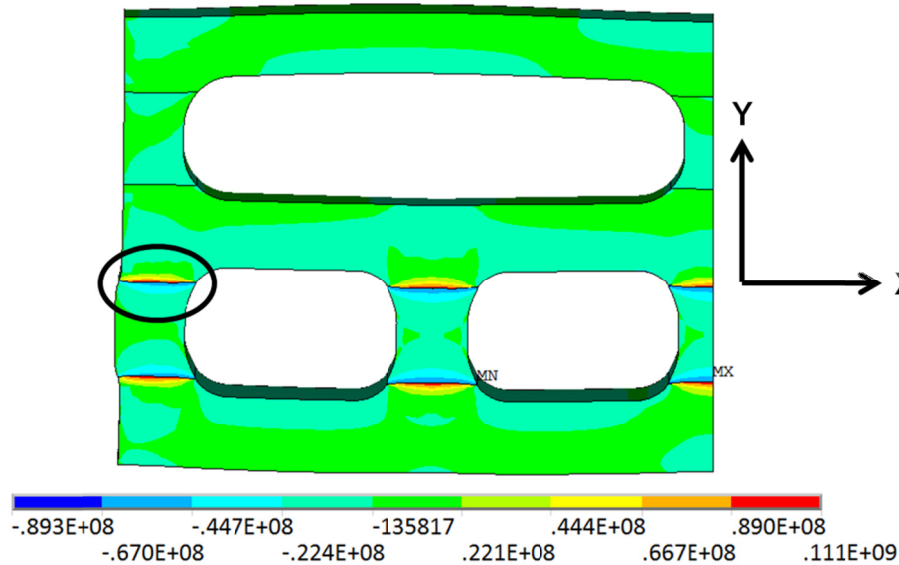


Figure 77: Y-direction stresses under combined loading for an airside pressure of 0.5 MPa and air inlet temperature of 150°C (units: Pa)

Relative to the stress magnitudes seen in the 150°C airside inlet temperature scenarios, the increase in airside pressure from 500 kPa to 5000 kPa had modest effects on stress development. The biggest discrepancy in stress magnitude occurred in the x- and y-directions, where stresses increased 57% and 164%, respectively. Nonetheless, the structural only y-direction stress magnitude for an airside pressure of 5000 kPa was only 51% of the y-direction stress magnitude for combined loading with an airside pressure of 5000 kPa and inlet temperature of 150°C.

Please note that the current model provides the most extreme anisotropy for the current geometry. Injection molding of PCHXs will generate gradual transitions in

material properties as the flow front advances through the mold cavity, which means that the stress development at the juncture between fins and plants will be less significant. Regardless, the discontinuous thermomechanical properties must be carefully considered to ensure that stress development between adjacent regions with significantly different fiber orientations does not cause failure of PCHXs.

Maximum Stress Locations

The naming convention shown in Figure 78 and Figure 79 is utilized to describe the locations of the maximum stress magnitude locations in the PCHX and titanium HX. ASL stands for airside left, ASR stands for airside right and WS stands for waterside. The fillet radii are numbered 1-4 clockwise around the channel beginning in the lower left corner. The front face is the hot air inlet and the rear face is the cooled air outlet.

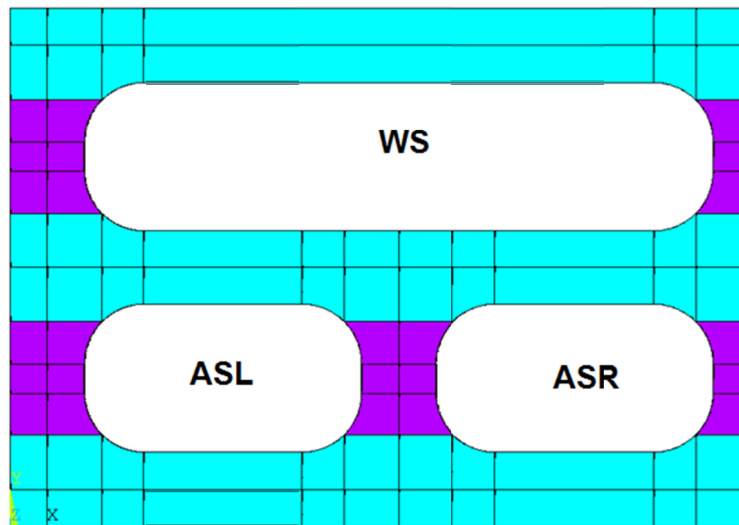


Figure 78: Naming convention for channels in HX

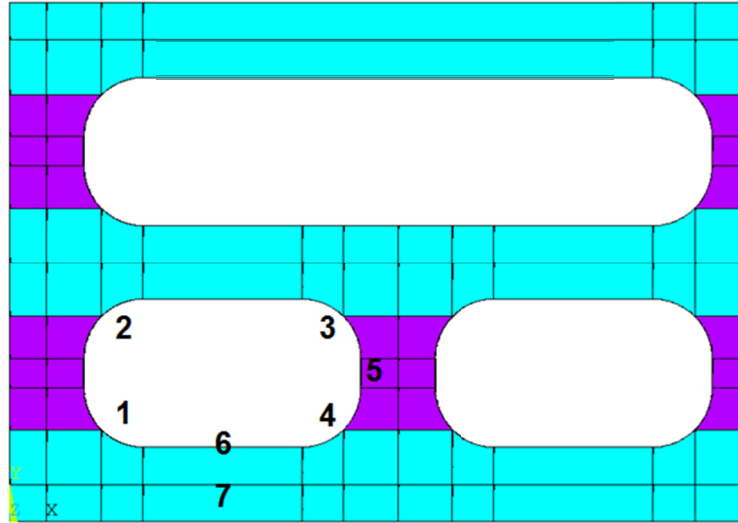


Figure 79: Naming convention for channel fillets

The location of the maximum directional stress magnitudes varied widely with the various loading conditions imposed on the PCHX. The location of the maximum stress magnitudes and how the locations change as a function of loading conditions informs the determination of the dominant load (i.e., pressure or thermal). The addition of thermal loading also changed the location of stresses with respect to their depth along the HX (i.e., location in the z-direction) because of the temperature gradients that occur in this direction as the air cools and water warms. The directional stresses were nearly independent of depth in the structural only loading conditions. Table 16 shows the locations of the maximum directional stresses as a function of airside pressure and air inlet temperature in the PCHX.

Table 16: Location of maximum stresses in PCHX exposed to combined loading

Air Inlet Condition	X	Y	Z	XY
0.5 MPa	WS 3	WS 2	WS 2	WS 2
0.5 MPa, 50°C	ASR 4 F	ASL 2 F	ASR 1 F	ASR 1 F
0.5 MPa, 150°C	ASR 4 F	ASL 2 F	ASR 1 F	ASR 1 F
5.0 MPa	ASR 4	ASL 1	ASL 1	ASR 4
5.0 MPa, 50°C	ASL 7 R	ASL 1 R	ASR 1 F	ASL 1 R
5.0 MPa, 150°C	ASR 4 F	ASR 5 F	ASR 1 F	ASR 3 F

At the lower airside pressure of 0.5 MPa, in both cases of thermal loading (i.e., inlet temperatures of 50 and 150°C), the locations of the maximum directional stresses changed to the same locations, none of which agreed with the locations of the maximum directional stresses in the studies where pressures of 0.5 MPa were applied. This result indicates that the application of the thermal load, even at low input temperatures, significantly alters the stress distribution. This result might have occurred because the lower applied pressures do not lead to high stress development in the PCHX.

For the studies with an airside pressure of 5.0 MPa, both the applied pressure and the temperature play important roles in stress development. Relative to the study without thermal loading, the addition of thermal loading with an air inlet temperature of 50°C changes the location of the maximum directional stresses with the exception of the maximum y-stress. The relocation of the maximum x-stress from the bottom of the left air channel to the junction between the fins and plate at the bottom middle of the HX indicates that the temperature loading has generated additional stress at the junction between sections with different mechanical properties. Increasing the air inlet temperature to 150°C reveals the significance of this load, as the locations of the maximum y- and z-directional stresses changed again. The anisotropy in the HX as well as the boundary condition in the z-direction likely caused the change in maximum stress location.

Titanium

Maximum Stress Magnitudes

Structural analysis was completed for a titanium heat exchanger subjected to combined thermomechanical loading to assess the effect of anisotropy on stress

development. Titanium was chosen – relative to other corrosion resistant heat exchanger materials such as PTFE – because titanium is more likely to be used in high-pressure high-temperature applications due to the softening and deformation that could occur in PTFE under these operating conditions.

Figure 80 provides a comparison of the stresses resulting from the application of structural and thermomechanical loads to the titanium heat exchanger. The results reveal that isotropic materials such as titanium distribute stresses more uniformly than fiber-reinforced polymers whose mechanical properties are a function of fiber orientation. Although the direction stress distribution differs between the polymer composite and titanium, the general trends in stress magnitude are similar. The stresses resulting from the application of only pressure loads and combined loading with an air inlet temperature of 50°C are much smaller than those seen when the HX is exposed to combined loading with an air inlet temperature of 150°C. For example, when for structural only loading with an airside pressure of 5.0 MPa, the maximum x-stress is 28.5 MPa; this value increases 32% for combined loading with a 50°C air inlet temperature but increases 158% for combined loading with a 150°C air inlet temperature; Similar trends are seen in the y- and xy-direction stresses.

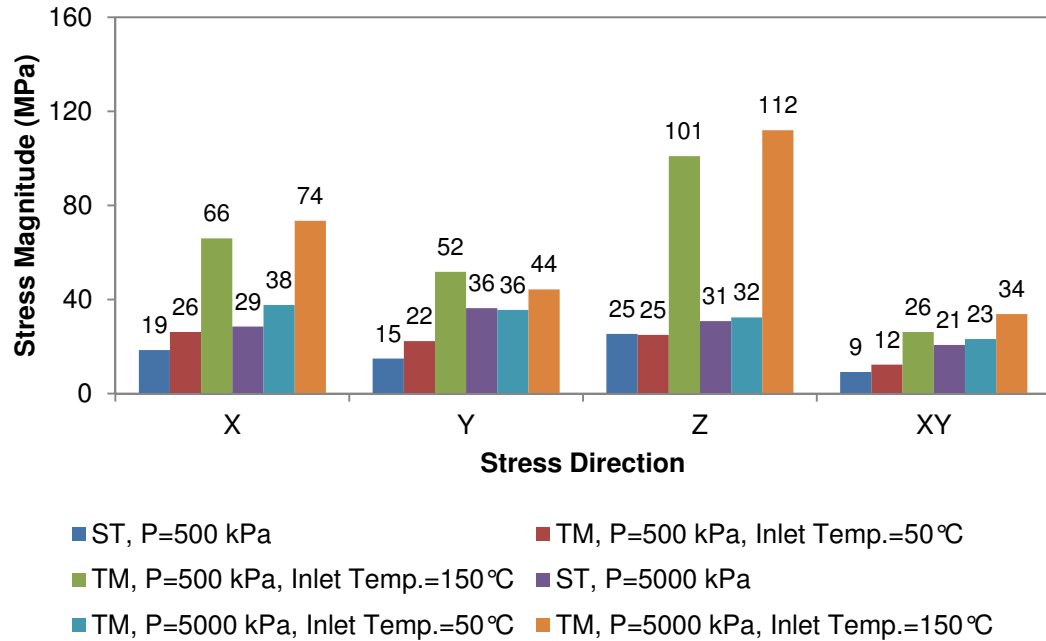
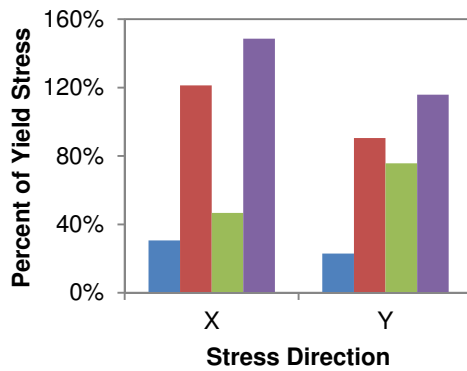


Figure 80: Maximum stress development from thermomechanical loading of titanium HX (ST: structural only loading. TM: thermomechanical loading)

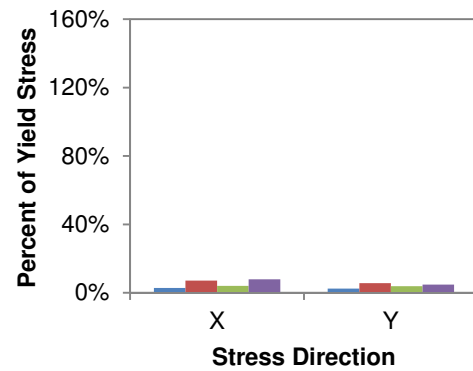
The effect of the inlet temperature on stress development is most pronounced in the z-direction stresses where the maximum stress increases 304% from the structural only loading with an airside pressure of 5.0 MPa to the combined loading with the same airside pressure and air inlet temperature of 150°C. This stress development is due to two reasons: the boundary conditions that prevent any displacement of the front and rear faces of the heat exchanger and the relatively high modulus-CTE product of titanium (1.03 MPa/°C). For comparison with the PCHX, the modulus-CTE product in the longitudinal to the fiber direction is a very low 0.0366 MPa/°C and the modulus-CTE product in the transverse to the fiber direction is 0.3904 MPa/°C. It is noteworthy that the boundary conditions represent the most extreme displacement constraint and the manifolds could be designed to provide some displacement, which would alleviate the stress magnitudes in the z-direction. This change would also reduce the z-direction stress magnitude in the PCHX.

Figure 81 and Figure 82 show the x- and y-direction stresses normalized based on the yield strength of the polymer composite heat exchanger and titanium heat exchanger, respectively. The results reveal that – regardless of loading application – the maximum stress magnitudes are well below the expected yield stress of titanium (930 MPa). These results reveal that the titanium material is underutilized for these applications, and thus material substitution or geometric changes are required for better use of the material. However, titanium is energy intensive, costly and more difficult to manufacture than polymer composites, which could mean that polymer composites are a more practical material choice for these loading conditions. The easier to manufacture and less energy intensive polymer composite experiences stresses that exceed its yield strength in the high temperature applications but the stress levels for the moderate air inlet temperature of 50°C are within the acceptable range for the material. Thus, such an application appears to be a practical implementation of the polymer composite material from a structural standpoint.



- TM, P=500 kPa, Inlet Temp.=50°C
- TM, P=500 kPa, Inlet Temp.=150°C
- TM, P=5000 kPa, Inlet Temp.=50°C
- TM, P=5000 kPa, Inlet Temp.=150°C

Figure 81: Normalized stresses in polymer composite heat exchanger



- TM, P=500 kPa, Inlet Temp.=50°C
- TM, P=500 kPa, Inlet Temp.=150°C
- TM, P=5000 kPa, Inlet Temp.=50°C
- TM, P=5000 kPa, Inlet Temp.=150°C

Figure 82: Normalized stresses in titanium heat exchanger

Maximum Stress Locations

As in the PCHX, the location of the maximum directional stress magnitudes varied widely with the various loading conditions imposed on the titanium HX. The addition of thermal loading contributed to additional stress development, but less so than in the PCHX because the temperature profile of the titanium HX showed less variation due to the isotropic and higher conductivity. Table 17 shows the locations of the maximum directional stresses as a function of airside pressure and air inlet temperature in the titanium HX.

Table 17: Location of maximum stresses in Ti HX exposed to combined loading

Air Inlet Condition	X	Y	Z	XY
0.5 MPa	WS 3	WS 2	WS 3	WS 2
0.5 MPa, 50°C	WS 3 R	WS 2 R	ASR 1 R	WS 2 F
0.5 MPa, 150°C	WS 4 R	WS 1 R	ASR 1 R	WS 4 R
5.0 MPa	ASR 4	ASL 1	ASL 1	ASR 4
5.0 MPa, 50°C	ASR 2 R	ASL 1 R	WS 3 R	ASR 2 R
5.0 MPa, 150°C	ASR 2 R	WS 1 R	ASL 6 R	ASR 2 R

For an airside pressure of 0.5 MPa, the addition of the thermal load with an airside inlet temperature of 50°C played an important role in the location of the z-direction stress, as the material experienced a compressive stress as it tried to expand due to the elevated temperature. The locations of the maximum x-, y- and xy-stresses were unchanged. Increasing the airside inlet temperature to 150°C led to significant changes in all of the maximum direction stress locations. The titanium HX experienced significantly higher stress in the z-direction, which led to larger stresses in the other directions and the material deformed to accommodate the higher temperatures and stress.

For an airside pressure of 5.0 MPa, the addition of the thermal load with an airside inlet temperature of 50°C led to changes in the location of the maximum x-

and xy-stress locations. It is reasonable that the maximum xy-direction stress location changed with the new location of the x-direction because of the relationship between these stresses and that the location of the maximum y-direction stress was unchanged. Under the same structural loading conditions with an airside inlet temperature of 150°C, the location of the maximum y- and z-direction stresses changed due to the higher compressive load resulting from the boundary conditions and increased temperature change.

Variation of Geometry

Purpose

The thickness of the fins and plates in the heat exchanger, which are uniformly sized, was varied in one case study to assess the effect of wall thickness on thermomechanical stress development in polymer composite heat exchangers. The directional thermomechanical stress was as high as 148% of the yield stress of the composite for the conditions studied. A similar study on the heat exchanger geometry was not performed for the titanium heat exchanger because the stresses seen in the titanium heat exchanger were approximately 10% of the yield stress.

Parameters

The operating conditions studied for the PCHX geometric variation were as follows: airside pressure of 5.0 MPa, air inlet temperature of 50°C and waterside pressure of 0.5 MPa. Of the operating conditions studied, these conditions represented conditions where the geometry is an important factor in stress development due to the high stress and the lower airside inlet temperature meant that thermal stress

development would not overshadow stress reductions resulting from increasing the plate thickness in the heat exchanger module.

The heat transfer characteristics of the fluid (i.e., local heat transfer coefficient and local fluid temperature) were not changed from the original analysis although, assuming constant flow rate, the velocity of the fluid would increase with increasing wall thickness and the wetted area and hydraulic diameter would decrease. The properties of the fluid were not changed because these properties affect the temperature distribution (and thus, thermal stress distribution) in the heat exchanger and would have limited the conclusions made regarding the effect of the plate thickness on stress development. By shaping the study without changing the convective properties, no discussion is provided regarding the effect of wall thickness on heat transfer rate. Based on one-dimensional conduction resistance and the low conductivity of the polymer composite, it is expected that the wall thickness is a significant contributor to the overall resistance of the heat exchanger. Nonetheless, more detailed variation of geometry could lead to a heat exchanger design that reduces the through wall thickness (and thus, conduction resistance) and increases the thickness in other areas to alleviate stress development.

Results

Figure 83 provides the maximum directional stresses as a function of fin and plate thickness for airside pressure of 5.0 MPa, air inlet temperature of 50°C and waterside pressure of 0.5 MPa. The thickness was varied from 1.5 to 4.5 mm in 0.5 mm increments; note that the baseline for previous results has been 2.5 mm.

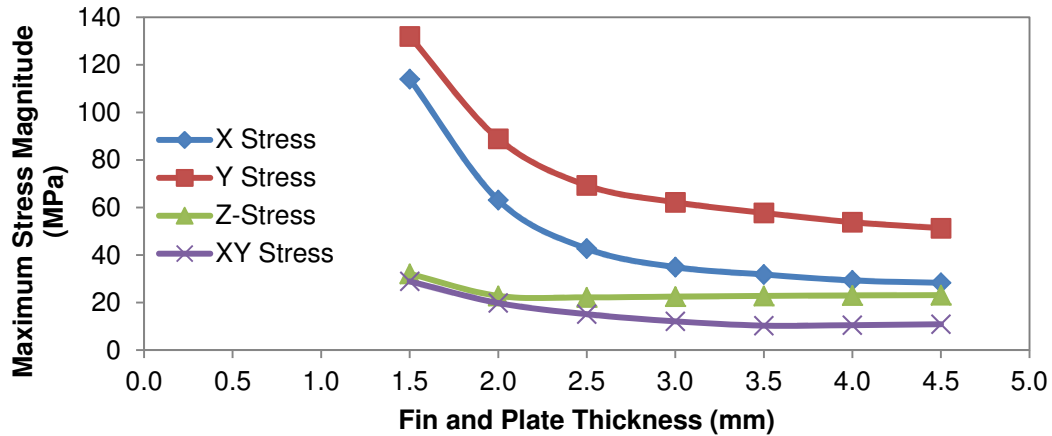


Figure 83: Maximum directional stress magnitude as a function of fin and plate thickness

The results reveal that the fin and plate thickness significantly affect maximum directional stress magnitudes. The relative decreases in stress development decrease with increasing plate thickness. For example, in the x-direction, increasing the thickness from 1.5 mm to 2.0 mm decreases the stress 45%; increasing the thickness from 4.0 to 4.5 mm decreases the stress only 3%. A similar trend is seen for the y-, z- and xy-directional stress magnitudes. The results indicate that the assumed thickness for the present study (2.5 mm) provides a balance between high stress levels and higher mass of the heat exchanger.

Discussion

The diminishing reduction in stress magnitude indicates the importance of the thermal stress development in the anisotropic polymer composite heat exchanger. After the thickness has reached a certain level, very little reductions can be achieved in maximum stress magnitude. In general, increasing the thickness should continue to reduce the stress magnitude. However, in the present analysis, the thermomechanical stress begins to dominate the stress development and further increases in thickness

fail to reduce stress magnitude. This result is most evident in the z-direction, which is most sensitive to thermal stress development because of the boundary conditions that prevent displacement at the inlet or outlet of the heat exchanger. In the z-direction, a 29% reduction in stress is achieved by increasing the thickness from 1.5 mm to 2.0 mm; beyond 2.0 mm, there is negligible variation in the stress magnitude because the axial thermal stress development is independent of loading area. Thus, increasing the thickness from 2.5 to 2.0 mm reduces the stress from the pressure loading but additional increases cannot reduce the stress, which is only a function of thermal expansion and temperature profile.

Summary of Findings

Combined thermomechanical loading of an anisotropic PCHX and an isotropic polymer HX were studied using a finite element model. The results revealed the importance of the thermal loading in both the maximum directional stress magnitude and the location of the maximum directional stress. In the PCHX, the location of the maximum directional stress magnitudes changed when the thermal load was applied and the higher stress magnitudes seen for an air inlet temperature of 150°C shared the same locations regardless of airside pressure, indicating that thermal stress dominated the stress magnitude and distribution for these conditions. In the PCHX, the maximum stress magnitudes of 83-136 MPa occurred in the x-, y- and z-directions when the HX was exposed to an air inlet temperature of 150°C. These stresses approached or exceeded the yield stress of the polymer composite, which was 91.5 MPa. In the titanium HX, the maximum stress magnitudes of 101 and 112 MPa occurred in the z-direction when the air inlet temperature was 150°C and the airside

pressure was 0.5 and 5.0 MPa, respectively. The z-direction stresses were the highest stresses seen in the titanium HX, which was the result of the higher modulus-CTE product of titanium and the boundary conditions of the problem. Nonetheless, the titanium heat exchanger was well below its yield stress of 930 MPa. In general, it appears that combined loading led to the most significant changes in maximum direction stress location and magnitude when the air inlet temperature was high. These loading conditions are of particular importance due to the change in mechanical properties that tends to occur in polymers and their composites at elevated temperatures. At modest air temperatures, the stress distributions showed little change resulting from the addition of the thermal loads.

A case study on the effect of heat exchanger wall thickness on thermomechanical stress development was performed. The results revealed that increasing the wall thickness could reduce the stress development resulting from pressure loading. However, the thermal stress development resulting from the boundary conditions and anisotropy could not be reduced because these stresses are nearly independent of geometry.

Chapter 8: Summary of Findings and Contributions and Path to Commercialization

Summary of Findings and Contributions

Hygrothermal Aging Studies

The hygrothermal effect on raw and fiber-reinforced polymers was studied over a range of applicable water temperatures and salinities; the effect of salinity on hygrothermal aging had not been studied previously. These studies contributed an understanding of the change in mechanical properties resulting from the hygrothermal effect in hygroscopic polymers and their composites. The results revealed that composite PA12 absorbed less moisture than raw PA12, which was attributed to the addition of the carbon fibers and their role to constrain the free volume and increase the crystallinity of the matrix. Water salinity and temperature did not affect equilibrium moisture content.

The study found that hygrothermal aging led to a reduction in elastic modulus and strength and increased ductility in raw and reinforced PA12, consistent with a decrease in crystallinity, and the effect of hygrothermal aging was more pronounced in the raw polymer. Mechanical properties exhibited excellent recovery after redrying of aged specimens, which indicated that the hygrothermal effect was primarily physical in nature. Permanent changes in mechanical properties resulting from hydrolysis, debonding and microcavity formation was minimal. In both aged and redried specimens, higher temperatures generally led to greater changes in mechanical properties but salinity did not affect retention or recovery of baseline properties. Thus, the scientific contribution of this work was to provide additional

evidence that attributes the hygrothermal aging to changes in crystallinity of the polymer matrix.

Mechanical Modeling

The technical contribution of this portion of the research effort was to develop a mechanical finite element model to assess the stress development in corrosion-resistant polymer, polymer composite and metallic heat exchangers subjected to pressure loading. The pressure loads represent a broad range of gas-to-liquid heat exchanger applications. The mechanical modeling found that transversely isotropic material systems developed higher stresses in those directions with most enhanced properties due to longitudinal fiber orientation. Although the directions with preferential fiber alignment were subjected to higher stresses, the fiber orientation means that the stiffness and strength in these directions is highest, leading to reduced deformation and reduced likelihood of plastic deformation. Isotropic materials exhibited greater uniformity among maximum directional stress magnitudes. The less stiff raw polymer material exhibited significant deformation at high pressure and the very stiff metal exhibited little deformation, even at high pressures (5.0 MPa).

Thermal Modeling

In this portion of the research effort, the technical contribution was to develop a thermal finite element model, adapted from the previous mechanical model, which was experimentally verified via comparison with the heat transfer rate of an identical laboratory heat exchanger apparatus. The numerical and experimental heat transfer rates agreed within experimental uncertainty and thus, the numerical model was subjected to a diverse range of fluid conditions. At fluid pressures near ambient, the

airside convective resistance dominated, which meant that improving material thermal conductivity had little effect on heat transfer rate. However, as the fluid pressure increased and the airside convective resistance diminished, the effect of the through wall thermal conductivity became more dominant and led to the titanium HX significantly outperforming the PCHX. At elevated airside pressures, the PCHX significantly outperformed the raw PHX. The present modeling revealed the importance of improving the through wall conductivity by improving fiber orientation in the through wall direction. Such an orientation could be achieved by using sacrificial features in the injection-molding process or using an alternative low-cost, high-volume manufacturing process (e.g., extrusion).

Thermomechanical Modeling

A final contribution of this research effort was to develop a thermomechanical model to quantify the significance of anisotropy in material properties on stress development in a prototype polymer composite heat exchanger subjected to simultaneous thermal and mechanical loading. Thermomechanical modeling revealed the significance of combined loading on stress development in PCHX prone to local and global anisotropy in thermomechanical properties. As in the mechanical modeling results, the maximum stresses occurred in the directions with longitudinal to the fiber properties. Unlike the mechanical modeling results, anisotropy within features (e.g., fins and plates) and between adjacent features led to significant additional stress development beyond the stress magnitudes generally seen in isotropic materials. The modeling results revealed the importance of mold designs that incorporate gradual transitions in fiber orientation, which directly affects

thermomechanical properties. The lower modulus-CTE product in fiber-reinforced polymer composites could be useful in applications that require the heat exchanger to be tightly constrained. In metals, the modulus-CTE product is often higher, which results in higher stresses in those directions subjected to boundary constraints. A brief case study on the effect of wall thickness on stress development confirmed that pressure loading was sensitive to geometry and thus stress development from such loading was reduced with increasing thickness, but thermal stress development, which was more sensitive to boundary conditions and anisotropy, could not be reducing by increasing the wall thickness.

Path to Commercialization

Large Scale Demonstration

The present study focused on the validation and modeling of a laboratory scale heat exchanger capable of transferring only tens of Watts. A larger heat exchanger capable of transferring hundreds to thousands of Watts would represent a much more practical heat exchanger and could serve to validate the improvement in heat transfer performance resulting from the use of polymer composites. A finned-tube heat exchanger capable of transferring hundreds of Watts is currently being installed in the laboratory.

Full Anisotropic Modeling

The modeling presented in this thesis assumed transversely isotropic thermomechanical properties based on fiber orientation. This modeling represented the worst-case scenario in terms of heat transfer rate and structural anisotropy. A full anisotropic model based on the microstructure resulting from the injection molding of

finned plates would provide more realistic thermomechanical properties and could reduce stress concentrations and improve heat transfer rate of the polymer composite heat exchanger. A full anisotropic model would require the use of commercially available mold filling software (e.g., Moldflow). The thermomechanical properties based on the fiber orientation resulting from injection molding must be input directly into the finite element modeling software to achieve full anisotropic modeling.

Evaluation of Hygrothermal Effects on Thermal Properties

The hygrothermal aging studies conducted for this thesis were limited in scope to the change in mechanical properties a function of aging conditions. A similar analysis must be completed to assess the change in thermal properties resulting from hygrothermal aging. It is expected that the thermal conductivity of the composite will improve slightly because the thermal conductivity of water is higher than that of the polymer matrix. Hygrothermal aging may affect the coefficient of thermal expansion of the polymer composite; this change is especially important as the coefficient of thermal expansion relates thermal gradients to stress development.

Assessment of Biofouling and Scaling

One potential benefit resulting from the use of polymer composites in heat exchangers is reduced biofouling and scaling. At present, the literature suggests that polymers experience less scaling due to their reduced surface energy and smooth surfaces but biofouling and scaling of polymer composites must be studied to ensure polymer composites are less susceptible to these activities. The reduction in surface fouling – if verified – would reduce the fouling resistance for polymer composite heat

exchangers and thus, their heat transfer performance would be more competitive with the performance of metallic heat exchangers.

Geometric Optimization of Polymer Composite Heat Exchanger

A rigorous optimization study of the heat exchanger geometry could lead to much lower stress development, improved heat transfer rates and lower mass (and embodied energy) designs. Such an optimization would require many simulations to determine the regions of the heat exchanger that benefit most of geometric changes. Furthermore, new geometries, such as finned tubes, could be studied to determine the thermomechanical benefits resulting from such changes. Fortunately, due to manufacturing processes available to polymer composites, the geometry can be more complex than the geometry of a conventional metallic heat exchanger without significantly affecting cost or manufacturing time.

Appendix 1: ANSYS Code

```
!*****Start Commands and Tolerance Setting
/clear,nostart
/prep7
antype,static
ccc=1e-6
!*****Pressure Setpoints
pres_gs=5e6
pres_ws=0.5e6
!*****Mesh Control
n_div=5
spacing_ratio=15
xy_mesh_size=.0002
z_mesh_size=.002
!*****Material Properties (1:plates, 2:fins)
MP,REFT,1,20
MP,EX,1,18.46e9
MP,EY,1,3.18e9
MP,EZ,1,3.18e9
MP,PRXY,1,.3394
MP,PRYZ,1,.5131
MP,PRXZ,1,.3394
MP,GXY,1,1.0125e9
MP,GYZ,1,1.0503e9
MP,GXZ,1,1.0125e9
MP,KXX,1,9.25
MP,KYY,1,0.734
MP,KZZ,1,0.734
MP,ALPX,1,1.98e-6
MP,ALPY,1,1.22e-4
MP,ALPZ,1,1.22e-4
MP,DENS,1,1610
MP,REFT,2,20
MP,EX,2,3.18e9
MP,EY,2,18.46e9
MP,EZ,2,3.18e9
MP,PRXY,2,.0584
MP,PRYZ,2,.3394
MP,PRXZ,2,.5131
MP,GXY,2,1.0125e9
MP,GYZ,2,1.0125e9
MP,GXZ,2,1.0503e9
MP,KXX,2,0.734
```

```

MP,KYY,2,9.25
MP,KZZ,2,0.734
MP,ALPX,2,1.22e-4
MP,ALPY,2,1.98e-6
MP,ALPZ,2,1.22e-4
MP,DENS,2,1610
!*****Element Definition
et,1,solid226,11
!*****Geometric Parameters
W=.05
D=.05
height_fin_ws=.005
height_fin_gs=.005
n_fin_ws=3
n_fin_gs=5
t_fin_ws=.0025
t_fin_gs=.0025
t_plate=.0025
r_fillet=.002
S_ws=(W-(n_fin_ws*t_fin_ws))/(n_fin_ws-1)
S_gs=(W-(n_fin_gs*t_fin_gs))/(n_fin_gs-1)
!*****Dimension Creation
nxx=100
nyy=100
nzz=100
*dim,xx,,nxx
*dim,yy,,nyy
*dim,zz,,nzz
xx(1)=0
xx(2)=t_fin_gs
xx(3)=xx(2)+r_fillet
xx(4)=xx(2)+S_gs-r_fillet
xx(5)=xx(2)+S_gs
xx(6)=t_fin_ws
xx(7)=xx(6)+r_fillet
xx(8)=xx(6)+S_ws-r_fillet
xx(9)=xx(6)+S_ws
xx(10)=W
yy(1)=0
yy(2)=t_plate
yy(3)=yy(2)+r_fillet
yy(4)=yy(2)+height_fin_gs-r_fillet
yy(5)=yy(2)+height_fin_gs
yy(6)=yy(5)+t_plate
yy(7)=yy(6)+r_fillet
yy(8)=yy(6)+height_fin_ws-r_fillet

```

```

yy(9)=yy(6)+height_fin_ws
yy(10)=yy(9)+t_plate
zz(1)=0
zz(2)=D
!*****Initial Block Creation
blc4,xx(1),yy(1),xx(10),yy(10),zz(2)
!*****Channel Creation
blc4,xx(3),yy(2),S_gs-2*r_fillet,height_fin_gs,zz(2)
blc4,xx(2),yy(3),S_gs,height_fin_gs-2*r_fillet,zz(2)
cyl4,xx(3),yy(3),r_fillet,,,zz(2)
cyl4,xx(3),yy(4),r_fillet,,,zz(2)
cyl4,xx(4),yy(3),r_fillet,,,zz(2)
cyl4,xx(4),yy(4),r_fillet,,,zz(2)
vsel,s,loc,x,xx(2)-ccc,xx(5)+ccc
vgen,n_fin_gs-1,all,,,xx(5)
blc4,t_fin_ws+r_fillet,t_plate*2+height_fin_gs,S_ws-2*r_fillet,height_fin_ws,zz(2)
blc4,t_fin_ws,t_plate+height_fin_gs+t_plate+r_fillet,S_ws,height_fin_ws-
2*r_fillet,zz(2)
cyl4,xx(7),yy(7),r_fillet,,,zz(2)
cyl4,xx(7),yy(8),r_fillet,,,zz(2)
cyl4,xx(8),yy(7),r_fillet,,,zz(2)
cyl4,xx(8),yy(8),r_fillet,,,zz(2)
vsel,s,loc,y,yy(6)-ccc,yy(9)+ccc
vgen,n_fin_ws-1,all,,,xx(9)
!*****Removal of Channel Geometry from Initial Block
vsel,all
vsbv,1,2,,delete,delete
numcmp,volu
*do,i,1,(n_fin_gs+n_fin_ws-2)*6-1,1
vol_num=(n_fin_gs+n_fin_ws-2)*6+1-i
vsel,all
vsbv,vol_num,1,,delete,delete
numcmp,volu
*enddo
numcmp,area
!*****Removal of Half of Geometry for Half Symmetry
Constraint
blc4,xx(10)/2,yy(1),xx(10)/2,yy(10),zz(2)
vovlap,all
vsel,s,loc,x,xx(10)/2-ccc,xx(10)+ccc
vdele,all,,,1
vsel,all
vplot
numcmp,volu
numcmp,area
!*****Vertical Separation of Gas Side Volumes

```

```

wpave,0,yy(2)/2,0
wprota,,90
vsbw,1
numcmp,volu
wpave,0,yy(3)-(1/sqrt(2))*r_fillet,0
vsbw,all,delete
wpave,0,yy(3),0
vsel,s,loc,y,yy(3)-ccc,yy(10)+ccc
vsbw,all,delete
wpave,0,yy(4),0
vsel,s,loc,y,yy(4)-ccc,yy(10)+ccc
vsbw,all,delete
wpave,0,yy(4)+(1/sqrt(2))*r_fillet,0
vsel,s,loc,y,yy(4)+(1/sqrt(2))*r_fillet-ccc,yy(10)+ccc
vsbw,all,delete
wpave,0,yy(10)/2,0
vsel,s,loc,y,yy(10)/2-ccc,yy(10)+ccc
vsbw,all,delete
!*****Vertical Separation of Water Side Volumes
wpave,0,yy(7)-(1/sqrt(2))*r_fillet,0
vsel,s,loc,y,yy(7)-(1/sqrt(2))*r_fillet-ccc,yy(10)+ccc
vsbw,all,delete
wpave,0,yy(7),0
vsel,s,loc,y,yy(7)-ccc,yy(10)+ccc
vsbw,all,delete
wpave,0,yy(8),0
vsel,s,loc,y,yy(8)-ccc,yy(10)+ccc
vsbw,all,delete
wpave,0,yy(8)+(1/sqrt(2))*r_fillet,0
vsel,s,loc,y,yy(8)+(1/sqrt(2))*r_fillet-ccc,yy(10)+ccc
vsbw,all
wpave,0,(yy(9)+yy(10))/2,0
vsel,s,loc,y,yy(8)+(1/sqrt(2))*r_fillet-ccc,yy(10)+ccc
vsbw,all
!*****Horizontal Separation of Gas Side Volumes
wprota,,90
wpave,(xx(1)+xx(2))/2,0,0
vsel,s,loc,y,0-ccc,yy(7)-(1/sqrt(2))*r_fillet+ccc
vsbw,all,delete
wpave,xx(3)-(1/sqrt(2))*r_fillet,0,0
vsel,s,loc,y,0-ccc,yy(7)-(1/sqrt(2))*r_fillet+ccc
vsbw,all,delete
wpave,xx(3),0,0
vsel,s,loc,y,0-ccc,yy(7)-(1/sqrt(2))*r_fillet+ccc
vsbw,all,delete
wpave,xx(4),0,0

```

```

vsel,s,loc,y,0-ccc,yy(7)-(1/sqrt(2))*r_fillet+ccc
vsbw,all,delete
wpave,xx(4)+(1/sqrt(2))*r_fillet,0,0
vsel,s,loc,y,0-ccc,yy(7)-(1/sqrt(2))*r_fillet+ccc
vsbw,all,delete
*do,i,1,n_fin_gs/2-1,1
wpoffs,0,0,xx(2)+2*(r_fillet-(1/sqrt(2))*r_fillet)
vsel,s,loc,y,0-ccc,yy(7)-(1/sqrt(2))*r_fillet+ccc
vsbw,all,delete
wpoffs,0,0,r_fillet/sqrt(2)
vsel,s,loc,y,0-ccc,yy(7)-(1/sqrt(2))*r_fillet+ccc
vsbw,all,delete
wpoffs,0,0,S_gs-2*r_fillet
vsel,s,loc,y,0-ccc,yy(7)-(1/sqrt(2))*r_fillet+ccc
vsbw,all,delete
wpoffs,0,0,r_fillet/sqrt(2)
vsel,s,loc,y,0-ccc,yy(7)-(1/sqrt(2))*r_fillet+ccc
vsbw,all,delete
!wpoffs,0,0,xx(2)/2+r_fillet-(1/sqrt(2))*r_fillet
vsel,s,loc,y,0-ccc,yy(7)-(1/sqrt(2))*r_fillet+ccc
!vsbw,all,delete
*enddo
wpave,xx(2)/2,0,0
*do,i,1,n_fin_gs/2-1,1
wpoffs,0,0,xx(2)*1+S_gs
vsel,s,loc,y,0-ccc,yy(6)+ccc
vsbw,all,delete
*enddo
!*****Horizontal Separation of Water Side Volumes
wpave,(xx(1)+xx(6))/2,0,0
vsel,s,loc,y,yy(4)+(1/sqrt(2))*r_fillet-ccc,yy(10)+ccc
vsbw,all,delete
wpave,xx(7)-(1/sqrt(2))*r_fillet,0,0
vsel,s,loc,y,yy(4)+(1/sqrt(2))*r_fillet-ccc,yy(10)+ccc
vsbw,all,delete
wpave,xx(7),0,0
vsel,s,loc,y,yy(4)+(1/sqrt(2))*r_fillet-ccc,yy(10)+ccc
vsbw,all,delete
wpave,xx(8),0,0
vsel,s,loc,y,yy(4)+(1/sqrt(2))*r_fillet-ccc,yy(10)+ccc
vsbw,all,delete
wpave,xx(8)+(1/sqrt(2))*r_fillet,0,0
vsel,s,loc,y,yy(4)+(1/sqrt(2))*r_fillet-ccc,yy(10)+ccc
vsbw,all,delete
!*****Application of Plate Material Properties
asel,all

```

```

vsel,all
vsel,s,loc,y,0-ccc,yy(2)+ccc
vsel,a,loc,y,yy(4)+(1/sqrt(2))*r_fillet-ccc,yy(6)+ccc
vsel,a,loc,y,yy(9)-ccc,yy(10)+ccc
vatt,1
!*****Application of Fin Material Properties
asel,all
vsel,all
vsel,s,loc,y,yy(2)-ccc,yy(4)+(1/sqrt(2))*r_fillet+ccc
vsel,a,loc,y,yy(6)-ccc,yy(9)+ccc
vatt,2
!*****Volume Gluing
vsel,all
vglue,all
!*****Application of X-Y Plane Element Size
lsel,all
lsel,s,,43
!Section Shortened for Brevity
lesize,all,xy_mesh_size
!*****Application of X-Y Plane Number of Divisions
lsel,all
lsel,a,,517
!Section Shortened for Brevity
lesize,all,,n_div,1
!*****Application of X-Y Plane Spacing Ratio
lsel,all
lsel,s,,302
!Section Shortened for Brevity
lesize,all,,n_div,spacing_ratio
lsel,all
lsel,s,,44
!Section Shortened for Brevity
lesize,all,,n_div,1/spacing_ratio
!*****Application of Z Plane Element Size
lsel,all
lsel,s,,21
!Section Shortened for Brevity
lesize,all,z_mesh_size
!*****Volume Meshing
vsel,all
vmesh,all
!*****Application of Water Side Pressure and Convection
Loads
*dim,hws,table,17,,z
hws(1,0)=0,.000002,.000005,.000013,.000034,.000090,.000241,.000659,.0018888,.0
02698,.003907,.005769,.008741,.013760,.023030,.042670,.050000

```

```

hws(1,1)=559624,340176,176232,88843,44680,22358,11179,5592,2796,2237,1790,1
432,1146,916.8,733.4,586.7,558.3
asel,all
*do,i,1,n_fin_ws/2,1
asel,s,loc,x,i*(t_fin_ws)+(i-1)*S_ws-ccc,i*(t_fin_ws+S_ws)+ccc
asel,r,loc,y,t_plate*2+height_fin_gs-ccc,t_plate*2+2*height_fin_gs+ccc
sfa,all,1,pres,pres_ws
sfa,all,1,conv,%hws%,15
*enddo
!*****Application of Gas Side Pressure and Convection Loads
*dim,hgs,table,13,,z
hgs(1,0)=0,.04392,.04826,.04924,.04961,.04978,.04987,.04992,.04995,.04997,.04998
,.04999,.05
hgs(1,1)=131.45,169.85,226.45,301.65,402,530.05,692.60,923.3,1102,1423.5,1713.5,
2236,3021.5
*dim,Tgs,table,13,,z
Tgs(1,0)=0,.04392,.04826,.04924,.04961,.04978,.04987,.04992,.04995,.04997,.04998
,.04999,.05
Tgs(1,1)=140.1,148.6,149.5,149.8,149.9,149.9,150,150,150,150,150,150,150
asel,all
*do,i,1,n_fin_gs/2,1
asel,s,loc,x,i*(t_fin_gs)+(i-1)*S_gs-ccc,i*(t_fin_gs+S_gs)+ccc
asel,r,loc,y,t_plate-ccc,t_plate+height_fin_gs+ccc
sfa,all,1,pres,pres_gs
sfa,all,1,conv,%hgs%,%Tgs%
*enddo
!*****Application of Additional Boundary Conditions
asel,s,loc,z,0-ccc,0+ccc
asel,a,loc,z,D-ccc,D+ccc
da,all,uz,0
!*****Application of Symmetry Constraint on Midplane
asel,s,loc,x,W/2-ccc,W/2+ccc
da,all,symm
!*****Transfer of Loads to Elements
allsel,all
sbctran
!*****Solving
FINISH
/SOLU
/STATUS,SOLU
SOLVE

```


References

- [1] Githens, R. E., Minor, W. R., and Tomsic, V. J., 1965, "Flexible-tube Heat Exchangers," *Chemical Engineering Progress*, 61(7), pp. 55-62.
- [2] Hart, G. K., Lee, C-O., and Latour, S. R., 1979, "Development of Plastic Heat Exchangers for Ocean Thermal Energy Conversion," DSS Engineers, Inc., Fort Lauderdale, FL, USA. Technical Report ORO-5165-1.
- [3] Miller, D., Holtz, R. E., Koopman, N., Marciniak, T. J., and MacFarlane, D. R., 1979, "Plastic Heat Exchangers: A State-of-the-Art Review," ANL-79-12.
- [4] Hesselgreaves, J. E., 2001, *Compact Heat Exchangers: Selection, Design, and Operation*, Pergamon, New York, NY.
- [5] Dupont, 2009, "Flue Gas Coolers with AlWaFlon Pressure Hoses Based on DuPont Teflon PTFE Maximize Power Plant Efficiency," Available from: <http://uk.news.dupont.com>.
- [6] Pugh, S. J., Hewitt, G. F., and Müller-Steinhagen, H., 2005, "Fouling During the Use of Seawater as Coolant - the Development of a User Guide," *Heat Transfer Engineering*, 26(1), pp. 35-43.
- [7] Zaheed, L., and Jachuck, R. J. J., 2004, "Review of Polymer Compact Heat Exchangers, with Special Emphasis on a Polymer Film Unit," *Applied Thermal Engineering*, 24(16), pp. 2323-2358.
- [8] T'Joen, C., Park, Y., Wang, Q., Sommers, A., Han, X., and Jacobi, A., 2009, "A Review on Polymer Heat Exchangers for HVAC&R Applications," *International Journal of Refrigeration*, 32(5), pp. 763-779
- [9] Zweben, C., 2004, "Emerging High-Volume Applications for Advanced Thermally Conductive Materials," Proceedings of the 49th International SAMPE Symposium and Exhibition, Long Beach, CA, USA, May 16-20, pp. 4061-4072.
- [10] Shah, R. K., 2006, "Advances in Science and Technology of Compact Heat Exchangers," *Heat Transfer Engineering*, 27(5), pp. 3-22.
- [11] MatWeb, 2011, "Aluminum 3003-H12," Available from: <http://matweb.com>.
- [12] MatWeb, 2011, "Copper, Cu; Annealed," Available from: <http://matweb.com>.
- [13] MatWeb, 2011, "304 Stainless Steel," Available from: <http://matweb.com>.
- [14] MatWeb, 2011, "Pacific Sintered Materials SS-316-RH 316L Stainless Steel Powdered Metal," Available from: <http://matweb.com>.
- [15] MatWeb, 2011, "Titanium, Ti," Available from: <http://matweb.com>.
- [16] Jones, R. F., 1998, *Guide to Short Fiber Reinforced Plastics*, Hanser/Gardner, Cincinnati, OH.
- [17] Ashby, M., Shercliff, H., and Cebon, D., 2007, *Materials Engineering, Science, Processing and Design*, Elsevier, London, UK, Chap. 20.
- [18] Engineering Sciences Data Unit, 2003, "Fouling in Cooling Systems Using Seawater," ESDU 03004.
- [19] Epstein, N., 1981, "Fouling: Technical Aspects," in *Fouling of Heat Transfer Equipment*, Somerscales, E. F. C., and Knudsen, J. G., eds. Hemisphere, Seattle, WA.

- [20] Fassbender, L. L., 1982, Proceedings of the PNL Fouling and Corrosion Workshop, PNL-4871, Battelle Pacific Northwest Laboratories, Richland, WA.
- [21] Garrett-Price, B. A., Watts, R. L., Smith, S. A., and Knudsen, J. G., 1983 “Industrial Fouling: Problem Characterization, Economic Assessment and Review of Prevention, Mitigation and Accommodation Techniques,” PNL-4883, Battelle Pacific Northwest Laboratories, Richland, WA.
- [22] Knudsen, J. G., 1992, “Fouling Control Measures,” in Handbook of Heat Exchanger Design, Hewitt, G. F., ed. , Begell House, New York, NY.
- [23] Brankevich, G. J., de Mele, M. L. F., and Videla, H. A., 1990, “Biofouling and Corrosion in Coastal Power Plant Cooling Water Systems,” *Marine Technology Society*, 24(3), pp. 18-28.
- [24] Flemming, H. C., 2002, “Biofouling in Water Systems – Cases, Causes and Countermeasures,” *Applied Microbiology and Biotechnology*, 59, pp. 629-640.
- [25] Shah, R. K., and Sekulic, D. P., 2003, Fundamentals of Heat Exchanger Design, Wiley, Hoboken, NJ.
- [26] Melo, L. F., and Bott, T. R., 1997, “Biofouling in Water Systems,” *Experimental Thermal and Fluid Science*, 14, pp. 375-381.
- [27] Mott, I. E. C., 1991, Biofouling and Studies Using Simulated Cooling Water, Ph.D thesis, University of Birmingham, Birmingham, UK.
- [28] Baier, R. E., and Meyer, A. E., 1992, “Surface Analysis of Fouling-Resistant Marine Coatings,” *Biofouling*, 6, pp. 165-180.
- [29] Paul, S., 1996, Surface Coatings – Science & Technology, Wiley, Chichester, UK.
- [30] Pfluger, R., 1989, “Physical Constants of Various Polyamides,” in Polymer Handbook, Bandrup, J., and Immergut, E. H., eds., Wiley, New York, NY.
- [31] Drzal, L. T., Mescher, J. A., and Hall, D. L., 1979, “The Surface Composition and Energetics of Type HM Graphite Fibers,” *Carbon*, 17, pp. 375-382.
- [32] Zhao, Q., Wang, C., Liu, Y., and Wang, S., 2007, “Bacterial Adhesion on the Metal-Polymer Composite Coatings,” *International Journal of Adhesion & Adhesives*, 27, pp. 85-91.
- [33] Zhao, Q., Liu, Y., Wang, C., Wang, S., and Muller-Steinhagen, H., 2005, “Effect of Surface Free Energy on the Adhesion of Biofouling and Crystalline Fouling,” *Chemical Engineering Science*, 60, pp. 4858-4865.
- [34] Luckow, P. W., 2009, “Minimum Energy Design of Seawater Heat Exchangers,” MS thesis, University of Maryland, College Park, MD.
- [35] Energy Information Administration, 2010, “Annual Energy Review 2009,” Available at: <http://www.eia.doe.gov>.
- [36] Energy Information Administration, 2011, “Electric Power Annual 2009,” Available at: <http://eia.doe.gov>.
- [37] Energy Information Administration, 2011, “Annual Energy Outlook 2011 with Projections to 2035,” Available at: <http://www.eia.doe.gov>.
- [38] Fthenakis, V., and Kim H. C., 2010, “Life-cycle Uses of Water in U.S. Electricity Generation,” *Renewable and Sustainable Energy Reviews*, 14, pp. 2039-2048.

- [39] Census Bureau, 2009, "Cumulative Estimates of Resident Population Change for the United States, Regions, States, and Puerto Rico and Region and State Rankings: April 1, 2000 to July 1, 2009," Available at: <http://www.census.gov>.
- [40] Kenny, J. F., Barber, N. L., Hutson, S. S., Linsey, K. S., Lovelace, J. K., and Maupin, M. A., 2009, "Estimated Use of Water in the United States in 2005," United States Geological Survey, Available at: <http://pubs.usgs.gov>.
- [41] Wahl, M., 1989, "Marine Epibiosis. I. Fouling and Antifouling: Some Basic Aspects," *Marine Ecology Progress Series*, 58, pp. 175-189.
- [42] Department of Energy, 2008, "Estimating Freshwater Needs to Meet Future Thermoelectric Generation Requirements," Available at: <http://www.netl.doe.gov>.
- [43] Department of Energy, 2009, "Water Requirements for Existing and Emerging Thermoelectric Plant Technologies," Available at: <http://www.netl.doe.gov>.
- [44] Carney, B., Feeley, T., and McNemar, A., "Department of Energy, National Energy Technology Laboratory, Power Plant-Water R&D Program," Available at: <http://www.netl.doe.gov>.
- [45] Tawney, R., Khan, Z., and Zachary, J., 2005, "Economic and Performance Evaluation of Heat Sink Options in Combined Cycle Applications," *Engineering for Gas Turbines and Power*, 127, pp. 397-403.
- [46] Najjar, K. F., Shaw, J. J., Adams, E. E., Jirka, G., and Harleman, R. F., 1979, An Environmental and Economic Comparison of Cooling System Designs for Steam-Electric Power Plants, Massachusetts Institute of Technology, MIT-EL 79-037.
- [47] Schweitzer, P. A., 2000, Mechanical and Corrosion-Resistant Properties of Plastics and Elastomers, Marcel Dekker, New York, NY.
- [48] MatWeb, 2011, "Overview of materials for High Density Polyethylene (HDPE), Injection Molded," Available at: <http://www.matweb.com>.
- [49] Danes, F., Garnier, B., and Dupuis, T., 2003, "Predicting, Measuring, and Tailoring the Transverse Thermal Conductivity of Composites from Polymer Matrix and Metal Filler," *International Journal of Thermophysics*, 24(3), pp. 771-784.
- [50] Lipton, R., and Vernescu, B., 1996, "Composites with Imperfect Interface," *Proceedings of the Royal Society of London Series A*, 452, pp. 329-358.
- [51] Gurdal, Z., Haftaka, R. T., and Hajela, P., 1999, Design and Optimization of Laminated Composite Materials, Wiley, New York, NY.
- [52] Piggott, M., 2002, Load Bearing Fibre Composites, Kluwer Academic, Boston, MA.
- [53] Fu, S. Y., Lauke, B., Mader, E., Yue, C. Y., and Hu, X., 2000, "Tensile Properties of Short-Glass-Fiber- and Short-Carbon-Fiber-Reinforced Polypropylene Composites," *Composites Part A: Applied Science and Manufacturing*, 31, pp. 1117-1125.
- [54] Sato, N., Kurauchi, T., Sato, S., and Kamigaito, O., 1991, "Microfailure Behavior of Randomly Dispersed Short Fibre Reinforced Thermoplastic Composites Obtained by Direct SEM Observation," *Material Science*, 26, pp. 3891-3898.

- [55] Takahashi, K., and Choi, N. S., 1991, "Influence of Fibre Weight Fraction on the Failure Mechanisms of Poly(Ethylene Terephthalate) Reinforced by Short-Glass Fibers," *Material Science*, 26, pp. 4648-4656.
- [56] Cowley, K. D., and Beaumont, P. W. R., 1997, "The Measurement and Prediction of Residual Stresses in Carbon-Fibre/Polymer Composites," *Composite Science and Technology*, 57, pp. 1445-1455.
- [57] Wisnom, M. R., Giglotti, M., Ersoy, N., Campbell, M., and Potter, K. D., 2006, "Mechanisms Generating Residual Stresses and Distortion During Manufacture of Polymer-Matrix Composite Structures," *Composites Part A: Applied Science and Manufacturing*, 37, pp. 522-529.
- [58] Nedele, M., and Wisnom, M. R., 1992, "Micromechanical Modeling of A Unidirectional Carbon Fibre Reinforced Epoxy Composite Subjected to Mechanical and Thermal Loading," Proc. of the American Society for Compos. Seventh Technical Conf., Pennsylvania State University, pp. 328-38.
- [59] Mikata, Y., and Taya, M., 1985, "Stress Field in Coated Continuous Fibre Composite Subjected to Thermomechanical Loadings," *Composite Materials*, 19, pp. 554-579.
- [60] Fiedler, B., Hojo, M., Ochiai, S., Schulte, K., and Ochi, M., 2001, "Finite-element Modeling of Initial Matrix Failure in CRFP under Static Transverse Tensile Load," *Composite Science and Technology*, 61, pp. 95-105.
- [61] Ramsteiner, F., and Theysohn, R., 1985, "The Influence of Fibre Diameter on the Tensile Behavior of Short-Glass-Fibre Reinforced Polymers," *Composite Science and Technology*, 24, pp. 231-240.
- [62] Fu, S. Y., Lauke, B., Mader, E., Yue, C. Y., and Hu, X., 2000, "Tensile Properties of Short-Glass-Fiber- and Short-Carbon-Fiber-Reinforced Polypropylene Composites," *Composites Part A: Applied Science and Manufacturing*, 31, pp. 1117-1125.
- [63] Vincent, M., Giroud, T., Clarke, A., and Eberhardt, C., 2005, "Description and Modeling of Fiber Orientation in Injection Molded Fiber Reinforced Thermoplastics," *Polymer*, 46, pp. 6719-6725.
- [64] EMS Grivory, 2002, "Technical Data Sheet Grilamid L 16 Natural," Available from: <http://www.emsgrivory.com>.
- [65] PolyOne, 2008, "Therma-Tech NJ-6000 TC," Available at: <http://catalog.ides.com>.
- [66] CYTEC Industries, 2008, "ThermalGraph DKD," Available from: <http://www.cytec.com>.
- [67] Nelson, W., 1976, *Nylon Plastics Technology*, Newnes-Butterworths, Boston, MA.
- [68] Ishak, Z. A. M., and Berry, J. P., 1994, "Hygrothermal Aging Studies of Short Carbon Fiber Reinforced Nylon 6.6," *Applied Polymer Science*, 51, pp. 2145-2155.
- [69] Cox, H.L., 1951, "The Elasticity and Strength of Paper and Other Fibrous Materials," *British Journal of Applied Physics*, 3(3), pp. 72-79.
- [70] Tucker, C. L., and Liang, E., 1999, "Stiffness Predictions for Unidirectional Short-fiber Composites: Review and Evaluation," *Composite Science and Technology*, 59, pp. 655-671.

- [71] Eduljee, R. F., McCullough, R. L., and Gillespie, J. W., 1994, "The Influence of Inclusion Geometry on the Elastic Properties of Discontinuous Fiber Composites," *Polymer Engineering Science*, 34, pp. 352-360.
- [72] Pegoretti, A., Fambri, L., Zappini, G., and Bianchetti, M., 2002, "Finite Element Analysis of a Glass Fibre Reinforced Composite Endodontic Post," *Biomaterials*, 23, pp. 2667-2682.
- [73] Halpin, J. C., and Kardos, J. L., 1976, "The Halpin-Tsai Equations: A Review," *Polymer Engineering and Science*, 16(5), pp. 344-352.
- [74] Hahn, H. T., and Tsai, S. W., 1980, *Introduction to Composite Materials*, Technomic, Lancaster, PA.
- [75] Agarwal, B. G., and Broutmann, L. J., 1990, *Analysis and Performance of Fiber Composites*, Wiley, New York, NY.
- [76] Fu, S., and Lauke, B., 1997, "The Elastic Modulus of Misaligned Short-Fiber-Reinforced Polymers," *Composite Science and Technology*, 58, pp. 389-400.
- [77] Foye, R. L., 1972, "The Transverse Poisson's Ratio of Composites," *Composite Materials*, 6(2), pp. 293-295.
- [78] Schapery, R. A., 1968, "Thermal Expansion Coefficients of Composite Materials Based on Energy Principles," *Composite Materials*, 2(3), pp. 380-404.
- [79] Karadeniz, Z. H., and Kumulutas, D., 2007, "A Numerical Study on the Coefficients of Thermal Expansion of Fiber Reinforced Composite Materials," *Composite Structures*, 78, pp. 1-10.
- [80] Nielson, L. E., 1974, "The Thermal and Electrical Conductivity of Two-Phase Systems," *Industrial & Engineering Chemistry Fundamentals*, 13(1), pp. 17-20.
- [81] Progelhof, R. C., Reutsch, R. R., and Throne, J. L., 1976, "Methods for Predicting the Thermal Conductivity of Composite Systems – A Review," *Polymer Engineering and Science*, 16, pp. 615-625.
- [82] Ishai, O., 1975, "Environmental Effects on Deformation, Strength, and Degradation of Unidirectional Glass-fiber Reinforced Plastics. I. Survey," *Polymer Engineering and Science*, 15, pp.486-490.
- [83] Kampf, J., and Sadrinasab, M., 2006, "The Circulation of the Persian Gulf: a Numerical Study," *Ocean Science*, 2, pp. 27-41.
- [84] ASTM Standard D638, 2010, "Standard Test Method for Tensile Properties of Plastics," American Society for Testing and Materials International, West Conshohocken, PA.
- [85] Starkweather, H. W., Moore, G. E., Hansen, J. E., Roder, T. M., and Brooks, R. E., 1956, "Effect of Crystallinity on the Properties of Nylons," *Polymer Science*, 21, pp. 189-204.
- [86] Loos, A, and Springer, G., 1979, "Moisture Absorption of Graphite-Epoxy Composites Immersed in Liquids and in Humid Air," *Composite Materials*, 13, pp. 131-147.
- [87] Pinho, P, and Macedo, E., 2005, "Solubility of NaCl, NaBr, and KCl in Water, Methanol, Ethanol, and Their Mixed Solvents," *Chemical Engineering Data*, 50, pp. 29-32.

- [88] Walpole, R. E., Myers, R. H., Myers, S. L., and Ye, K., 2007, *Probability & Statistics for Engineers & Scientists*, Pearson Prentice Hall, Upper Saddle River, NJ, Chap. 13.
- [89] Ishai, O., 1975, "Environmental Effects on Deformation, Strength, and Degradation of Unidirectional Glass-Fiber Reinforced Plastics. II. Experimental Study," *Polymer Engineering and Science*, 15, pp. 491-499.
- [90] ADGAS Personnel & Training Division, "Basic Operator Course: Overview of Processes," Module 17, Part 1, Trains I, II, III and Storex. Rev. 0.0.
- [91] Haytouni, N., and Rodgers, P., 2008, "Survey of Heat Exchanger Usage at ADGAS Das Island LNG Plant."
- [92] Lepi, S. M., 1998, *Practical Guide to Finite Elements*, CRC Press, New York, NY, Chap. 7.
- [93] ANSYS, 2009, "Element Guide," Release 12.0, Available from: www.ansys.com.
- [94] White, F. M., 1991, *Viscous Fluid Flow*, McGraw-Hill, New York, NY.
- [95] Wilbuswas, P., 1966, *Laminar Flow Heat Transfer in Non-Circular Ducts*, Ph.D thesis, London University, London.
- [96] Shah, R. K., and London, A. L., 1978, *Laminar Flow Forced Convection in Ducts*, Academic Press, New York, NY.
- [97] Kakac, S., Shah, R. K., and Aung, W., eds., 1987, *Handbook of Single-Phase Convection Heat Transfer*, Wiley, New York, NY.
- [98] Culham, J. R., and Yovanovich, M. M., 1998, "Factors Affecting the Calculation of Effective Conductivity in Printed Circuit Boards," *Proc. Sixth Intersociety Conf. on Thermal and Thermomechanical Phenomena in Electronic Systems*, pp. 460-470.
- [99] Hewitt, G. F., Shires, G. L., and Bott, T. R., 1994, *Process Heat Transfer*, CRC Press, Ann Arbor, MI, Chap. 3.
- [100] Dally, J. W., Bonenberger, R. J., 2004, *Design Analysis of Structural Elements*, College House Enterprises, Knoxville, TN.